Prenylation in cell-intrinsic innate immunity to positive-strand RNA viruses

Frank William Soveg

A dissertation

submitted in partial fulfillment of the

requirements for the degree of

Doctor of Philosophy

University of Washington

2021

Reading Committee:

Ram Savan, Chair

Daniel B. Stetson

Michael Gale, Jr.

Program Authorized to Offer Degree:

Immunology

University of Washington

Abstract

Prenylation in cell-intrinsic innate immunity to positive-strand RNA viruses

Frank William Soveg

Chair of the Supervisory Committee:
Ram Savan, Ph.D
Department of Immunology

Cell intrinsic antiviral immunity is a critical facet of the innate immune response to viruses. Since virtually every subcellular compartment can be utilized by viruses for replication, antiviral factors must also be positioned in these compartments to effectively interact with various viral threats. In this thesis, we explored the impact organelle membrane targeting through protein prenylation has on the antiviral specificity of innate immune RNA binding proteins in the context of positive-strand RNA virus infection. Since positive-strand RNA viruses use host organelle membranes to construct niches for RNA replication, we hypothesized antiviral RNA binding proteins that localize to organelle membranes might have enhanced access to viral RNA generated by these viruses during infection. We focused on two antiviral RNA binding proteins: zinc finger antiviral protein (ZAP) and oligoadenylate synthetase 1 (OAS1). The long isoform of ZAP, ZAP-L, is prenylated and targeted to endosomes and lysosomes. This localization is critical for its antiviral activity against alphaviruses, which use those compartments for RNA replication. The cytosolic short isoform of ZAP, ZAP-S, regulates interferon RNA. Similarly, the p46 isoform of OAS1 is prenylated and localizes primarily to the Golgi apparatus and the endoplasmic reticulum. Localization to these compartments bestows p46 with enhanced antiviral activity against viruses that use ER and Golgi membranes for RNA replication, including picornaviruses, flaviviruses, and coronaviruses. Overall, prenylation can target innate immune antiviral RNA binding proteins to subcellular compartments where positive-strand RNA viruses sequester their RNA.

TABLE OF CONTENTS

LIST OF FIGURES

LIST OF TABLES

ACKNOWLEDGEMENTS

No journey is completed without the help of others, and I am extremely fortunate to have such wonderful and supportive mentors, friends, and family.

First and foremost, I'm extremely grateful for my mentor, Dr. Ram Savan, who has provided consistent support and guidance throughout my time in his lab. His continual enthusiasm for my work has kept me going through times both good and bad. Thank you for being patient with me and for always trying to push me to be a better scientist and person. Thank you for cultivating a lab environment that is not only scientifically rigorous, but also filled with some of the best people I have ever had the pleasure to work with. I'm deeply indebted to Dr. Johannes Schwerk, who I have had the pleasure to work side by side with, figuratively and literally as our benches are next to each other, throughout my time in the lab. Thank you for being such a great mentor and friend. Without you this work would not have been possible. Thank you, Dr. Adriana Forero, for invaluable project advice and always being willing to have engaging scientific discussions. Thank you to Dr. Lomon So, Snehal Ozarkar, Julian Smith, Dr. Matt Hendricks, Dr. Nandan Gokhale, and Rachel Van Gelder for being wonderful labmates and colleagues. Thanks to all who did make the Ram lab a wonderful place to work.

This work would also not have been possible without contributions from members of the Gale laboratory, including Drs. Alison Kell, Justin Roby, Katarina Esser-Nobis and Michael Davis. Thank you so much for your support.

A very special thank you to Sandy Turner. Without your support and gentle reminders, I would definitely not have registered for classes or paid my student fees on time. Thank you for all that you do to ensure us graduate students stay on track.

Finally, my thesis committee, through their feedback and helpful discissions, has been instrumental in getting this work completed. So thank you, Drs. Ram Savan, Dan Stetson, Harmit Malik, Josh Woodward and Michael Gale, Jr.

DEDICATION

I dedicate this work to the memory of my Yiayia, Sophie Soveg,

whose selflessness, optimism, and zest for life

inspires me to this day.

Chapter 1. Introduction

Non-self-recognition forms the basis of immunity and is the foundation of the field of immunology. This process is an initial and critical event in the innate immune response where germline encoded pathogen recognition receptors (PRRs) intercept microbial products termed pathogen associated molecular patterns (PAMPS). Sensing of PAMPs by PRRs leads to the activation of cell intrinsic and cell extrinsic immune responses which serve to limit replication of the pathogen and instruct the adaptive immune response.

One of the defining features of the eukaryotic cell is the presence of membrane-bound organelles. These subcellular structures serve to organize and compartmentalize cellular processes, and even keep immunostimulatory self-molecules, such as RNA and DNA, segregated from innate immune PRRs. However, a major group of RNA viruses, the positive-strand RNA viruses, have evolved to dramatically usurp and reorganize organelle membranes for their replication. These viral-derived replication organelles (ROs) are the platforms for viral RNA synthesis and shield immunostimulatory viral RNA from RNA-detecting PRRs and antiviral effectors. Despite the importance of these viruses to global health, how the innate immune system counters the RO is understudied.

In this thesis, we explored the consequence of membrane-targeting through prenylation in innate immune defense against positive-strand RNA viruses. Collectively, we found targeting innate immune RNA binding proteins to organelles included in the ROs of positive-strand RNA viruses enhanced their ability to detect viral RNA. Thus, organelle targeting of innate immune PRRs and effectors through lipidation and other means may represent an effective host strategy to access the replication organelle.

1.1 Positive-strand RNA viruses

Virus life cycle overview

Positive-strand RNA viruses include many viruses that cause human disease, such as Poliovirus, West Nile virus (WNV), Hepatitis C virus (HCV), and severe acute respiratory syndrome coronavirus 2 (SARS-CoV-2). Positive-strand RNA viruses are so termed because their single stranded RNA genomes are read by the host translational machinery as mRNA. Infection begins when a virion binds to its cognate receptor on a susceptible cell in a process known as attachment. Internalization of the virion then occurs by receptor mediated endocytosis. Acidification of the endosomal compartment leads to conformational shifts in the viral glycoproteins, allowing the viral envelope to fuse to the vesicle membrane and viral RNA to escape to the cytosol in a process known as fusion. Since the RNA genomes of positive-strand RNA viruses are read as messenger RNA, the viral genome is translated into a single polypeptide by the host translational machinery. This polypeptide is then cleaved to generate nonstructural proteins that facilitate replication. Following cleavage, the viral nonstructural proteins form a replicase complex that synthesizes negative strand RNA from the positive-strand template. This negative strand RNA serves as a template to generate new positive-strand RNA, which goes on to be translated into more viral proteins or packaged into new virions in a process known as assembly. Newly assembled virions are then released from the cell in a process known as egress. These virions then go on to infect new cells.

The replication organelle formed by positive-strand RNA viruses.

One defining feature of positive-strand RNA viruses is the ability to form replication organelles (ROs) derived from host organelle membranes (Fig 1.1). ROs are the sites of viral RNA synthesis. Additionally, ROs function to organize products needed for genome

amplification while also shielding viral RNA synthesis from innate immune sensors. ROs can be divided into two types depending on if the ROs are formed by negative or positive membrane curvature (Fig 1.2). The first are single membraned vesicles or spherules that form by negative membrane curvature of the donor membrane into the organelle lumen. The other type of replication organelle is the double-membraned vesicle (DMV) which is formed by outward curvature of the donor organelle membrane. Interestingly, different positive-strand RNA viruses use unique combinations of organelle membranes to form replication organelles. Host proteins are also recruited to the replication complexes of positive-strand RNA viruses where they facilitate replication, and this may allow host antiviral proteins to be recruited to the RO provided they are positioned at the correct organelle. A consideration of the membranes recruited to these sites of viral RNA synthesis will help us rationalize the innate immune effectors that may be able to gain access to these compartments.

Alphaviruses: Alphaviruses are members of the family Togaviridae, which also includes Rubiviruses. A number of alphaviruses are human pathogens, including Chikungunya virus (CHIKV), O'nyong'nyong virus (ONNV), and Sindbis virus (SINV). Semliki forest virus (SFV) is not a human pathogen but is a useful model virus for studying alphavirus life cycle. Studies with SINV and SFV have shown the ROs of alphaviruses are formed by invaginations at the plasma membrane and at modified endosomes and lysosomes known as type 1 cytopathic vacuoles (CPV1s) (*1-4*). These invaginations, termed spherules, contain dsRNA and are roughly 50nm in diameter and contain a neck-like pore of roughly 10nm connecting the spherule lumen to the cytosol (*1*) (Fig 1.2 A). This neck is comprised of the non-structural proteins nsP1, nsP2, nsP3, and nsP4 that form the replicase complex (*5, 6*). Work on SINV and SFV has

demonstrated viral RNA synthesis occurs primarily at these plasma membrane spherules, and that plasma membrane spherules are endocytosed to form CPV1s (*7*, *8*). Whether or not plasma membrane spherules are the primary site of RNA synthesis for other alphaviruses such as CHIKV and ONNV remains to be ascertained. Work aimed at addressing the membrane composition of plasma membrane spherules formed by SFV have identified plasma membrane, endosomal, and endoplasmic reticulum markers in these replication complexes (*8*).

Coronaviruses: Coronaviruses include important human pathogens such as the severe acute respiratory syndrome coronaviruses SARS-CoV and SARS-CoV-2 and Middle Eastern respiratory syndrome coronavirus (MERS-CoV). The murine hepatitis virus (MHV) is a mouse coronavirus often used as a model coronavirus for *in vitro* and *in vivo* studies. During coronavirus infection, the cytosol is populated with membrane tubules, double-membraned vesicles (DMVs), and vesicle packets primarily derived from ER membranes (*9*-*12*) (Fig 1.2 B). Cotransfection of SARS-CoV nsp3, nsp4, and nsp6 are sufficient to induce DMVs, suggesting a prominent role of these viral proteins in DMV formation (*13*). The outer membranes of these double-membraned vesicles are connected to the ER network via these membrane tubules (*12*). Although the double-membraned vesicles were found to contain dsRNA, it was unclear if they are the sites of vRNA synthesis as the DMVs lacked any clear connection to the cytosol (*10*). A recent study used metabolic labeling of RNA followed by electron microscopy to demonstrate vRNA synthesis does indeed occur within the DMV (*11*). To support this observation, a molecular pore complex was described spanning the DMVs of MHV and SARS-CoV-2 (*14*). At least for MHV, this pore consisted of the non-structural protein nsp3, providing a mechanism for how substances might be exchanged across the DMV (*14*). Work on SARS-CoV-2 has

documented disassembly of the Golgi and repositioning of Golgi membranes in proximity to DMVs where they may serve as a site of virion assembly (*12*).

Picornaviruses: The ROs of the human pathogens poliovirus (PV) and Coxsackievirus B3 (CVB3) are perhaps the most well-studied. Both viruses form a network of single-membraned tubules and double-membraned vesicles during infection generated by outward curvature of the donor organelle membrane that is not contiguous with any particular organelle or organelle network (*15, 16*) (Fig 1.2). The single-membraned tubules are produced first during infection and later give rise to the double-membraned vesicles (*16*). The viral replicase is located on the cytosolic face of the single-membraned tubule network where the majority of viral RNA is synthesized, although viral RNA synthesis does occur on the double-membraned vesicles to some degree (*17, 18*). The exact function of the double-membraned vesicles is unclear, although they seem to play a role in nonlytic release of PV particles (*19*). The specific organelle membranes used initially by picornaviruses for RO formation have been debated since picornavirus ROs are not contiguous with any particular organelle, with studies showing either endoplasmic reticulum and/or Golgi membranes serving as sites of viral RNA replication (*20-23*). Indeed, recent work using live-cell imaging has found both ER and Golgi membranes can serve as the donor membranes for CVB3 ROs, suggesting some flexibility with respect to the initial organelle membrane source that can be used (*24*). The ROs of CVB3 have also been found to be in contact with lipid droplets, which act as a source of lipids required for replication (*25*).

Flaviviruses: Flaviviruses of the genus *Flaviviridae* include important human pathogens such as West Nile virus (WNV), Zika virus (ZIKV), Dengue virus (DENV), and Tick-born encephalitis

virus (TBEV). Electron microscopy studies have revealed these viruses generate vesicle packets (VPs) by negative curvature of the rough endoplasmic reticulum inwards to the ER lumen (*26-29*) (Fig 1.2 A). These VPs are connected to the cytosol via a narrow pore, roughly 10nm in diameter, that allows for the exchange of solutes including viral RNA (*27, 29*). Studies with WNV have shown these vesicle packets contain double-stranded RNA and the RNA-dependent RNA polymerase NS5 and therefore are the presumed sites of viral RNA replication (*27, 30*). At least for DENV, these vesicle packets are generally situated opposite the sites of viral particle assembly at the ER, which allows for spatial coordination of RNA replication and particle assembly (*29*). The non-structural proteins NS2A, NS4A, NS4B, are transmembrane proteins and play an important role in the formation of vesicle packets (*31-34*). Although not a transmembrane protein, NS1 has membrane-shaping properties and is also implicated in replication organelle formation (*35*). Studies on host proteins important for flavivirus RO formation have demonstrated ER-shaping atlastin (ATL) proteins as being critical for inducing negative membrane curvature. Specifically, depletion of ATL2 resulted in a reduction in DENV replication and altered VP morphology (*36*). Thus, host proteins are important for supporting the membrane rearrangements induced during infection.

Hepatitis C virus (HCV) is a Flavivirus and a member of the genus *Hepacivirus* and can cause considerable disease in humans in the form of viral hepatitis. Unlike members of *Flaviviridae*, HCV generates a RO dubbed the membranous web that consists of double-membraned vesicles derived from the ER that are embedded in the ER network (*37, 38*) (Fig 1.2 B). These are morphologically similar, although not identical, to the DMVs produced by coronaviruses. Virtually all of HCV's non-structural proteins interact with lipids and membranes with NS4B playing a prominent role in rearranging membranes and forming DMVs (*39*). The

positive-strand RNA and newly synthesized RNA accumulates in these double-membraned vesicles, implicating them as the sites of viral RNA synthesis (*40-42*). Biochemical purification of HCV DMVs confirmed these compartments contain the viral polymerase NS5B and are the sites of viral RNA synthesis (*41*). The HCV replicase complex and viral RNA are contained in a relatively inaccessible compartment as the ability of purified HCV replication organelles to synthesize viral RNA is not inhibited by protease or RNase treatment (*41, 43*). How transport occurs across HCV DMVs is not entirely clear. Pore-like openings were seen in a minority of DMVs, suggesting they may contain a pore complex or contain a transient opening linking them to the cytosol (*37*). Nuclear pore complexes are recruited to the membranous web, but if they localize to DMVs and facilitate transport in and out of the replicase compartment remains to be determined (*44*).

1.2 Innate immunity to positive-strand RNA viruses

RLRs and TLRs involved in viral nucleic acid sensing

The ability of a cell to sense the presence of a virus is critical to mounting an effective immune response. The host encodes an array of sensors capable of distinguishing its own DNA and RNA from those of viruses. Upon binding their nucleic acid ligand, these sensors initiate a signaling cascade that activates a cell intrinsic and extrinsic immune response. The ability of these sensors to activate downstream response pathways make them indispensable for host innate immune defense against virtually all viruses. These host nucleic acid sensors are typically placed in subcellular compartments where viral nucleic acids are anticipated to accumulate. The major non-self-molecule detected by the innate immune system during positive-strand RNA virus infection is the viral RNA. The toll-like receptors (TLRs) localize to the endolysosomal compartment while the RIG-I-like receptors (RLRs) localize to the cytosol.

Toll-like receptors

TLRs are important for the detection of microbial products from a variety of different pathogens(*45*). The RNA-sensing TLRs are TLR3, TLR7, and TLR8. The sensing domains of these proteins face the endolysosomal lumen while the signaling domains point towards the cytosol. Placement within the endolysosomal compartment allows these TLRs to sense internalized sources of viral RNA such as virions and infected cells. TLR3 senses double-stranded RNA and is expressed in many different cell types (*46*). Studies in TLR3 deficient mice and cells have demonstrated an important role for TLR3 in responses to EMCV, CVB3, HCV, and DENV (*47-50*). In contrast, TLR7 and TLR8 sense single stranded viral RNA. (*51, 52*) One major difference between TLR7 and TLR8 is they exhibit cell-type specific expression. TLR7 is largely expressed on plasmacytoid dendritic cells while TLR8 expression is largely restricted to monocytes (*52, 53*). TLR7 and TLR8 have been shown to be important in immune responses to WNV, MHV, HCV, and CVB (*54-57*). Ultimately, TLR engagement leads to the induction of antiviral and proinflammatory mediators.

RIG-I-like receptors

Accumulation of viral RNA in the cytosol is sensed by the RIG-I-like receptors (RLRs). The RLRs consist of the three intracellular dsRNA-dependent RNA helicases retinoic acid-inducible gene I (RIG-I), melanoma differentiation-associated protein 5 (MDA5), and laboratory of genetics and physiology 2 (LGP2). RIG-I and MDA5 are active signaling molecules while LGP2 can regulate RIG-I and MDA5 signaling (*58-61*). These proteins are localized to the cytosol (*62*). Studies in RIG-I and MDA5 deficient mice or cells have demonstrated both redundant and nonredundant roles for these sensors in various viral infections *in vitro* and *in vivo*. RIG-I is required for resistance to vesicular stomatitis virus (VSV), influenza A virus

(IAV), Newcastle disease virus (NDV), and ZIKV (*59, 63-65*), while MDA5 is critical for resistance to picronaviruses and coronaviruses such as CVB3 and MHV (*66-69*). Both sensors contribute to innate immune defense against some viruses, including WNV and DENV (*64, 70, 71*). Consistent with the RLR's somewhat different roles in viral RNA sensing, RIG-I and MDA5 have different RNA ligand preferences. RIG-I binds to short, blunt, double-stranded, 5' tri-phosphorylated RNA characteristic of some viral genomes and replication intermediates while, in contrast, MDA5 prefers long RNA duplexes such as the replicative intermediates of picornaviruses (*66, 67, 72*). Viral RNA binding to RIG-I or MDA5 induces a signaling cascade that requires the signaling adaptor mitochondria antiviral signaling MAVS protein (*73-76*). Signaling through MAVS ultimately results in activation of the kinases TNK-binding kinase 1 (TBK1) and IκB kinase-ε. This signaling cascade culminates in the activation and nuclear translation of NF-κB, IRF3, and IRF7. Collectively, these transcription factors induce a cell-intrinsic and extrinsic antiviral state through the synthesis of type I and III interferons and antiviral factors.

Several studies have evaluated the impact of ROs on innate immune sensing. Microscopy analysis of Tick-borne encephalitis virus (TBEV) RNA demonstrated the viral RNA is largely confined to the replication compartment, suggesting viral RNA is not accessible to the majority of cytosolic PRRs (*28*). Accordingly, experiments comparing the ability of TBEV strains to elicit innate immune responses found TBEV RNA is not accessible to the cytosol until late in infection and appearance of TBEV RNA in the cytosol correlates with interferon production (*77*). Another study comparing the cytosolic accessibility of DENV and Yellow Fever virus (YFV) found DENV RNA is less accessible to the cytosol and this correlates with decreased interferon

production (*78*). Whether or not differences in cytosolic accessibility of viral RNA is a general theme of positive-strand RNA viruses remains to be explored.

For HCV, recruitment of nuclear pore proteins to the membranous web were shown to exclude cytosolic PRRs from this compartment (*79*). Interestingly, adding a nuclear localization signal to RIG-I enhanced interferon production during infection. This supports a model in which accessing the RO may enhance antiviral responses against positive-strand RNA viruses. Interestingly, the fact that RIG-I can still signal while in the RO of HCV suggests ER rearrangements during infection are not sufficient to block innate immune signaling. Whether or not the ROs of other plus-strand RNA viruses similarly inhibit PRR recruitment has not been investigated.

Interferons and pan-antiviral activity

Sensing of viral RNA leads to the production of interferons, which are critical antiviral cytokines. The three types of interferon are the type I, II, and III interferons. These cytokine molecules are essential for the control of viruses both *in vitro* and *in vivo*. The ability of a cell to produce and respond to interferon varies, which results in a complex network of interferon responses. Interferons exert their effector functions by signaling though cognate interferon receptors which induce an antiviral state in the responding cell through the modulation of interferon regulated genes. Many of these interferon regulated genes are proteins that promote cell intrinsic antiviral immunity by directly interfering with particular viral life cycle steps (*80*).

Type I interferons include 13 IFN-αs, IFN-β, IFN-ε, IFN-κ, and IFN-ω signal through the interferon α/β receptor (IFNAR) is comprised of the IFNAR1 and IFNAR2 heterodimers. Virtually all nucleated cells are capable of producing at least some subset of the type I interferons. Also, all nucleated cells express IFNAR and are capable of responding to type I

interferon. Signaling through IFNAR leads to the activation of a JAK/STAT pathway that results in the assembly and nuclear translocation of the ISGF3 complex, which consists of STAT1, STAT2, and IRF9. The ISGF3 complex activates the transcription of antiviral and other genes leading to an antiviral cellular state (*81*).

The type II interferons consist only of IFN-γ, which is almost exclusively produced by adaptive immune cells such T lymphocytes. The receptor for interferon gamma is less restricted than its ligand and is expressed on most cells. Interferon gamma is an important antiviral cytokine although, because of its adaptive cell source, it is likely more important at later stages of infection or reinfection (*82*). Interestingly, IFN-γ has been shown to interfere with the formation of pathogen-induced membrane structures, including positive-strand RNA virus ROs, through the autophagy pathway (*83, 84*).

Type III interferons are the interferon lambdas, which include four subtypes: IFNL1, IFNL2, IFNL3, and IFNL4. IFNL4 is a pseudogene and not secreted from the cell (*85*). These interferons signal through the interferon lambda receptor (IFNLR) which is a complex of the IL-10R2 and IFN-λR1 proteins. Like type I interferon, virtually all nucleated cells are capable of producing interferon lambda. However, expression of the IFNLR is mostly restricted to epithelial cells. Thus, interferon lambda is important for antiviral immunity at barrier surfaces such as the lung, intestine, and reproductive tract (*86*). Like IFNAR, signaling through IFNLR results in the formation and nuclear translocation of the ISGF3 complex resulting in gene regulation. Although type I and III interferons modulate a largely overlapping set of genes, some differences in the kinetics of induction and genes induced exist. For example, type I interferon induces expression of IRF1 which leads to the induction of certain chemokines not seen with type I interferon treatment (*87*).

Cell intrinsic restriction of positive-strand RNA viruses

Cell intrinsic restriction to viruses described the mechanisms by which cells suppress virus production. Cells have evolved mechanisms to interfere with every step of the virus life cycle (*80*). Many proteins produced downstream of interferon signaling directly interfere with virus replication by targeting viral proteins or viral nucleic acids for degradation. Although hundreds of interferon stimulated genes and IRF target genes have been described, the mechanistic details of these genes are poorly defined or completely unknown (*80, 88*). Here, ISGs that have been described to interact with the replication organelle or replicase of positive-strand RNA viruses are summarized.

An IFN-γ inducible-system directly targeting the replication organelles of murine norovirus (MNV) has been described. MNV uses membranes derived from ER, Golgi, and lysosome to form its replication organelle (*89*). MNV is sensitive to IFN-γ pathway in a manner that depends on non-degradative autophagy (*84*). Interestingly, this pathway is not induced by type I interferon and thus represents an IFN-γ unique pathway targeting ROs. This is because, compared to type I interferon, IFN-γ treatment induces robust production of the immunity-related GTPases (IRGs) and guanylate binding proteins (GBPs). Both IRGs and GBPs are recruited to the RO of MNV and are required for IFN-γ dependent restriction of MNV (*83*). How this pathway specifically restricts the ROs is unclear. Possible mechanisms include preventing the formation of the RO or rupturing the RO. The latter mechanism is plausible as this autophagy/IRG/GBP pathway was shown to rupture the intracellular replication niches of *Toxoplasma gondii*. Indeed, rupturing the RO might expose viral RNA and other PAMPs to

innate immune detection, for example. Future work is needed to define if this pathway is only active against noroviruses and if other mechanisms exist to disrupt the RO.

Viperin (RSAD2) is an ISG with broad antiviral activity against viruses including WNV, DENV, ZIKV, and HCV. Viperin localizes to the ER and lipid droplets through an N-terminal amphipathic α-helix (*90, 91*). Membrane topology experiments have localized viperin to the cytosolic face of organelle surfaces, which would allow this protein to access viral products within replication compartments (*91*). Indeed, viperin localizes to the replication organelles of HCV and the α-helix is critical for its ability to interact with NS5A and inhibit HCV. Interesting, this helix is dispensable for its antiviral activity against DENV. Expression of viperin also causes distortions in ER membranes but whether or not viperin-induced ER distortions can modulate the formation of ER-derived ROs remains to be explored (*91*). Interestingly, α-helices imbedded on the cytosolic face of an organelle surface generate positive membrane curvature, which may oppose the negative curvature enforced by some flaviviruses (*92*).

TRIM5α is an ISG and was shown to inhibit tick born flaviviruses Tick-born encephalitis virus (TBEV), Kyasanur forest disease (KFD), and Langat virus (LGTV). During infection with these viruses, TRIM5α localizes to sites of viral replicase formation (NS5 and NS3 positive) at the RO. Mechanistically, TRIM5α promotes the degradation of the NS2B/3 complex. How TRIM5a localizes to the RO to interact with the ER-imbedded NS2B/3 complex is uncertain as TRIM5α has no obvious ER-targeting domains. Evaluating if TRIM5α is already localized to an organelle membrane prior to infection may be of value. Surprisingly, TRIM5α lacks antiviral activity against the tick-born flavivirus Powassan virus (POW). However, whether or not TRIM5α is recruited to sites of POW replication was not discerned. TRIM5α also lacks antiviral

activity against DENV2, ZIKV, and YFV, and does not seem to be recruited to sites of viral replication (*93*).

Two independent genome wide screens for ISGs targeting flaviviruses identified interferon alpha-inducible protein 6 (IFI6) as an important restriction factor for WNV, DENV, ZIKV, and the yellow fever virus (YFV) (*94, 95*). IFI6 blocks the replication of these viruses at a step before genome replication but after polyprotein processing. Notably, IFI6 contains a signal peptide and is embedded in the ER and localizes to sites of DENV RNA accumulation during infection (*95*). Thus, it was proposed IFI6 inhibits RO formation of select flaviviruses by inhibiting the negative membrane curvature required for their formation (*95*). Consistently, IFI6 had no antiviral activity against HCV which, unlike IFI6-sensitive viruses, generates ER-derived ROs by positive membrane curvature. Further, IFI6 had no antiviral activity against CVB3 which also generates ROs via positive membrane curvature. How IFI6 inhibits membrane curvature is unknown.

Receptor-transporting protein 4 (RTP4) is an ER-localized RNA-binding ISG with antiviral activity against ZIKV, WNV, YFV, and DENV (*96*). Mechanistically, RTP4 localizes to sites of flavivirus RNA replication and seems to inhibit replication by disrupting the interaction between the replicase components NS5 and NS3. Since the RNA-binding zinc finger domain of RTP4 is required for antiviral activity RTP4 may disrupt interactions between the replicating viral RNA and the replicase complex. Although RTP4 contains a transmembrane anchor, this anchor is dispensable for ER localization and antiviral activity suggesting RTP4 gains access to the ER and/or replicase complex via some other means (*96*). Interestingly, human RTP4 is not antiviral against other positive-strand RNA viruses that utilize ER-membranes for replicase formation such as HCV and the human coronavirus OC43 (HCoV-OC43). These

differences in the antiviral activity of RTP4 may be explained by the differences in membrane curvature induced by these viruses (positive vs negative) which could impact viral RNA access or by the differences in the RNA sequences of these viruses (*96*).

1.3 Protein lipidation of innate immune effectors as a way to access the RO

Many of the antiviral proteins capable of accessing the RO are proteins targeted to organelle membranes prior to infection. Thus, organelle membrane targeting of innate immune factors may represent a host strategy to gain access to the RO. In particular, targeting of proteins to the cytosolic face of organelle surfaces would allow these proteins to interface with viral proteins and RNA within the ROs. One mechanism by which proteins are targeted to the cytosolic surface of organelle membranes is through lipidation.

Lipidation is a post-translational protein modification where a lipid is covalently attached to a protein containing a lipidation motif (*97*). In contrast to proteins containing transmembrane domains, which span both leaflets of a lipid bilayer (integral membrane proteins), lipidated proteins are inserted into the cytosolic leaflet of particular organelles. One important function of lipidation is to organize signaling complexes and facilitate protein-protein interactions at organelle surfaces (*97*). Of interest to this thesis is the addition of an isoprenyl fatty acid group to a protein via a process known as prenylation.

Mechanisms and consequences of protein prenylation

Prenylation is the irreversible addition of a 15-carbon farnesyl pyrophosphate (FPP) or a 20-carbon geranylgeranyl pyrophosphate (GGPP) to the C-terminus of proteins containing a "CaaX box" at their C-termini where C is cysteine, a is aliphatic, and X is a variable amino acid. There is one described farnesyltransferase (FTase) and three geranylgeranyl transferases

geranylgeranyl transferase type I (GGTase1), geranylgeranyl transferase type II (GGTase2), and the recently identified geranylgeranyl transferase III (GGtase3) (*98, 99*). Although farnesyl diphosphate and geranylgeranyl diphosphate are similar lipids, the longer and more hydrophobic carbon chain of the geranylgeranyl group has a greater affinity for cellular membranes (*100*) A CaaX-containing protein is geranylgeranylated if the X amino acid is a leucine or phenylalanine, any other amino acid results in farnesylation (*101*). The prenyltransferases are cytosolic proteins and therefore prenylation occurs in the cytosol (Fig. 1.3). Shortly after prenylation, prenylated proteins are recruited to the ER where they undergo post-prenylation processing (*102*). Two ER-localized enzymes facilitate this sequential processing. The first is Ras converting CAAX endopeptidase 1 (RCE1), which cleaves the "aaX" peptide. After, protein-S-isoprenylcysteine O-methytransferase (ICMT) adds a methyl group to the prenylcysteine which increases protein hydrophobicity (Fig. 1.3). Prenylated proteins then traffic to various destinations within the endomembrane system.

By targeting proteins to organelle membranes, prenylation can spatially organize protein complexes, coordinate signaling networks, and facilitate receptor-ligand interactions at organelle surfaces. The role of prenylation in spatially organizing signaling complexes is perhaps best studied for the RAS family of signaling proteins which, in humans, is composed of HRas, KRas, and NRas (*103*). Briefly, the RAS family of small GTPases are involved in the mitogen-activated protein kinase (MAPK) signal transduction pathway important for cell growth and cell differentiation (*103*). All Ras proteins contain a C-terminal CaaX motif and are targeted to the plasma membrane after ER processing by RCE1 and ICMT (*104*). Localization to the plasma membrane is critical for Ras to interact with other components of the MAPK pathway. Ablation of the CaaX motif in any of the Ras proteins abolishes signaling activity, demonstrating the

importance of plasma membrane localization for Ras function (*104*). Several innate immune proteins with antiviral activity against positive-strand RNA viruses are prenylated such as zinc finger antiviral protein (ZAP) and GBP1, GBP2, and GBP5(*105-107*).

The mevalonate pathway

The two key lipid molecules involved in prenylation, farnesyl pyrophosphate and geranylgeranyl pyrophosphate, are products of the mevalonate pathway or isoprenoid pathway. This metabolic pathway is responsible for the synthesis of many important biomolecules, including cholesterol and steroid hormones (*108*). Thus, regulation of this pathway can have consequences on protein prenylation which in turn can regulate prenylated proteins. The mevalonate pathway begins when HMG-CoA reductase (HMGR) converts HMG-CoA to mevalonic acid (Fig. 1.3). The reaction catalyzed by HMGR is the rate limiting step of this pathway. Also, HMGR is the target of the lipid-reducing class of drugs known as statins. The importance of statins in innate antiviral immunity will be discussed below. Mevalonic acid, through a series of reactions, is converted to geranyl pyrophosphate. Geranyl pyrophosphate is converted to farnesyl pyrophosphate by farnesyl diphosphate synthetase. Farnesyl pyrophosphate can be used as a substrate by farnesyltransferase I, converted to geranylgeranyl pyrophosphate and utilized by geranylgeranyl transferases, or converted to squalene and used in sterol synthesis (Fig. 1.3).

Given the important role products of the mevalonate pathway play in host processes such as cholesterol synthesis and prenylation, which in turn regulate process such as cellular signaling, it is not surprising that statin use impacts the immune system and inflammatory processes (*109, 110*). Additionally, positive-strand RNA viruses depend on host lipid biosynthesis pathways for lipid envelope production and generating membranous replication

organelles (*111*). Fascinatingly, different positive-strand RNA viruses utilize unique combinations of lipids to facilitate replication (*111*). Therefore, targeting specific host lipid biosynthetic pathways important for viral replication might represent an important therapeutic avenue for these viruses, while also blunting detrimental host inflammation.

As an example, statin use was found to decrease the severity of COVID-19 in individuals infected with SARS-CoV-2. In this retrospective study, statin use was correlated with a 4% decrease in COVID-19 mortality (*112*). Although the molecular mechanisms underlying this protection from severe disease was not explored, patients on statins did have lower levels of IL-6 and neutrophils compared to non-statin patients. This suggests an immunoregulatory role for statins in COVID-19. However, statin use likely involves regulation of host inflammatory pathways and virus replication. In support of the latter hypothesis, a recent study aimed at identifying host pathways critical for coronavirus replication found statin treatment can reduce coronavirus replication *in vitro (113)*. Thus, statin use might be doubly beneficial in some contexts by reducing both virus fitness and inflammatory cytokine production. Since many important metabolites are downstream of the molecular target of statins (HMGR), a more detailed investigation of the enzymes and metabolites important for SARS-CoV-2 replication and inflammatory mediator production would be beneficial. Applying this thinking to other positive-strand RNA viruses, an understanding of their utilization of the mevalonate pathway would allow us to generate host targeted therapies that may broadly restrict groups of positive-strand RNA viruses.

1.4 Unanswered questions

Does the innate immune system protect organelles from being hijacked by positive-strand RNA viruses?

Although all positive-strand RNA viruses generate ROs, the organelle membrane composition of the RO and their structure (i.e. positive vs negative membrane curvature) differs from virus to virus. It is conceivable the innate immune system may position factors capable of inhibiting the RO at organelle surfaces. Thus, antiviral activity can in part be rationalized or predicted by defining the specific organelle(s) to which an antiviral factor is targeted. Further, whether or not interferon or other antiviral signaling pathways impact organelle membrane composition in a way that makes them less susceptible to manipulation by positive-strand RNA viruses remains to be investigated.

In what subcellular compartment do RLRs sense viral RNA during positive-strand RNA virus infection?

There is no disputing the importance of RLRs for initiating a protective immune response to virtually all positive-strand RNA viruses. At some point during infection, these sensors bind viral RNA. However, the relative inaccessibility of the viral RNA to the cytosol and its confinement to the RO warrants a more detailed investigation of where RLRs are sensing viral RNA during infection. This is especially critical to address for MDA5, which has been shown to bind almost exclusively to viral double stranded RNA, an RNA species that is restricted to the RO and specifically the replicase complex (*67*). This suggests that, somehow, MDA5 does access the replication compartment or some mechanism exists to damage and reveal the RNA PAMPs contained within the RO.

1.5 Premise of this thesis

The ability of the host cell to mount an effective response to an infection depends its ability to sense the presence of an infection. The host accomplishes this by encoding PRRs capable of intercepting PAMPs. The host also deploys restriction factors that interface with viral products. In either case, the host must be able to access viral products. However, successful pathogen strategies include hiding PAMPs from innate immune surveillance. Positive-strand RNA viruses usurp host organelle membranes and construct replication organelles, which shield immunostimulatory viral RNA and viral proteins from innate immune detection and antagonism. Although ROs were initially thought resistant to innate immune interference, accumulating evidence suggests the innate immune system is indeed capable of inhibiting the RO and is also capable of accessing viral RNA and proteins within this compartment. However, a complete understanding of the host restriction factors capable of accessing the RO, and the mechanisms by which they gain access to this compartment, is lacking. We hypothesized antiviral proteins targeted to organelle membranes might have enhanced access to viral PAMPs contained within the RO. Specifically, in this thesis, we defined protein prenylation as mechanism by which host innate immune RNA binding proteins can be targeted to organelle membranes that are utilized for RO formation (Fig 1.4). Prenylation of these RNA binding proteins was required to localize these proteins to sites of viral RNA replication and was critical for their antiviral activity.

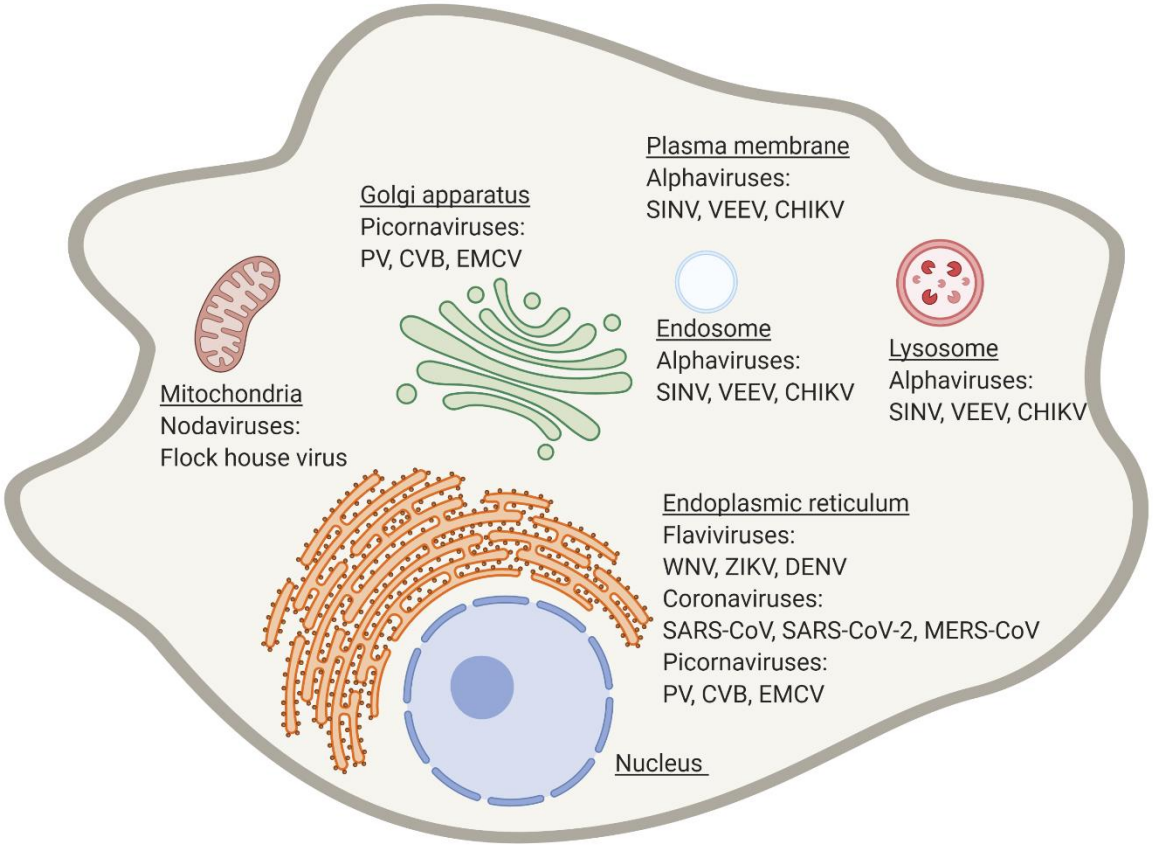

Figure 1.1. Organelles utilized by positive-strand RNA viruses for replication organelle formation.

Virtually all organelles are utilized by positive-strand RNA viruses for RO formation.

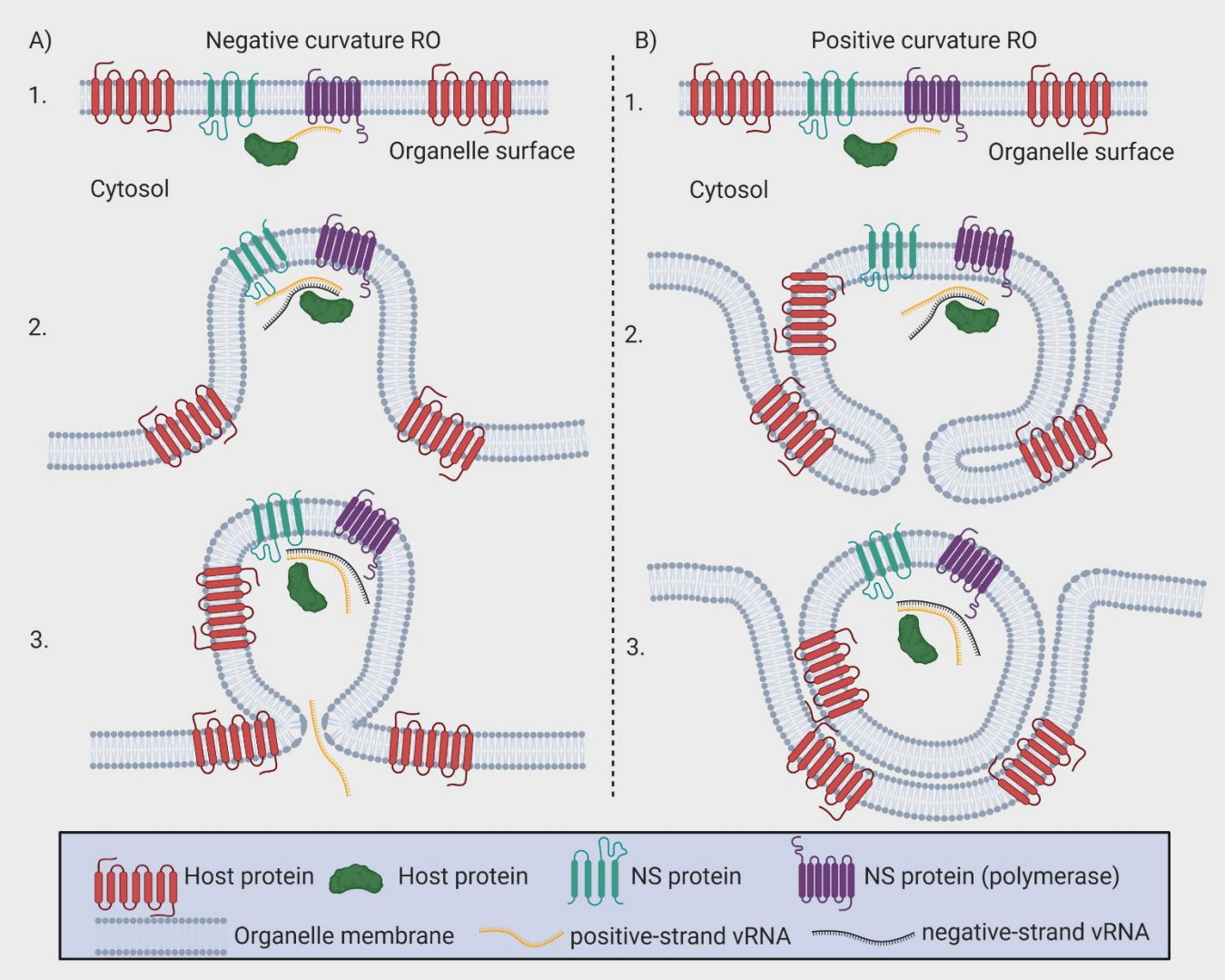

Figure 1.2. Architecture of replication organelles.

A) Negative curvature replication organelles (spherule type) are formed by invaginations of the organelle membrane into the luminal space. 1. The viral positive-strand RNA genome and non-structural proteins, including the RNA-dependent RNA polymerase, localize to the organelle membrane surface. 2. The organelle surface begins to involute due to negative membrane curvature induced by the non-structural proteins and host proteins. Viral RNA synthesis is also required for this process. 3. The mature replication organelle is formed and the negative strand RNA is copied into many positive-strand RNAs that serve as mRNA or are packaged into

virions. A narrow pore at the anterior of the replication organelle allows molecules such as RNA to be exported from this compartment **B)** Positive curvature replication organelles (double-membraned vesicle type) are formed by extrusions of the organelle membrane. 1. The viral positive-strand RNA genome and non-structural proteins, including the RNA-dependent RNA polymerase, localize to the organelle membrane surface. 2. Positive membrane curvature is generated by the viral non-structural proteins and host proteins. 3. Through unknown mechanisms, the membranes are paired and resolved generating a replication organelle with an inner enclosed membrane and an outer membrane that can be contiguous with the organelle membrane (shown) or wrapped around the inner membrane and not contiguous with the organelle membrane (not shown). Further, protein transporters and transient pores (not shown) may regulate the exchange of molecules across this type of replication organelle.

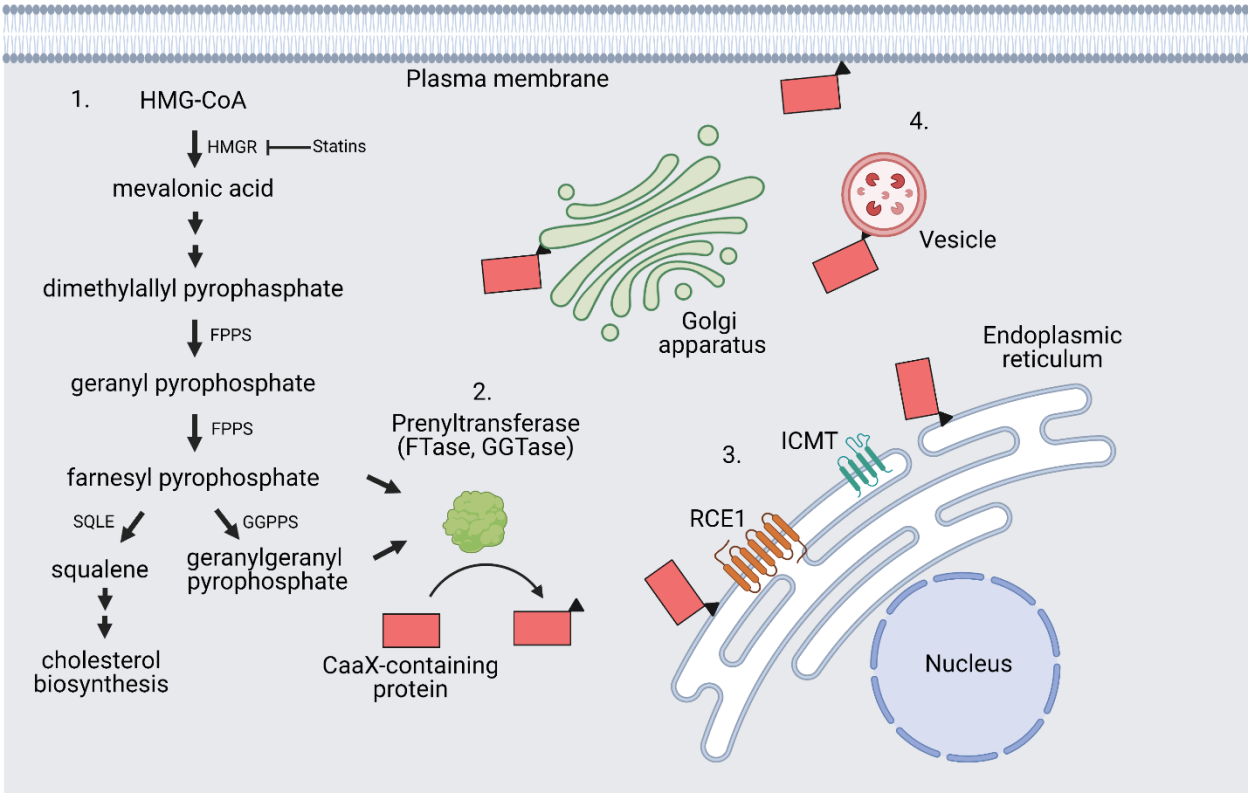

Figure 1.3. The mevalonate pathway and prenylation.

1. The mevalonate pathway. HMG-CoA is converted to mevalonic acid by HMG-CoA reductase (HMGR). A series of reactions follow to form dimethylallyl pyrophosphate, which is converted to geranyl pyrophosphate by farnesyl diphosphate synthase (FPPS). FPPS then converts geranyl pyrophosphate into farnesyl pyrophosphate, which can be used as a prenylation substrate by farnesyltransferase I. Farnesyl pyrophosphate can be converted to geranylgeranyl pyrophosphate via geranylgeranyl diphosphate synthase (GGPPS), which can then be used by geranylgeranyl transferases for geranylgeranylation. Farnesyl pyrophosphate can also be converted to squalene which is used for cholesterol synthesis. 2. Cytosolic prenyltransferases catalyze the covalent addition of farnesyl pyrophosphate or geranylgeranyl pyrophosphate to a CaaX-containing protein, which proceeds to localize to the endoplasmic reticulum or can interact with lipid

binding proteins (not shown). 3. Post prenylation processing occurs at the ER where the “aaX” peptide sequence is cleaved by RAS-converting CAAX endopeptidase 1 (RCE1) followed by the addition of a methyl group to the prenylcysteine by isoprenylcysteine carboxylmethyltranserase (ICMT). The addition of methyl group enhances the hydrophobicity and membrane affinity of the protein. 4. Prenylated proteins can remain in the ER or traffic primarily to organelles of the endomembrane system such as the Golgi apparatus, vesicles (endosomes, lysosomes) and the plasma membrane.

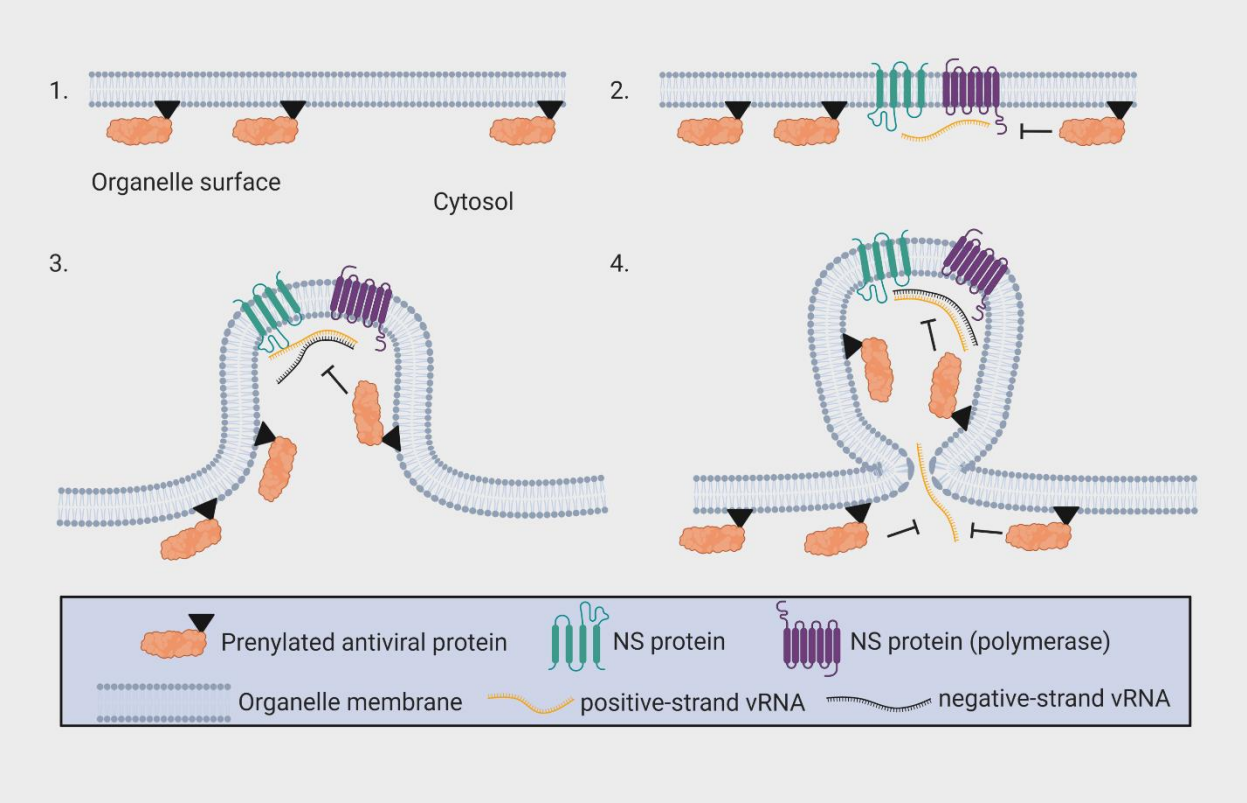

Figure 1.4. Targeting of antiviral effectors to the replication organelle via prenylation.

1. A prenylated antiviral RNA-binding protein is localizes to the cytosolic surface of an organelle membrane. 2. During infection with a positive-strand RNA virus the viral non-structural proteins and viral RNA are recruited to the organelle surface. Here, the antiviral protein can interact with viral RNA. 3. As the organelle membrane is involuted (a negative membrane curvature RO is depicted), the prenylated protein is also included in the replication organelle. Confinement in the RO may enhance access to viral RNA. 4. Newly prenylated proteins are continually recruited to the organelle surface during infection, which may allow for additional interference of viral RNA as it escapes the replication organelle.

Chapter 2. RNA-binding protein isoforms ZAP-S and ZAP-L have distinct antiviral and immune resolution functions

Johannes Schwerk*, Frank W. Soveg*, Andrew P. Ryan, Kerri R. Thomas, Lauren D. Hatfield, Snehal Ozarkar, Adriana Forero, Alison M. Kell, Justin A. Roby, Lomon So, Jennifer L. Hyde, Michael Gale Jr., Matthew D. Daugherty, and Ram Savan

*equal contribution

2.1 Introduction

Cells infected with viruses mount an antiviral response to block viral replication, alert neighboring cells to limit viral spread and ultimately clear the infection. Cell-intrinsic antiviral restriction factors are the first line of defense that prevent a virus from establishing a productive infection. Viral pathogen associated molecular patterns (PAMPs) that are sensed by host pattern recognition receptors (PRRs) trigger a signaling cascade that induces the synthesis of antiviral factors including type I and III interferons (IFNs). These IFNs are then secreted to induce an antiviral program in neighboring cells via activation of hundreds of IFN-stimulated genes (ISGs) (*71*), including factors that directly limit viral replication such as APOBECs, Mx and IFITs (*114-116*). Although a potent inhibitor of viral replication, the IFN response must be tightly regulated to prevent tissue damage. Despite the importance of returning to homeostasis post-infection, the mechanistic details underlying the attenuation of IFN responses after infection are poorly understood. One proposed mechanism for the resolution of IFN responses is the post-transcriptional regulation of immune genes. Specifically, the mRNAs of IFN and cytokines contain elements encoded within the 3′UTR, such as microRNA binding sites and motifs for

RNA-binding proteins (RBPs), that can destabilize mRNA (*117-120*). However, the RBPs that mediate clearance of IFN mRNAs have remained unknown.

The antiviral restriction factor ZAP (also known as PARP13; gene name *ZC3HAV1*) is an RNA-binding protein that targets viral RNA (vRNA) to inhibit viral replication. Its antiviral properties extend for several classes of viruses, including alphaviruses, filoviruses and retroviruses (*121-124*). ZAP contains tandem zinc-finger motifs that bind vRNA and shuttle it to the exosome for degradation (*125, 126*). Early studies were carried out under the assumption that only one isoform of ZAP exists. Subsequent studies identified a long isoform of ZAP, named ZAP-L, generated from the same *ZC3HAV1* gene and which contains an additional C-terminal catalytically inactive poly ADP-ribose polymerase (PARP) domain (*127, 128*). Because both ZAP-L and ZAP-S contain identical N-terminal zinc-finger motifs that can bind RNA, it is unclear if the isoforms play independent or overlapping roles in coordinating the innate antiviral immune response.

In this study, we show that ZAP-S and ZAP-L have distinct functions during the innate antiviral immune response. ZAP-S was induced late after immune activation and bound and negatively regulated *IFN* mRNA to blunt immune responses downstream of IFN. In contrast, the ZAP-L isoform was expressed constitutively and was the primary antiviral effector. We found that differential subcellular localization of the two isoforms, mediated by the presence or absence of a C-terminal prenylation motif, was the principal determinant of the distinct activities of ZAP-L and ZAP-S. Our data provides mechanistic insights into the distinct localization and expression kinetics of ZAP isoforms, which conferred differential target-RNA specificity and opposing functions during viral infection.

2.2 Results

2.2.1 ZAP-S interacts with the 3′UTR of IFN mRNAs

AU-rich elements (AREs) in the 3′UTR of *IFNL3* are required for the rapid decay of the *IFNL3* mRNA (*118*). To identify the RBPs that bind to the ARE of *IFNL3* specifically, we performed a mass-spectrometry screen for candidate proteins that are recruited to the 3′UTR of wild-type *IFNL3* mRNA (WT *IFNL3*), but not to the 3′UTR in which the AREs were mutated (ΔAREs; AUUUA>AUCUA). Biotinylated WT *IFNL3* or ΔAREs 3′UTRs (Fig 2.1 A) were incubated with whole cell lysates from HepG2 hepatoma cells, streptavidin-affinity purified and subjected to mass spectrometry. Of the candidate proteins that bound to either *IFNL3* 3′UTR, ZAP-S showed the highest relative preference to bind to WT *IFNL3* (Fig 2.1 B). Next, Huh7 cells were transfected with either FLAG-tagged ZAP-S or ZAP-L and stimulated with the RIG-I ligand poly U/UC RNA to induce expression of endogenous *IFNL3* mRNA (Fig 2.1 C). FLAG-tagged ZAP-S or ZAP-L were then affinity-purified, and the co-precipitated total RNA was probed for *IFNL3* mRNA by qPCR. *IFNL3* mRNA was significantly enriched in the ZAP-S RNA immunoprecipitation (RIP) fraction, but not in the ZAP-L RIP fraction, even though ZAP-L and ZAP-S have identical RNA-binding zinc-finger motifs (*127*) (Fig 2.1 C,D). Because *IFN* genes share similar instability motifs, we also tested if ZAP-S bound to other *IFN* mRNAs. We observed enrichment of *IFNL1*, *IFNL2* and *IFNB* mRNA in the ZAP-S RIP fractions, while ZAP-L RIP fractions did not show significant enrichment of *IFN* mRNA over IgG control (Fig 2.1 D). RIP under UV-crosslinking conditions, to exclude a potential post-lysis re-assortment of ZAP and its target RNAs, indicated enrichment of *IFN* mRNAs in the ZAP-S RIP fractions compared to ZAP-L and empty vector (EV) RIP fractions (Fig S2.1 A). We next performed RIP of *IFN* mRNA and endogenous ZAP in Huh7 hepatocytes. In Huh7 cells lacking functional type

I IFN receptor (*IFNAR1*$^{-/-}$), which did not express ZAP-S after stimulation with poly U/UC RNA, less *IFNB* mRNA was pulled down compared to wild-type Huh7 cells, which expressed ZAP-S (Fig S2.1 B). These data suggested that ZAP-S, but not ZAP-L, was specifically recruited to several host immune genes by recognition of 3′UTR motifs that contain AU-rich elements.

2.2.2 ZAP-S induction is delayed and is dependent on IFN signaling

Because induction of ZAP-S is dependent on type I IFN signaling(*129-131*) we assessed the expression kinetics of ZAP-S and ZAP-L upon stimulation of Huh7 hepatocytes with poly U/UC RNA and IFN. While ZAP-L protein was expressed constitutively in mock-transfected wild-type Huh7 cells, expression of ZAP-S protein was detected no sooner than 24 h post stimulation with poly U/UC RNA (Fig 2.1 E). We observed reduced expression of ZAP-S in *IFNAR1*$^{-/-}$ Huh7 cells compared to Huh7 wild-type cells (Fig 2.1 E), indicating that induction of ZAP-S was dependent on type I IFN receptor signaling. Stimulation of *IRF3*$^{-/-}$ Huh7 cells with poly U/UC RNA did not induce the expression of ZAP-S protein at 48 h after stimulation, whereas stimulation of *IRF3*$^{-/-}$ Huh7 cells with recombinant IFN-α2 led to robust expression of ZAP-S at 48 h (Fig 2.1 F), indicating that expression of ZAP-S upon virus-like PAMP stimulation was IRF3-dependent. Furthermore, stimulation of wild-type and *STAT1*$^{-/-}$ PH5CH8 hepatocytes cells with recombinant IFN-β, IFN-λ3 and IFN-γ led to ZAP-S expression in wild-type PH5CH8 cells, but not in *STAT1*$^{-/-}$ PH5CH8 cells (Fig 2.1 G,H), indicating that expression of ZAP-S was dependent on intact STAT1 signaling. These data showed that ZAP-L was constitutively expressed, while the expression of ZAP-S occurred no sooner than 24 h after stimulation and was dependent on IFN signaling.

2.2.3 CSTF2-mediated alternative polyadenylation generates ZAP-S

Alternative splicing was proposed to mediate the expression of ZAP-L and ZAP-S from the same gene (*127*). We found that the ZAP-S mRNA utilized the first 694 base pairs of the intron between exons 9 and 10 as a 3′UTR and that this 3′UTR deployed a weaker non-canonical polyadenylation signal, AGUAAA (Fig 2.2 A). Because the induction of ZAP-S expression was dependent on type I IFN receptor signaling, we designed a ZAP-S splicing PCR assay that allowed us to detect the usage of the proximal non-canonical polyadenylation signal of ZAP-S, compared to skipping of this polyadenylation signal and expression of ZAP-L. Treatment of wild-type Huh7 cells with recombinant IFN-β led to a strong increase in usage of the alternative polyadenylation signal and 3′UTR of ZAP-S, which was absent in untreated wild-type Huh7 cells and IFN-β-treated *IFNAR1*$^{-/-}$ Huh7 cells (Fig 2.2 B). ZAP-L expression was independent of type I IFN signaling (Fig 2.2 B). Additionally, qPCR using isoform-specific ZAP probes in wild-type and IFNAR1-/- Huh7 cells after stimulation with IFN-β confirmed the validity of the ZAP-S splicing PCR assay (Fig 2.2 C).

We next investigated the factors that bound to the 3′UTR of ZAP-S and induced its expression. Analysis of the ZAP-S 3′UTR indicated a conserved upstream element (USE) and a downstream element (DSE), which are required for recruitment of the cleavage factor CSTF2 (also known as CstF-64) and the CSTF2-dependent processing of weak non-canonical polyadenylation signals (*132-134*), flanking the non-canonical polyadenylation signal of ZAP-S. We used the ZAP-S splicing PCR assay to test if CSTF2 was involved in the generation of ZAP-S in Huh7 cells through alternative polyadenylation cells upon knockdown of CSFT2 and treatment with IFN-β. Usage of the non-canonical polyadenylation signal in ZAP-S was reduced in Huh7 cells upon siRNA-mediated knockdown of CSTF2 compared to non-targeting control

(NC) siRNA, whereas expression of ZAP-L in Huh7 cells was unaffected by the knockdown of CSTF2 compared to non-targeting control (NC) siRNA (Fig 2.2 D, E). More importantly, ZAP-S protein expression was decreased in Huh7 wild-type cells upon siRNA-mediated knockdown of CSTF2 and stimulation with recombinant IFN-β, compared to non-targeting control (NC) siRNA, whereas expression of ZAP-L protein remained unaltered (Fig 2.2 F). Collectively, these data indicated that the ZAP-S isoform was generated by alternative polyadenylation through a mechanism that involved type I IFN signaling and the polyadenylation factor CSTF2.

2.2.4 ZAP-deficient cells have a higher and more prolonged IFN response

ZAP recruits target viral RNAs to the exosome machinery to mediate decay of bound viral RNAs (*124, 126, 135*). To test whether ZAP-S deployed a similar decay machinery to dampen the IFN response, we generated ZAP-deficient Huh7 hepatoma cells by using the CRISPR/Cas9 technology and guide RNA targeting the first exon of ZAP, which is required for the expression of both ZAP isoforms, and isolated single ZAP isoforms-deficient Huh7 cell clones (hereafter ZAP KO Huh7 cells) from a heterogeneous cell population (Fig 2.3 A and Fig S2.2 A-E). ZAP KO Huh7 cells had increased expression of *IFNB*, *IFNL2* and *IFNL3* mRNA after stimulation with poly U/UC RNA compared to wild-type Huh7 cells (Fig 2.3 B), suggesting ZAP KO Huh7 cells could not control IFN production upon a virus-like insult. To test whether ZAP was critical to resolve the IFN response, we performed a time course analysis of IFN expression after stimulation of wild-type and ZAP KO Huh7 cells with poly U/UC RNA. To exclude the effects of differential uptake of the stimulus, cells were pulsed with transfected poly U/UC RNA for 2 h. While induction of *IFNB* mRNA was maximal at 12 h and resolved at 36 h post stimulation in wild-type Huh7 cells, the ZAP KO Huh7 cells showed about 20-fold elevated

peak expression at 12 h and delayed resolution of *IFNB* mRNA between 12 and 36 h compared to wild-type Huh7 cells (Fig 2.3 C). Similarly, expression of *IFNL3* mRNA was significantly higher (5-fold) and exhibited delayed resolution between 12 and 36 h in ZAP KO Huh7 cells compared to wild-type Huh7 cells (Fig 2.3 C). Sustained and increased expression of *IFN* mRNA was substantiated by the 6 to 16-fold increased expression of ISGs mRNA (*IFIT1* and *ISG15*) at 24 and 48 h after poly U/UC RNA stimulation and ISG protein (ISG15 and RIG-I) 48 h post poly U/UC RNA stimulation in ZAP KO Huh7 cells compared to wild-type cells (Fig 2.3 D, E). Importantly, the basal expression of RIG-I protein, the cytosolic sensor of poly U/UC RNA, and IRF3 protein were similar between unstimulated wild-type and ZAP KO Huh7 cells (Fig 2.3 E). Stimulation with recombinant IFN-β did not result in sustained and increased expression of ISG mRNA and protein in ZAP KO Huh7 cells compared to wild-type cells (Fig 2.3 F, G). Furthermore, polysome fractionation indicated that neither ZAP-S nor ZAP-L interacted with actively translating polyribosomes (Fig 2.3 H). Treatment of wild-type Huh7 cells with harringtonine, an inhibitor of translation initiation, resulted in the disruption of polyribosomes, as indicated by the polysome traces, and a shift of the ribosomal protein S6 towards the lighter non-polysome fractions (Fig 2.3 H). ZAP-S and ZAP-L did not co-sediment with S6 in the absence of harringtonine, and a shift in the sedimentation pattern of ZAP-S and ZAP-L was not observed in the presence of harringtonine (Fig 2.3 H). Furthermore, overexpression of ZAP-S and ZAP-L did not affect the amount of *IFNB* and *HPRT* mRNA loaded on actively translating polyribosomes compared to EV control (Fig. S2.2 F), indicating that differences in overall mRNA translation and protein synthesis were not a major contributor to the prolonged, elevated IFN mRNA in ZAP KO Huh7 cells compared to wild-type cells. These experiments indicated that ZAP-S expression promoted the resolution of IFN-mediated immune responses.

2.2.5 ZAP-S and ZAP-L localize to different subcellular compartments

Mouse ZAP-L was shown to be targeted to endolysosomal membranes by a C-terminal CaaX ('C' cysteine, 'a' aliphatic amino acid, 'X' variable amino acid) motif that can be prenylated by S-farnesyltransferases (*105*) (Fig 2.4 A). Prenylation is a post-translational modification that renders proteins hydrophobic, thereby tethering them to membranes (*102*). To investigate whether ZAP-S and ZAP-L occupied distinct subcellular compartments, that would give them differential access to unique pools of RNA, we carried out immunofluorescence staining and confocal microscopy of ZAP isoforms in ZAP KO Huh7 cells co-transfected with Myc-tagged ZAP-S and FLAG-tagged ZAP-L. Myc-ZAP-S had a diffuse cytoplasmic distribution, while FLAG-ZAP-L aggregated in condensed foci, with no overlap between Myc-ZAP-S and FLAG-ZAP-L (Fig 2.4 B). Next we used structured illumination microscopy (SIM), a super-resolution microscopy which doubles the lateral resolution over conventional confocal laser scanning microscopy (*136*), to obtain higher resolution of ZAP isoform localization. SIM indicated that Myc-ZAP-S and FLAG-ZAP-L did not co-localize within ZAP KO Huh7 cells, and that Myc-ZAP-S occupied the cytosolic compartment while FLAG-ZAP-L occupied a population of vesicles (Fig 2.4 C). Tagless ZAP-S and ZAP-L detected by antibody staining showed similar subcellular distribution in ZAP KO Huh7 cells as their tagged counterparts (Fig 2.4 D), thereby excluding an influence of the Myc and FLAG tags on the subcellular localization. Staining of wild-type and ZAP KO Huh7 cells confirmed the specificity of the antibody for endogenous ZAP (Fig S2.3 A).

To identify the subcellular localization of human ZAP-L, we co-expressed tagless ZAP-L and ZAP-S along with mCherry-tagged organelle markers for LAMP1 (lysosome), Rab5 (early endosome), Rab7 (late endosome), Sec61β (endoplasmic reticulum), PTS1 (peroxisome) and

COX8 (mitochondria). Immunofluorescence staining showed that tagless ZAP-L, but not tagless ZAP-S, co-localized with the lysosomal marker LAMP1 (Fig 2.4 E, F), and also co-localized with $Rab5^+$ and $Rab7^+$ vesicles in the endosomal pathway (Fig 2.4 F, Fig S2.4 A, B and Table 2.1). SIM indicated that ZAP-L specifically localized to the membranes of $LAMP1^+$ endolysosomes. Although ZAP was in proximity to the endoplasmic reticulum (ER), we did not observe isoform-specificity to the co-localization of tagless ZAP-L or tagless ZAP-S with the ER by immunofluorescence microscopy (Fig S2.5 A, B). We did not observe the co-sedimentation of ZAP-S and the ER-marker calnexin in a membrane flotation assay (Fig S2.5 C). Furthermore, we did not observe the co-localization of tagless ZAP-L with peroxisomes or mitochondria (Fig S 2.5 D, E and Table 2.1).

To ask whether the C-terminal CaaX motif was necessary and sufficient for the differential subcellular localization of ZAP-L and ZAP-S, we generated two expression constructs in which we either mutated the ZAP-L CaaX motif (ZAP-L SVIS) or added a CaaX motif to ZAP-S (ZAP-S+CVIS) (Fig 2.4 A). When expressed in ZAP KO Huh7 cells, ZAP-L SVIS did not overlap with the endolysosomal markers Rab5, Rab7 and LAMP1 and had a diffuse cytoplasmic distribution, which resembled the cytosolic localization of wild-type ZAP-S (WT ZAP-S) (Fig 2.4 D-F and Fig S2.4 A,B). Expression of ZAP-S+CVIS in ZAP KO Huh7 cells led to formation of distinct foci positive for LAMP1, Rab5 and Rab7 staining, as seen for WT ZAP-L (Fig 2.4 E, F and Fig S2.3A, 2.4 A, B), indicating a gain of endolysosomal localization through the addition of a CaaX motif to the C-terminus of ZAP-S. To confirm the immunofluorescence data, we carried out subcellular fractionation of ZAP KO Huh7 cells overexpressing WT ZAP-S, WT ZAP-L, ZAP-L SVIS or ZAP-S+CVIS. WT ZAP-S and ZAP-L SVIS were detected in the cytosol, whereas little to no WT ZAP-L or ZAP-S+CVIS were detected in the cytosol (Fig S2.3

B), consistent with our microscopy data. This data shows that absence of presence of the CaaX motif determines the differential subcellular localization of ZAP-S and ZAP-L isoforms.

2.2.6 ZAP-L targets alphavirus RNA at viral replication sites

ZAP has strong antiviral activity against members of the *Alphavirus* genus of the *Togaviridae* family (*121, 127, 137*) and overexpression of ZAP-L inhibits alphaviruses to a greater extent than ZAP-S (*105, 127*). To ask whether ZAP showed isoform-specific localization to the replication sites of the alphavirus Sindbis virus (SINV), we infected ZAP KO Huh7 cells overexpressing tagless ZAP-L or ZAP-S with SINV strain Toto and performed immunofluorescence staining of ZAP and SINV dsRNA replication intermediates. ZAP-dense foci formed around SINV dsRNA in ZAP-L-overexpressing ZAP KO Huh7 cells (Fig S2.5 A). ZAP KO Huh7 cells overexpressing ZAP-S formed few such foci, which were also smaller in size compared to those formed by ZAP-L (Fig 2.5 A). To test if endogenous ZAP-L co-localized with SINV replication intermediates, we infected wild-type Huh7 cells with SINV (strains Toto and AR86) and stained for endogenous ZAP and SINV dsRNA replication intermediates 6 h post-infection. Endogenous ZAP-L co-localized with SINV (Toto and AR86) RNA replication intermediates (Fig 2.5 B). Importantly, endogenous ZAP-S was not expressed at this time point (Fig 2.5 C), indicating that the immunofluorescence signal from ZAP was derived from endogenous ZAP-L only. The co-localization of ZAP-L with SINV RNA occurred at the plasma membrane and in conjunction with G3BP1-positive stress granules, where SINV, like other alphaviruses, assembles its replication sites (*6*) (Fig 2.5 B and Fig S2.6 A, B). To address if the co-localization of ZAP-L with SINV RNA required immune activation by the host cell, we infected *IRF3*$^{-/-}$ Huh7 cells, which do not induce IFN or expression of ZAP-S upon PAMP

stimulation or viral infection, with SINV Toto for 6 h. Endogenous ZAP-L co-localized with SINV RNA at the cell membranes of *IRF3*$^{-/-}$ Huh7 cells**,** similar to wild-type Huh7 cells (Fig 2.5 D), indicating that endogenous ZAP-L preferentially localized to viral RNA and sites of SINV replication on membranes even in the absence of IRF3-mediated innate immune signaling.

To test if the subcellular localization of the ZAP isoforms influenced their antiviral activity against SINV, we generated doxycycline-inducible HEK 293 cells expressing WT ZAP-S, WT ZAP-L, ZAP-L SVIS or ZAP-S+CVIS and infected them with SINV. Supernatants harvested from WT ZAP-L HEK 293 cells infected with SINV showed a strong inhibition (20,000-fold) of viral replication compared to control EV expressing cells, whereas WT ZAP-S-expressing HEK 293 cells showed a much lower degree of inhibition (60-fold) (Fig 2.5 E). Expression of ZAP-L SVIS decreased the antiviral activity to levels observed in WT ZAP-S-expressing HEK 293 cells (Fig 2.5 E), while expression of ZAP-S+CVIS led to increased (2,000-fold) antiviral capacity, although 10-fold less than that induced by WT ZAP-L (Fig 2.5 E). We also used a replicon-based system for another alphavirus, Semliki Forest virus (SFV) (*138*), which allowed the expression of increasing amounts of the ZAP expression constructs. Overexpression of WT ZAP-L was the most efficient at blocking SFV replication, with ZAP-S+CVIS the second most inhibitory compared to control cells that did not overexpress a plasmid (Fig S2.6 C). WT ZAP-S and ZAP-L-SVIS were the least inhibitory (Fig S2.6 C). To confirm that the effects observed in the overexpression experiments were relevant in the context of endogenously expressed ZAP isoforms, we used an siRNA approach to selectively knock down ZAP-L or ZAP-S during SINV infection in Huh7 cells. We designed isoform-specific siRNAs that either target the 3′UTR of ZAP-S, which is absent in ZAP-L, or exon 12 in ZAP-L, which is absent in ZAP-S, and confirmed their specificity by immunoblot (Fig 2.5 F). Knockdown of

ZAP-L, but not ZAP-S, in Huh7 cells resulted in increased SINV replication (Fig 2.5 G), indicating that ZAP-L was the major antiviral ZAP isoform during alphavirus infection and that ZAP-S had a minimal role in direct antiviral immunity against alphaviruses. These results indicated that the isoform-specific targeting of viral RNA was due to differences in the subcellular localization of ZAP-S and ZAP-L, which were determined by the presence or absence of the C-terminal CaaX motif and allowed the recruitment of ZAP-L to sites of SINV RNA replication at endolysosomes and the plasma membrane.

2.2.7 ZAP-S, but not ZAP-L, suppresses IFN

To address which ZAP isoform was responsible for the increased expression of *IFN* mRNA in ZAP KO Huh7 cells, we performed isoform-specific ZAP siRNA knockdown experiments. Wild-type Huh7 cells were co-transfected with ZAP-L (exon 12) siRNA or ZAP-S (3′UTR) siRNA and poly U/UC RNA to induce expression of IFN and endogenous ZAP-S protein. Transfection of ZAP-S siRNA led to significantly higher expression of *IFNB*, *IFNL2* and *IFNL3* mRNA compared to non-targeting control (NC) siRNA and ZAP-L siRNA (Fig 2.6 A, B). IRF3 phosphorylation was similar in ZAP-L, ZAP-S and NC siRNA transfected cells (Fig 2.6 A), indicating activation of IRF3 was not affected by knockdown of either ZAP isoform. ZAP-S was reported to co-operate with RIG-I to increase RIG-I-mediated IFN responses in HEK 293 cells (*129*), but knockdown of ZAP-S led to increased IFNB and IFNL3 mRNA in 293 cells compared to ZAP-L knockdown and NC siRNA upon stimulation with poly U/UC RNA (Fig S2. 7 A, B). *TNFA* and *IL6* mRNA harbor AREs in their 3′UTRs. *IL6* mRNA was significantly increased upon ZAP-S knockdown in Huh7 cells, while *TNFA* mRNA was not as affected (Fig S2.7 C), although both *IL6* and *TNF* transcripts are bound by the ZAP-S preferentially compared

to ZAP-L or EV control (Fig S2.7 D). Overexpression of the phosphomimetic IRF3-5D, which bypasses the signaling pathways upstream of IRF3 activation, led to increased *IFNB* mRNA in ZAP-S-knockdown Huh7 cells compared to ZAP-L-knockdown or NC Huh7 cells (Fig 2.6 C, D). Stimulation of CAL-1 pDC cells with R848, a TLR7 ligand that signals through IRF7 resulted in increased induction of *IFNL2* and *IFNL3* mRNA in ZAP-S-knockdown CAL-1 cells only (Fig 2.6 E, F). Additionally, overexpression of IRF1 in ZAP KO Huh7 cells led to significantly increased *IFNB* and *IFNL3* mRNA compared to wild-type Huh7 cells (Fig 2.7 E, F), indicating that the effect of ZAP-S on *IFN* mRNA was not caused by the dysregulation of upstream signaling pathways due to knockdown of ZAP-S. These data indicated that the increased expression of IFN in ZAP KO Huh7 cells was not only specific to the RIG-I-IRF3 signaling axis and that ZAP-L had a minor role in the resolution of IFN responses.

2.2.8 Localization of ZAP isoforms determines binding of *IFN* mRNA

To test if the cytoplasmic localization of ZAP-S determined whether ZAP-S, but not ZAP-L, could target and negatively regulate *IFN* mRNA, we carried out RIP with FLAG-tagged WT ZAP-S, WT ZAP-L, ZAP-L SVIS or ZAP-S+CVIS in ZAP KO Huh7 cells. The disruption of the CaaX motif in the ZAP-L SVIS mutant resulted in increased enrichment of *IFNB* and *IFNL3* mRNA compared to ZAP-L WT, while addition of the CaaX motif to ZAP-S in the ZAP-S+CVIS mutant led to a decrease in its ability to target *IFNB* and *IFNL3* mRNA compared to ZAP-S WT (Fig 2.7 A), suggesting the CaaX motif was a major determinant for target RNA specificity of ZAP isoforms. To test whether increased IFN expression resulting from a loss of ZAP-S decreased the replication of viruses sensitive to IFN, we used SINV and vesicular stomatitis virus (VSV), both of which are sensitive to the antiviral effects of IFN, while only

SINV is sensitive to ZAP-L mediated restriction. We observed elevated SINV replication in the ZAP KO Huh7 cells compared to wild-type Huh7 cells in unstimulated conditions (Fig 2.7 B), indicating the intrinsic restriction of SINV replication by constitutive ZAP-L. In contrast, we saw no difference in VSV replication between wild-type and ZAP KO Huh7 cells (Fig 2.7 B), indicating VSV was insensitive to ZAP expression. Both SINV and VSV were more sensitive to IFN-mediated restriction after poly(I:C) stimulation in ZAP KO Huh7 cells compared to wild-type Huh7 cells (Fig 2.7 B), suggesting that increased IFN levels in ZAP KO Huh7 cells compared to wild-type Huh7 cells have a direct biologically effect on replication of IFN-sensitive viruses. These results show that the isoform-specific binding of ZAP-S to *IFN* mRNA to resolve the antiviral IFN response is determined by its cytosolic localization due to the lack of a C-terminal CaaX motif (Fig S2.8).

2.3 Discussion

Here we found that the innate antiviral immune factor, ZAP has a role in the negative regulation of the immune response. In contrast to the direct antiviral role of the long isoform, ZAP-L, we found that the shorter isoform, ZAP-S, targeted host *IFN* mRNAs to resolve IFN-mediated inflammatory responses. The distinct self-versus non-self RNA recognition by ZAP-S and ZAP-L is linked to differential expression kinetics and subcellular localization, which was determined by prenylation of a C-terminal CaaX motif.

Previous studies have described the antiviral effect of ZAP, mediated through direct binding of viral RNA and RNA degradation (*121, 125, 126, 135, 139, 140*). ZAP-S and ZAP-L share an identical N-terminal RNA-binding motif, proposed to be transcribed from the same gene (*ZC3HAV1*) through alternative splicing (*127*). Our studies show IFN-induced and CSTF2-dependent alternative polyadenylation leading to alternative last exon usage and generation of

ZAP-S. Expression of CSTF2 in immune cells is dependent on the activation status of the cell, with a direct effect on alternative polyadenylation of mRNA (*132-134*). Type I IFN-dependent induction of CSTF2 has been reported(*141*). While we did not observe altered expression of CSTF2 after IFN or PAMP stimulation, we do not rule out changes in post-translational modifications of CSTF2 protein, or stimulus-dependent changes in the amounts of CSTF2 co-factors required for its activation.

The motif on the viral RNA that is recognized by ZAP has been elusive, with early papers suggesting that RNA structure-dependent recognition whereas more recent papers indicate that ZAP binds to regions with high CG dinucleotide content (*142, 143*). Regardless of the exact target RNA motif, the identical zinc-finger domains of ZAP-S and ZAP-L (*142, 144*) cannot impart the differential specificity of ZAP isoforms for host *IFN* mRNA sequences. The longer C-terminus of ZAP-L contains a catalytically inactive poly ADP-ribose polymerase (PARP) domain (*127*) and a functional CaaX prenylation motif (*105*), which are absent in the ZAP-S isoform. We found that the subcellular localization of ZAP-S and ZAP-L predominantly determined the functional differences observed between the isoforms targeting host and viral RNAs, respectively. Through overexpression and isoform-specific knockdown experiments, we establish that ZAP-L is the dominant antiviral isoform against SINV, which is consistent with previous observations (*105, 127*). However, the fact that we could not fully mirror ZAP-L activity by simple re-localization of ZAP-S through the addition of the CaaX motif might be due to the requirement of additional amino acid residues in the C-terminal part of ZAP-L, specifically in the PARP domain, which could provide antiviral functions or additional localization signals. While the PARP domain of ZAP-L lacks the catalytic activity of functional PARPs, the mutations causing PARP inactivity are essential for the antiviral activity of ZAP-L

against alphaviruses (*145*), suggesting that RNA-binding activity might not be the only antiviral mechanism conferred by ZAP (*146*). We propose that the primary determinant for higher antiviral activity of ZAP-L over ZAP-S was due to the proximity of ZAP-L to sites of alphavirus replication at the plasma membrane and in endolysosomes with highly abundant vRNA ligands. Prenylation and targeting of ZAP-L to these sites positioned ZAP-L in close proximity to the viral RNA, which might also explain the antiviral specificity of ZAP-L against alphaviruses.

ZAP-S knockdown had specific effects on certain mRNAs and did not affect general mRNA turnover. Although the common feature of *IFNB, IFNL1-3, IL6* and *TNFA* mRNAs is the presence of AREs in their 3'UTRs that could be preferentially bound by ZAP-S, we cannot rule out additional motifs aside from the AREs that might determine the specificity of ZAP-S-mediated mRNA regulation. Similar to AREs in human cytokine mRNAs, alphaviruses harbor U-rich elements in their genome. This raises the possibility that the zinc-finger motifs of ZAP-L and ZAP-S target similar motifs in host and viral RNA. The exact RNA structure and motifs recognized by ZAP warrants further investigation.

We observed that the replication of IFN-sensitive viruses was attenuated due to elevated and sustained IFN production in the absence of ZAP-S. This provides a mechanistic explanation for two previous observations in the ZAP literature: First, a previous study using an *in vivo* infection model of ZAP-deficient mice with a neurovirulent Sindbis virus strain reported opposing phenotypes depending on the age of the mice (*147*). Suckling ZAP KO mice, which lack a fully developed immune system, were highly susceptible to SINV (*147*). Weanling ZAP-deficient mice, whose immune system is more developed, showed improved survival, along with increased expression of IFN compared to wild-type mice (*147*). Based on our data we suggest that suckling ZAP-deficient mice would succumb to infection due to lack of the direct antiviral

properties of ZAP-L. Weanling ZAP-deficient mice however could benefit from increased IFN expression due to lack of ZAP-S. Future *in vivo* studies are required to dissect individual contributions of ZAP-L and ZAP-S to innate antiviral immunity.

Second, codons that have undergone recurrent positive selection throughout primate evolution, which might indicate the regions of ZAP that are recognized by viral antagonists, are only found in the catalytically inactive C-terminal PARP domain of ZAP-L (*127*). Our data could indicate that ZAP-S might act as an evolutionary 'shield' that protects the remainder of the protein from antagonism. If a viral protein were to prevent ZAP-L function by binding to the N-terminus of the protein, it would also disrupt ZAP-S activity and therefore increase the IFN response. This theory could also explain isoform-specific signatures of positive selection found in other genes. It would be interesting to know if viruses possess mechanisms to selectively increase expression of or stabilize ZAP-S in order to attenuate the IFN response and promote viral replication.

Collectively, our study reveals that the host can diversify the function of RNA-binding protein isoforms to exert unique cellular functions through distinct expression kinetics subcellular localization, highlighting that differential intracellular targeting is an important mechanism controlling the target RNA specificity of RNA-binding proteins.

2.4 Materials and methods

Cell culture conditions.

All cells were incubated at 37 °C with 5% CO_2. Huh7, HepG2, PH5CH8 and HEK 293 cells were cultured in DMEM (Sigma) containing 10% heat-inactivated FBS (Atlanta Biologicals) and 1% penicillin-streptomycin-glutamine (Mediatech). BHK cells were cultured in

MEM (Sigma) containing 10% heat-inactivated FBS (Atlanta Biologicals) and 1% penicillin-streptomycin-glutamine (Mediatech). CAL-1 cells were grown in RPMI 1640 (Sigma) containing 10% heat-inactivated FBS (Atlanta Biologicals) and 1% penicillin-streptomycin-glutamine (Mediatech), and supplemented with 2 mM L-Glutamine, 1 mM sodium pyruvate, 10 mM HEPES, 1x MEM NEAA (Corning).

Stimulations.

Recombinant human IFN-α2, IFN-β, IFN-λ3 (PBL Interferon Source) and IFN-γ (Shenandoah Biotechnology) were used at 25-100 ng/ml (IFN-α2), 25-500 IU/ml (IFN-β), 100 ng/ml IFN-λ3 or 5 ng/ml (IFN-γ), respectively. For RIG-I stimulations, poly U/UC RNA was synthesized by *in vitro* transcription as previously described (*148*). Poly U/UC RNA was transfected at 0.2-1 µg/ml using *Trans*IT-X2 (Mirus Bio) according to the manufacturer's instructions. Stimulations of TLR3 and TLR7/8 were performed using 10 µg/ml floating poly(I:C) or 1 µg/ml R848 (both InvivoGen) in culture media.

RNA isolation, reverse transcription and quantification of gene expression.

Total RNA was isolated using the NucleoSpin RNA kit (Macherey-Nagel) according to the manufacturer's protocol. cDNA was synthesized from 1 µg total RNA using the QuantiTect RT kit (Qiagen) according to manufacturer's instructions. qPCR was carried out using the ViiA7 qPCR system with *Taq*Man reagents using *Taq*Man primers/probes (Life Technologies) for *IFNB*, *IFNL1*, *ISG15*, *IFIT1*, *MX1*, *OAS1*, *TNFA*, *IL6*, *ZC3HAV1*, *CSTF2*, *HPRT*, *GAPDH* and custom-designed, isoform-specific probes for ZAP-S and ZAP-L (Supplementary Table 1). *Taq*Man primers/probes for *IFNL2* and *IFNL3* were previously designed and tested for

specificity (*118, 149*). Target gene expression was normalized to *HPRT* or *GAPDH* housekeeping genes.

Western blot.

Cells were lysed in RIPA buffer (+ 1x HALT protease and phosphatase inhibitor and 10-30 μg total protein from whole cell lysates was run on SDS-PAGE and transferred to PVDF membranes (Thermo Scientific). The membranes were probed in 5 % BSA or milk in PBS-T (Phosphate-buffered saline/Tween 20) for ZAP (N3C2, GeneTex), ISG15 (Cell Signaling, #2743), OAS1 (D1W3A, Cell Signaling), RIG-I (Alme-1, AdipoGen), IRF1 (D5E4, Cell Signaling), IRF3 (D83B9, Cell Signaling), phospho-IRF3 (Ser386) (EPR2346, Abcam), STAT1 (42H3, Cell Signaling), phospho-STAT1 (Tyr701) (58D6, Cell Signaling), RPS6 (5G10, Cell Signaling), CSTF2 (Bethyl Laboratories), Calnexin (C5C9, Cell Signaling), FLAG (M2, Sigma), Myc (71D10, Cell Siganling) or β-Actin-HRP (13E5, Cell Signaling). For detailed information about the source of the antibodies and dilutions used please refer to the Life Sciences Reporting Summary.

ZAP siRNA knockdown.

Specific DsiRNAs against ZAP-S and ZAP-L were custom-designed and obtained from Integrated DNA Technologies (IDT) (Supplementary Table 2). DsiRNA against *CSTF2* was obtained from IDT (hs.Ri.CSTF2.13.1). For knockdown experiments, DsiRNA was transfected at 10-20 nM final concentration using *Trans*IT-X2 (Mirus Bio) according to the manufacturer's instructions. Stimulations of cells were performed 24-36 h after DsiRNA transfection. Co-transfections of DsiRNA and poly U/UC RNA or expression plasmids were performed using

*Trans*IT-X2 (Mirus Bio) at a DsiRNA concentration of 10-20 nM. Cells were analyzed 24-42 h post transfection.

Generation of ZAP KO and *IRF3* KO cells.

ZAP targeting guide RNA (gRNA, 5′-GCAACTATTCGCAGTCCGAG-3′) and *IRF3* targeting guide RNA (gRNA, 5′-GTTGGAAGCACGGCCTACGGC-3′) was cloned downstream of the U6 promoter in the pRRLU6-empty-gRNA-MND-Cas9-t2A-Puro vector using In-Fusion enzyme mix (Clontech). Cells were transfected with ZAP- or *IRF3* gRNA-Cas9-expressing plasmids. Cas9-empty-expressing plasmids were transfected as control. $3x10^6$ Huh7 cells were seeded onto a 10 cm dish and 10 µg of plasmid was transfected using the $CaPO_4$ transfection kit (Invitrogen) according to the manufacturer's instructions. After 48 h cells were pre-selected by addition of 2 µg/ml puromycin to the media for 2 days. Pre-selected cells were sub-cloned and analyzed for absence of ZAP protein expression by immunoblot upon stimulation with IFNβ or transfection of poly U/UC RNA. *IFNAR1* KO cells were generated as previously described (*117*).

Generation of Flp-In HEK 293T cells expressing doxycycline-inducible ZAP isoforms.

ZAP isoform constructs were cloned into the Flp-In vector pcDNA5/FRT/TO. Flp-In T-REx 293 cells maintained in 5 µg/ml blasticidin were transfected at 70% confluency with ZAP isoform constructs and the vector containing the Flp recombinase pOG44 in a 1:10 molar ratio using *Trans*IT-X2 (Mirus Bio). After one day, cells were transferred to new dishes, and on the following day, hygromycin was added to the cells at a concentration of 100 µg/ml. Following

selection, cells were maintained in 5 µg/ml blasticidin and 100 µg/ml hygromycin. For ZAP expression, cells were induced with 500 ng/ml doxycycline.

Mass spectrometry.

IFNL3-WT and *IFNL3*-ΔARE 3′UTR were amplified from constructs containing wildtype (WT) sequences or disrupted ARE (ΔARE) in all three ATTTA motifs; pGL3 constructs described previously (*118*). The T7 promoter was incorporated using the following primers: T7-INFL3-F TAATACGACTCACTATAGGGACCCTTCCGCCAGTCATGC and IFNL3-R CAACAAGGATTTCAAAAAGTAGAAAAATAAACATTTTCCTGG. RNA probes were generated using the MAXIscript T7 *In Vitro* Transcription Kit (Ambion) as described by the manufacturer for 1 µg DNA template and were precipitated with ammonium acetate/ethanol. RNA probes were subsequently biotinylated using the RNA 3′End Biotinylation Kit (Pierce) according to manufacturer's instructions for 50 pmol RNA. $1.5x10^6$ Huh7 cells were lysed in 100 µl polysome lysis buffer. 2 µg biotinylated RNA probes were incubated with 400 µg protein lysate in 2X TENT buffer (20 mM Tris-HCl, pH 8.0; 2 mM EDTA; 500 mM NaCl; 1% Triton X-100), rocking at room temperature for 1 h. RNA probes were isolated using Dynabeads M-280 Streptavidin. RNA-protein complexes were washed 4 times with ice-cold PBS and eluted in SDS elution buffer (10 mM Tris-HCl, pH 8.0; 1 mM EDTA; 2% SDS), shaking at 1000 rpm for 30 min at 55 °C. Bound proteins were TCA-precipitated and dry protein pellets were frozen at -20 °C until ready for digestion.

Protein pellets from biotinylated RNA pull-downs (~15 µg) were resuspended in 40 µl of 100 mM ammonium bicarbonate + 5% acetonitrile + 8 M urea, subsequently reduced with 4 µl 50 mM DTT, and incubated for 30 min at 56 °C. Cooled samples were then alkylated with 4 µl

100 mM iodoacetamide (IAA) and incubated at room temperature for 30 min in the dark. Unreacted IAA was quenched with 4 µl 50 mM DTT and incubated at room temperature for 15 min in the dark. The protein mixture was diluted 1:5 with 25 mM ammonium bicarbonate + 5% acetonitrile to reduce the concentration of urea to <2 M. 26 µl of 100 mM $CaCl_2$ was added to the mixture before digestion with 7 µl of 0.2 µg/µl trypsin at 37 °C for 4 h. Digestion products were cooled to room temperature before peptide clean-up using C18 Spin Columns (Pierce) according to the manufacturer's instructions. Peptides were eluted in 80 µl of 70% acetonitrile, dried in a SpeedVac for 1.5 h and reconstituted in 10 µl of 5% acetonitrile + 0.1% formic acid. Peptides were loaded onto the ACQUITY UPLC system (Waters), trapped on Magic C18AQ 200Å 5u beads (MichromBioresources PM5/61200/00) and run through an analytical separation column with Magic C18AQ 100Å 5u beads (MichromBioresources PM5/61100/00). Analysis was performed on the LTQ Orbitrap XL (Thermo) mass spectrometer. Peptides were identified using Comet (Dragonfly) and assignments were established using PeptideProphet (ISB). Subsequent protein identification using ProteinProphet (ISB) required a minimum of 2 high confidence peptides (0.01 false discovery rate).

RNA-Immunoprecipitation.

FLAG-tagged ZAP-S and FLAG-tagged ZAP-L expression plasmids were generated by cloning of the ZAP CDS from pcDNA4 huZAP(S) and pcDNA4 huZAP(L) (obtained from Addgene) into the MCS of pEF N-FLAG (gift from Michael A. Davis, UW Immunology). A FLAG-empty vector (EV) was used as negative control for RNA-IP. $4x10^6$ Huh7 cells were seeded onto a 10 cm cell culture dish the day before transfection. The next day, 4 µg ZAP-S, ZAP-L, or EV expression plasmid were co-transfected with 2 µg poly U/UC RNA using

*Trans*IT-X2 (Mirus Bio) according to the manufacturer's instructions. 24 h after transfection cells were harvested and lysed in RNA-IP lysis buffer (100 mM KCl, 5 mM $MgCl_2$, 10 mM HEPES pH 7.4, 0.5% NP-40, 1 mM DTT, 1x HALT protease inhibitor, 100 U/ml RNasin, 2 mM ribinucleoside-vanadyl complex). Nuclei and debris were removed from cytosolic lysate by centrifugation at 8,000 x g at 4 °C for 10 min. 400 µg protein from cytosolic lysate was incubated with 5 µg anti-FLAG mouse IgG_1 (M2, Sigma) or mouse IgG_1 control over night at 4° C rotating. The next day, 0.75 mg Dynabeads Protein G (Invitrogen) were added and the lysate was incubated for 2 h at 4° C rotating. For RNA-IP of endogenous ZAP, cytosolic lysates were incubated with 10 µg of anti-ZAP antibody (GeneTex) and 1.2 mg Dynabeads Protein G (Invitrogen) were used. After washing, co-precipitated RNA was isolated from IgG_1-protein complexes by chloroform-isoamyl alcohol extraction, reverse transcribed into cDNA (QuantiTect RT kit, Qiagen) and analyzed for mRNA transcripts by qPCR. For UV-crosslinking, cells were irradiated in cold PBS on ice with 120 mJ/cm^2 before cell lysis, using a Stratalinker 1800 (Stratagene).

Confocal immunofluorescence microscopy.

Cells were seeded on type I collagen (Sigma) coated 12 mm coverslips (EMS) and rested overnight. Cells were transfected using *Trans*IT-X2 (Mirus Bio) with expression plasmids encoding respective ZAP isoforms and/or mCherry-tagged organelle markers: Rab5 (Addgene #49201)(*150*), Rab7A (Addgene #61804)(*151*), and Sec61β (Addgene #49155)(*151*) COX8 (Addgene #55102), PTS1 (Addgene #54520), and LAMP-1 (Addgene #55073)(*152*). mCherry-tagged Rab5, Rab7A, and Sec61β were gifts from Gia Voeltz and COX8, PTS1, and LAMP-1 were gifts from Michael Davidson. At 24 h post-transfection, cells were fixed in 4% PFA/PBS

for 10 min at room temperature and then permeabilized with PBS containing 0.1% Triton-X100 for 10 min at room temperature. Permeabilized samples were then blocked for 1 h at room temperature in 3% BSA/PBS and then stained with the following primary antibodies in PBS containing 1% BSA and 0.3% Triton-X100 for 1 h at room temperature: mouse anti-FLAG (Sigma), rabbit anti-Myc (Cell Signaling), rabbit anti-ZAP (GeneTex), mouse J2 anti-dsRNA (Scicons). For immunofluorescence staining of the plasma membrane and stress granules primary anti-E-cadherin (Thermo) and anti-G3BP1 (Abcam) antibodies were used. Cells were washed three times with PBS prior to staining with the following secondary antibodies in PBS containing 1% BSA and 0.3% Triton-X100 for 1 h in the dark at room temperature: goat anti-mouse IgG Alexa Fluor 488, goat anti-rabbit IgG Alexa Fluor 594, and goat anti-rabbit IgG Alexa Fluor 488 (all Thermo Fisher). Samples were washed with PBS three times and then mounted with ProLong Diamond antifade mounting media (Thermo Fisher) with DAPI. Samples were cured in the dark at room temperature prior to imaging. All samples were imaged on a Nikon Eclipse Ti laser scanning confocal microscope using a 60x oil-immersion lens. Images were processed and analyzed using the NIS elements software and Fiji. Quantification of co-localization was performed for 10 cells each, using the Fiji Coloc 2 plugin. Overlays of co-localized pixels were calculated and generated using the Fiji Colocalization Threshold plugin, using Costes auto threshold algorithm to determine true co-localization. For detailed information about the source of the antibodies and dilutions used please refer to the Life Sciences Reporting Summary.

Super-resolution structured illumination microscopy.

All samples were imaged on a DeltaVision OMX SR imaging system (GE Healthcare) using a 60x oil-immersion objective. SIM reconstruction and image alignment was achieved using SoftWoRx. ZAP KO Huh7 cells were seeded on #1.5 high precision glass coverslips (Bioscience Tools) and coated with collagen as described previously. Cells were transfected with Myc-tagged ZAP-S and FLAG-tagged ZAP-L and were stained 24 h post-transfection as previously described. Cells were mounted using ProLong Glass antifade mounting media and cured for 48 h prior to imaging.

Cell fractionations.

For differential subcellular fractionation Huh7 ZAP KO cells were seeded on 10 cm dishes and allowed to settle overnight. Cells were then transfected with expression plasmids encoding either ZAP-S, ZAP-L, ZAP-S+CVIS, or ZAP-L SVIS. At 24 h post transfection, cells were incubated on ice in hypotonic lysis buffer (20 mM HEPES pH 7.4, 10 mM KCl, 2 mM $MgCl_2$, 1 mM EDTA, 1 mM EGTA, 1 mM DTT, 1x HALT protease and phosphatase inhibitor, 3 mM imidazole) for 30 min. Cells were passed through a 27-gauge needle 10 times prior to collection of the soluble cytosolic fraction by spinning down the lysate for 1 h at 100,000 x g in an Optima TL Ultracentrifuge. Whole cell lysates and soluble cytoplasmic fractions were blotted as described previously using antibodies against ZAP (GeneTex), COX IV (Cell Signaling), and α-tubulin (Cell Signaling).

For polyribosome fractionation $1x10^7$ Huh7 WT cells were grown on 15 cm dishes and stimulated with 500 IU/ml human recombinant IFN-β for 24 h. Cells were incubated with 5 µg/ml harringtonine (LKT Labs) in PBS for 10 min or with 100 µg/ml cycloheximide (Sigma) in PBS for 5 min at 37 °C with 5% CO_2. Cells were then washed twice in ice-cold PBS and

harvested in 500 µl polysome lysis buffer (50 mM Tris-HCl pH 7.5, 100 mM KCl, 12 mM $MgCl_2$, 1% NP-40, 1 mM DTT, 1x HALT protease inhibitor, 100 µg/ml cycloheximide). The lysate was cleared of nuclei and debris by centrifugation at 8,000 x g for 10 min at 4 °C. Supernatants were layered on a 10-50% sucrose gradient and spun at 230,000 x g for 2.5 h at 4 °C. Gradients were then fractionated while continuously monitoring absorbance at 254 nm. 15 µl of each fraction was loaded for Western blot.

Membrane flotation assays were performed as previously described (*153*), with the following modifications. Briefly, Huh7 WT cells were grown to ~80% confluency in T150 flasks. Cells were harvested and for each condition, 30 million cells were resuspended in PBS containing 0.25 M sucrose and a protease/phosphatase inhibitor cocktail and placed on ice for 30 min. Cells were then lysed on ice with a tight-fitting dounce homogenizer. After 200 passages, lysis efficiency (90%) was assayed by trypan blue staining. Post nuclear lysate was generated by collecting supernatants after centrifugation of the crude lysate at 2,500 x g for 10 min at 4 °C. Protein concentration was determined by BCA and 500 µg of protein was mixed with PBS containing 0.25 M sucrose to a final volume of 2 ml. Samples were then mixed with 2 ml of PBS containing 0.25 M sucrose and 60% (w/v) Histodenz (Sigma) non-ionic density gradient medium. This mixture was then carefully added to a 14 ml ultracentrifuge tube (Beckman) and then 4 ml of PBS containing 0.25 M sucrose and 20% (w/v) Histodenz was carefully overlayed. A final 4 ml of PBS containing 0.25 M sucrose and 10% (w/v) Histodenz was carefully overlayed. Samples were spun down overnight (~16 h) at 4 °C and 209,000 x g in an SW41Ti rotor in an L8-70m ultracentrifuge (Beckman). After spin, 500 µl fractions were taken from the top by careful removal and stored at -80 °C until ready for use.

Ribosome profiling.

$1x10^7$ Huh7 ZAP KO cells were grown on 15 cm dishes and transfected with plasmids expressing ZAP-S, ZAP-L or empty vector (EV) control. 24 h after plasmid transfection, cells were stimulated with 250 ng/ml poly U/UC RNA for 18 h. Cells were then incubated with 100 µg/ml cycloheximide (Sigma) in PBS for 5 min at 37 °C with 5% CO_2. Cells were washed twice in ice-cold PBS and harvested in 500 µl polysome lysis buffer (50 mM Tris-HCl pH 7.5, 100 mM KCl, 12 mM $MgCl_2$, 1% NP-40, 1 mM DTT, 1x HALT protease inhibitor, 100 µg/ml cycloheximide). The lysate was cleared of nuclei and debris by centrifugation at 8,000 x g for 10 min at 4 °C. Supernatants were layered on a 10-50% sucrose gradient and spun at 230,000 x g for 2.5 h at 4 °C. Gradients were then fractionated while continuously monitoring absorbance at 254 nm. Total RNA was isolated from the fractions using TRIzol and the Direct-zol 96 RNA kit (Zymo Research) according to the manufacturer's instructions. cDNA was synthesized from 1 µg total RNA using the QuantiTect RT kit (Qiagen) according to manufacturer's instructions. qPCR was carried out using the ViiA7 qPCR system with *Taq*Man reagents using *Taq*Man primers/probes (Life Technologies) for *IFNB* and *HPRT*.

Virus infections.

Sindbis virus (SINV) was generated by electroporation of *in vitro* transcribed RNA from plasmid SINV TE/5′2J-GFP (from Dr. Charles Rice, Rockefeller University) into BHK cells as previously described (*121*). For antiviral protection assays, SINV infections were performed in 24 well plates using MOI=0.1 and viral supernatants were harvested 16 h (for Huh7 cells) or 24 h (for Flp-In 293 cells) after infection and titrated on BHK cells. For immunofluorescence staining of SINV dsRNA intermediates, Huh7 cells were grown on collagen-coated glass coverslips and

were infected with SINV Toto or AR86 at indicated MOIs in DMEM +10% FBS. At indicated time points, cells were washed once in PBS, fixed for 10 min in 4% PFA/PBS for 10 min at room temperature, and then incubated in 0.1% Triton X-100 for 10 min at room temperature. Coverslips were subsequently washed 3x in PBS before staining. Vesicular stomatitis virus (VSV) was a generous gift of J. Rose (*154*) and was propagated in BHK cells. VSV infections were performed in 24 well plates using a MOI=0.04 and viral supernatants were harvested 12 h after infection and titrated on BHK cells. For infection of Flp-In HEK 293T cells, doxycycline was added to 500 ng/ml 16 h before viral infection. For knockdown of ZAP isoforms in Huh7 cells prior to infection, siRNAs were transfected 16 h before infection. For Semliki Forest virus replicon assays, the vector pSMART was used (*138*), which expresses the non-structural proteins of Semliki Forest virus followed by a sub-genomic promoter driven beta-galactosidase protein. Expression of the beta-galactosidase gene is dependent on viral genome replication and expression of virally-transcribed genes. HEK 293T cells in 24 well plates were transfected with 200 ng pSMART and the indicated amount of pcDNA5/FRT/TO expressing ZAP constructs. After 24 h, cells were freeze/thawed three times and 4-methylumbelliferyl-β-D-galactopyranoside (4-MUG) was added to 200 µg/ml to measure beta-galactosidase activity. Fluorescence (excitation/emission wavelength of 365/460 nm) was monitored every 20 sec and the rate of fluorescence increase was averaged for 5 min.

Statistics.

Statistical analyses for quantitative assays were performed with Prism 8 (GraphPad Software) using Student's t-test (to compare two conditions), one-way ANOVA with multiple comparisons (to compare more than two conditions), or two-way ANOVA with multiple

comparisons (to compare between two independent variables) was performed to analyze statistical significance between treatment groups. The confidence interval for all statistical test was 95%. More information on analyses performed and exact P-values can be found in the legend of each Figure.

Data availability. The data that support the findings of this study are available from the corresponding author upon reasonable request.

2.5 Acknowledgements

This project was funded by National Institutes of Health grants AI108765 and AI135437 (R.S.), AI119017 (M.D.D.), AI104002, AI118916, AI127463 (M.G.), the Pew Biomedical Scholars program (M.D.D.), a Research Fellowship from the German Research Foundation (DFG) to J.S. (SCHW 1881/1-1), T32 training grants (AI106677 and GM007270) to F.W.S., and T32 training grant (GM007240) to A.P.R. This work was supported in part by the UW Proteomics Resource (UWPR95794). We would like to acknowledge P. von Haller and J. Eng (UW Proteomics Resource) for expert technical assistance with mass spectrometry. We are thankful for the support of W. P. Chang (UW Biology Imaging Facility) for help with super-resolution microscopy. We thank M. A. Davis (UW Immunology) for help with confocal laser scanning microscopy, D. B. Stetson and K. Burleigh (UW Immunology) for providing the *IRF3* CRISPR construct, S. N. Sarkar (University of Pittsburgh) for providing *STAT1* KO PH5CH8 cells, and members of the Savan, Daugherty, and Gale labs for helpful discussions.

Author contributions

J.S., F.W.S., M.G., M.D.D., and R.S. designed the study; R.S. directed the study. J.S., F.W.S., A.P.R., K.R.T., L.D.H., S.O., A.F., A.M.K., J.A.R., L.S. and J.L.H. performed experiments and analyzed the data. J.S., M.D.D., and R.S. wrote the manuscript.

2.6 Figures

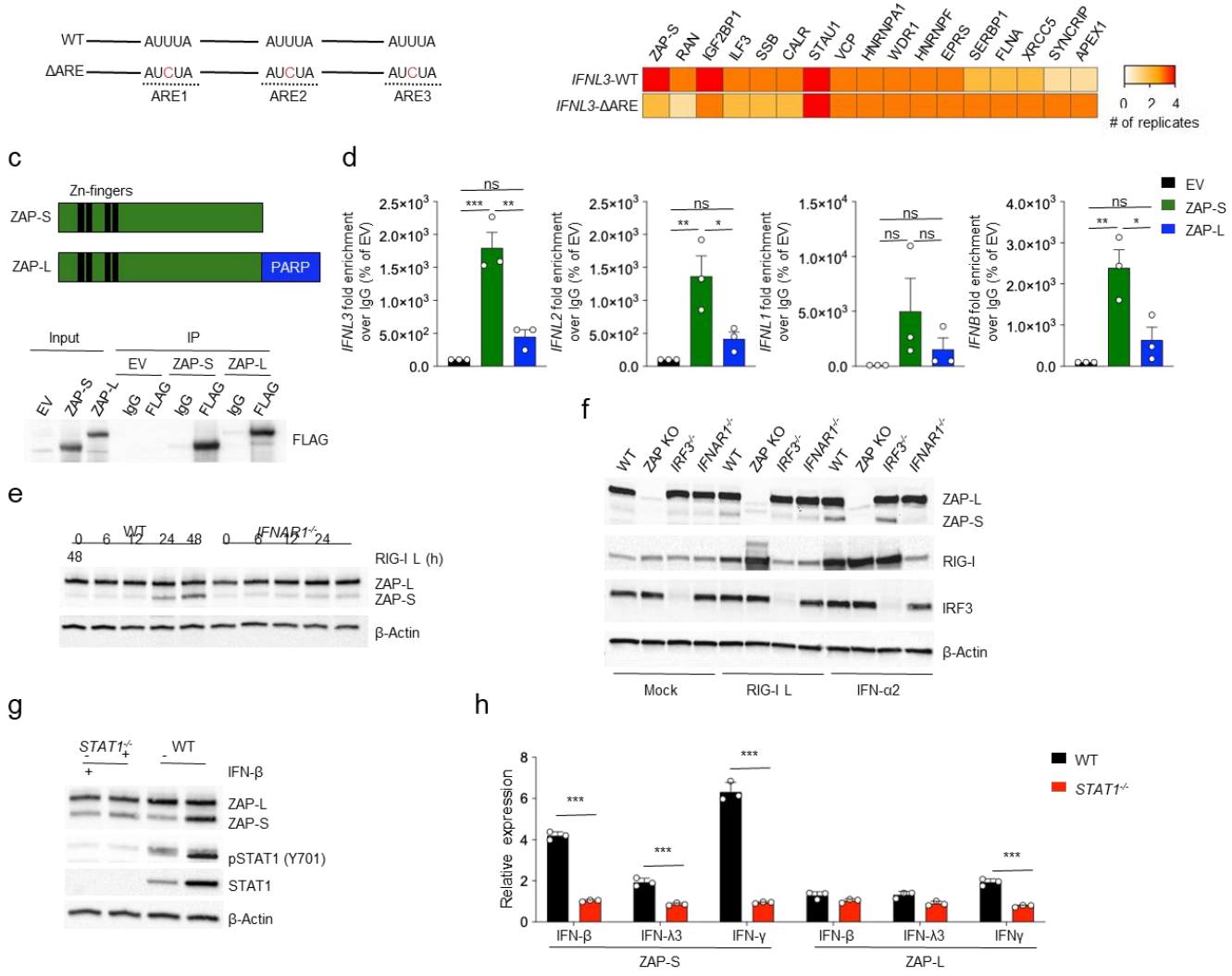

Figure 2.1. ZAP-S interacts with the 3'UTR of *IFN* mRNAs.

(a) Schematic of *IFNL1*, *IFNL2* and *IFNL3* 3′UTR sequences showing AREs 1-3 and mutations (ATTTA > ATCTA) introduced to disrupt the motifs (ΔARE). **(b)** Mass spectrometry of

biotinylated *IFNL3* 3′UTR and interacting proteins of HepG2 cell lysate. **(c)** Domain structures of ZAP-S and ZAP-L protein isoforms. Western blot of immunoprecipitated FLAG-tagged ZAP-S, ZAP-L and empty vector (EV) control in Huh7 ZAP KO cells 24 h after stimulation with poly U/UC RNA. **(d)** qPCR analysis of immunoprecipitated FLAG-tagged ZAP-S, ZAP-L and empty vector (EV) control in Huh7 ZAP KO cells after stimulation with poly U/UC RNA for 24 h. Data from three independent experiments is shown combined as fold enrichment over IgG control (% of EV). Bars show mean ± SEM. **(e)** Western blot of ZAP isoform expression in Huh7 WT and IFNAR1-/- cells after stimulation with 0.3 µg/ml poly U/UC RNA (RIG-I L). **(f)** Western blot of ZAP isoform expression in Huh7 wild-type, ZAP KO, IFNAR1-/- and IRF3-/- cells after stimulation with 0.2 µg/ml poly U/UC RNA (RIG-I L) or treatment with 100 ng/ml recombinant human IFN-α2 for 48 h. **(g)** Western blot of ZAP isoform expression in PH5CH8 wild-type and STAT1-/- cells after treatment with 200 IU/ml IFN-β for 24 h. **(h)** qPCR of ZAP isoform mRNA expression in PH8CH8 wild-type and STAT1-/- cells after treatment with 25 IU/ml IFN-β, 100 ng/ml IFN-λ3 or 5 ng/ml IFN-γ for 9 h. Data shown is representative of three independent experiments with replicates (n=3) and similar results. Bars show mean ± SD. (c, e-g) Representative Western blots of three individual experiments with similar results are shown. Data were analyzed using (d) one-way ANOVA with Tukey's post-test or (h) two-way ANOVA with Sidak's post-test. *$P < 0.05$; **$P < 0.01$; ***$P < 0.001$; ns, not significant.

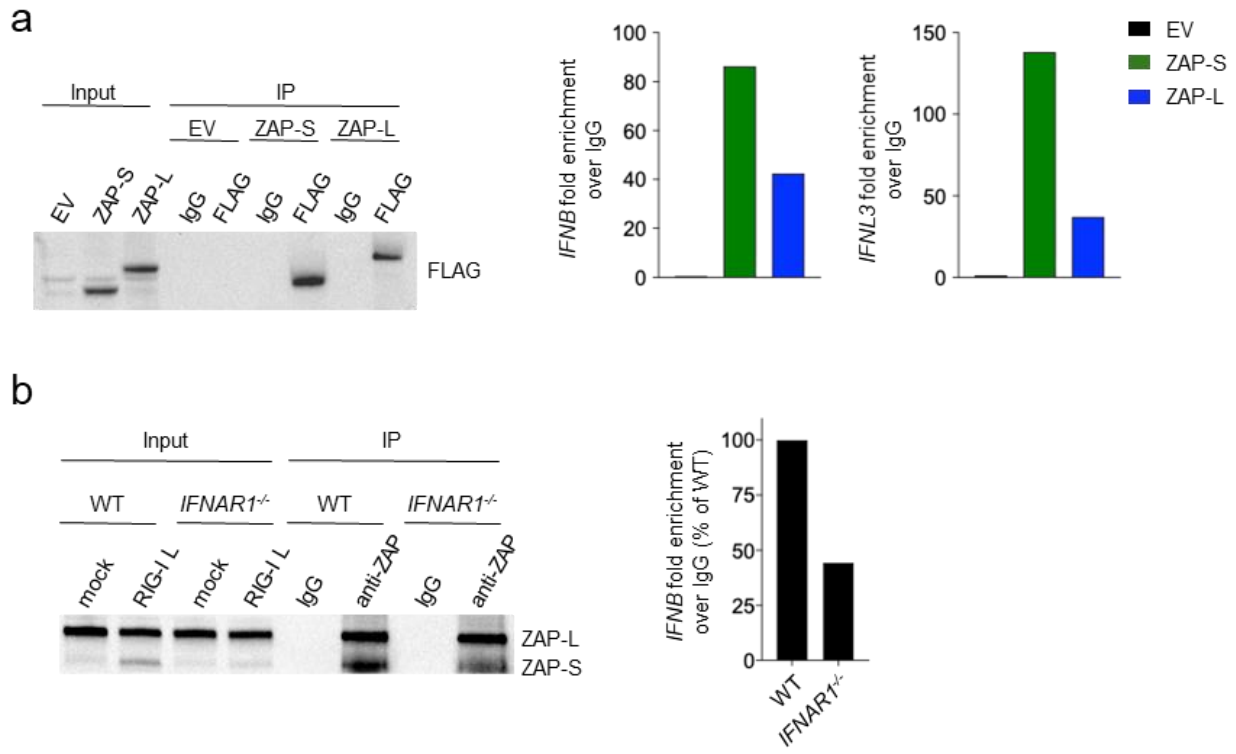

Supplementary Figure 2.1 (related to 2.1).

(a) ZAP RNA-IP performed in Huh7 ZAP KO cells under UV crosslinking conditions after expression of FLAG-tagged ZAP-S, FLAG-tagged ZAP-L and FLAG-empty vector (EV) control, and stimulation with 0.2 µg/ml RIG-I ligand for 24 h. **(b)** RNA-IP of endogenous ZAP performed in Huh7 WT and IFNAR1 KO cells after stimulation with 0.5 µg/ml RIG-I ligand for 24 h. Representative experiments of (a) two and (b) three independently performed experiments with similar results are shown.

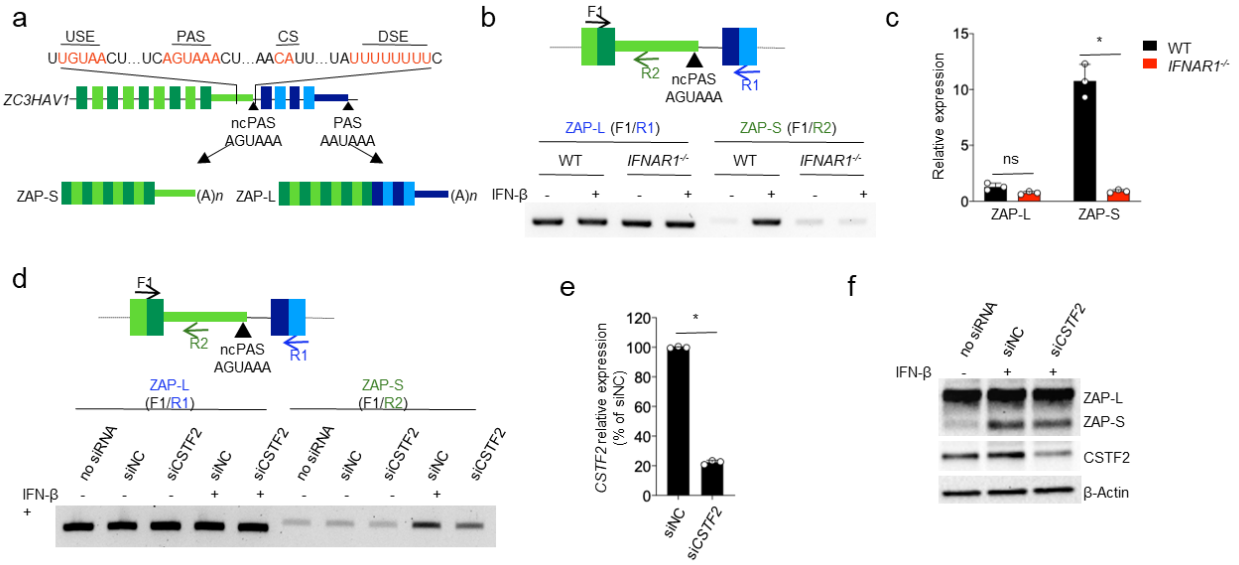

Figure 2.2. CSTF2-mediated alternative polyadenylation generates ZAP-S.

a) Schematic of intron/exon structure of the ZC3HAV1 gene. The intron between exons 9 and 10 harbors a non-canonical weak polyadenylation signal (ncPAS, AGUAAA) that is flanked by an upstream element (USE) and a downstream element (DSE) required for recruitment of the 3′ processing machinery. **(b)** PCR on cDNA of Huh7 wild-type and IFNAR1-/- cells stimulated with or without 250 IU/ml IFN-β for 8 h. **(c)** qPCR with ZAP isoform-specific probes on cDNA of Huh7 wild-type and IFNAR1-/- cells stimulated with or without 250 IU/ml IFN-β for 8 h. **(d)** PCR on cDNA of Huh7 WT cells transfected with non-targeting control (NC) or CSTF2 siRNA and stimulated for 24 h with or without 250 IU/ml IFN-β 24 h after siRNA transfection. **(e)** CSTF2 mRNA expression in Huh7 cells upon knockdown of CSTF2 and stimulation with 250 IU/ml IFN-β for 24 h. **(f)** Western blot of ZAP protein expression in Huh7 cells upon knockdown of CSTF2 and stimulation with 250 IU/ml IFN-β for 24 h. (b-f) Data shown are representative of three independent experiments with replicates (n=3) and similar results. Bars

show mean ± SD. Data were analyzed using (c) two-way ANOVA with Sidak's post-test or (e) unpaired two-tailed Student's t-test. *P < 0.001; ns, not significant.

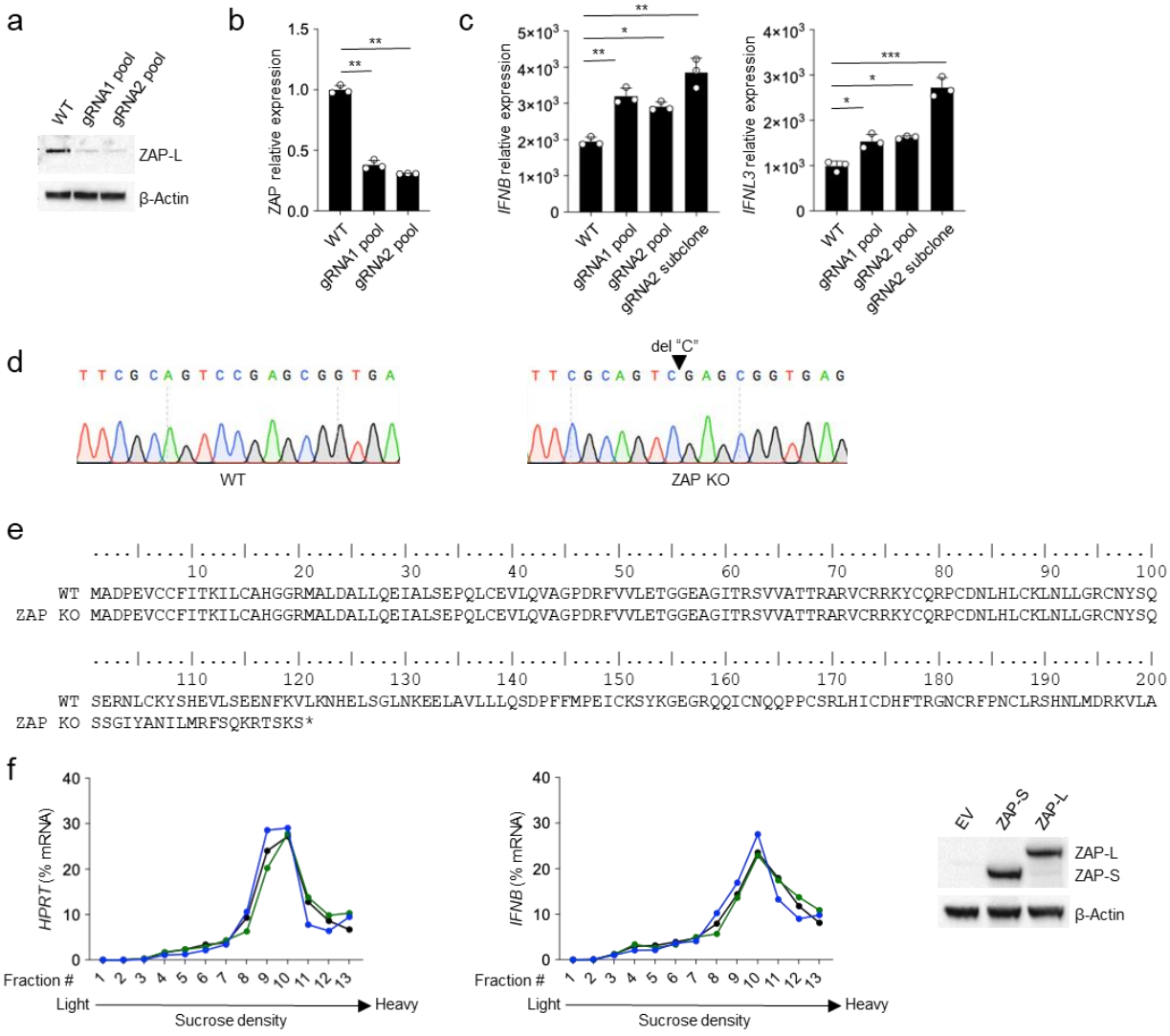

Supplementary Figure 2.2 (related to 2.2).

(a) Western blot of Huh7 ZAP KO cell pools generated by CRISPR-Cas9 technology using two different guide RNAs. **(b)** *ZAP* mRNA expression in ZAP KO cell pools. **(c)** *IFNB* and *IFNL3* mRNA expression in ZAP KO cell pools compared to WT cells and a single-cell sub-clone after stimulation with RIG-I ligand for 24 h. (a-c) Representative experiments with replicates (n = 3) of two independently performed experiments with similar results are shown. Bars show mean ±

SD. **(d)** Sequencing chromatogram of the CRISPR target region in exon 1 of the human ZAP (ZC3HAV1) gene. Four bacterial clones were sequenced showing the same del C deletion. **(e)** Alignment of WT and CRISPR targeted ZAP polypeptide sequence (amino acid residue 1-200). The ΔC base pair deletion results in a premature stop codon at amino acid residue 121 (exon 2). **(f)** Polysome profiling of *HPRT* and *IFNB* mRNA after overexpression of ZAP-S (green), ZAPL (blue), or empty vector (EV, black) control in Huh7 ZAP KO cells and stimulation of the cells with 0.25 μg/ml RIG-I ligand for 18 h. A representative of two independent experiments with similar results is shown. Data were analyzed using one-way ANOVA with Tukey's post-test. *P < 0.01; **P < 0.001; ns, not significant.

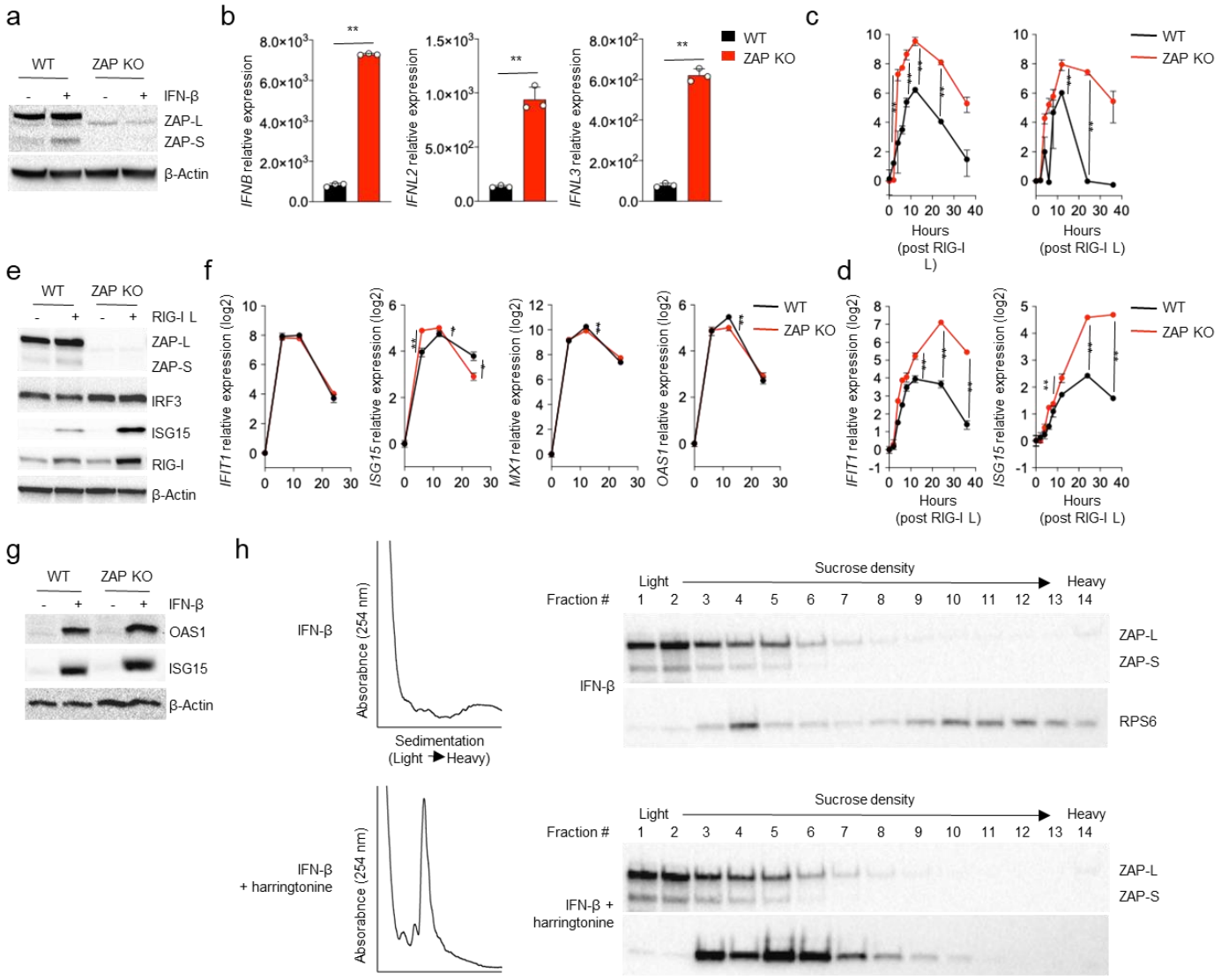

Figure 2.3. ZAP-deficient cells have a higher and more prolonged IFN response.

(a) Western blot of Huh7 wild-type and ZAP KO cells treated with IFN-β for 24 h. **(b)** Expression of *IFNB*, *IFNL2* and *IFNL3* mRNA in Huh7 wild-type and ZAP KO cells 18 h after stimulation with poly U/UC RNA. Bars show mean ± SD. (c, d) Time course of **(c)** *IFNB* and *IFNL3* mRNA or **(d)** *IFIT1* and *ISG15* mRNA expression upon pulsing of Huh7 wildtype and ZAP KO cells with 1 µg/ml poly U/UC RNA (RIG-I L) for 2 h. Symbols show mean ± SD. **(e)** Western blot of ZAP, IRF3, ISG15 and RIG-I protein expression in Huh7 wild-type and ZAP KO cells 36 h after

stimulation with 0.2 µg/ml poly U/UC RNA (RIG-I L). **(f)** Expression of *IFIT1*, *ISG15*, *MX1* and *OAS1* mRNA upon treatment of Huh7 wild-type and ZAP KO cells with 25 IU/ml IFN-±. Symbols show mean ± SD. **(g)** Western blot of ISG15 and OAS1 protein expression in Huh7 wild-type and ZAP KO cells after stimulation with 25 IU/ml IFN-β for 24 h. **(h)** Polysome fractionation of Huh7 wild-type cells treated with 500 IU/ml IFN-β for 24 h, and with or without 5 µg/ml harringtonine. In (a-h) data shown is representative of three independent experiments with replicates (n=3) for (b-d, f) and similar results. Data were analyzed using (b) unpaired two-tailed Student's t-test or (c, d, f) two-way ANOVA with Sidak's post-test. *P < 0.01; **P < 0.001.

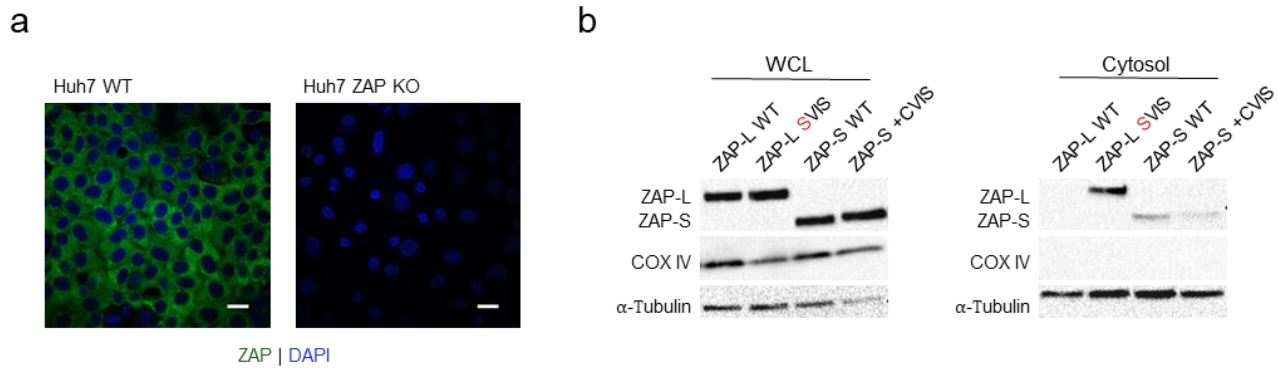

Supplementary Figure 2.3 (related to 2.3).

(a) Immunofluorescence staining of endogenous ZAP in Huh7 WT and ZAP KO cells. The scale bar represents 20 µm. **(b)** Subcellular fractionation of ZAP WT and CaaX mutant isoforms after expression in Huh7 ZAP KO cells. For (a, b) representative micrographs and Western blots of three independent experiments with similar results are shown.

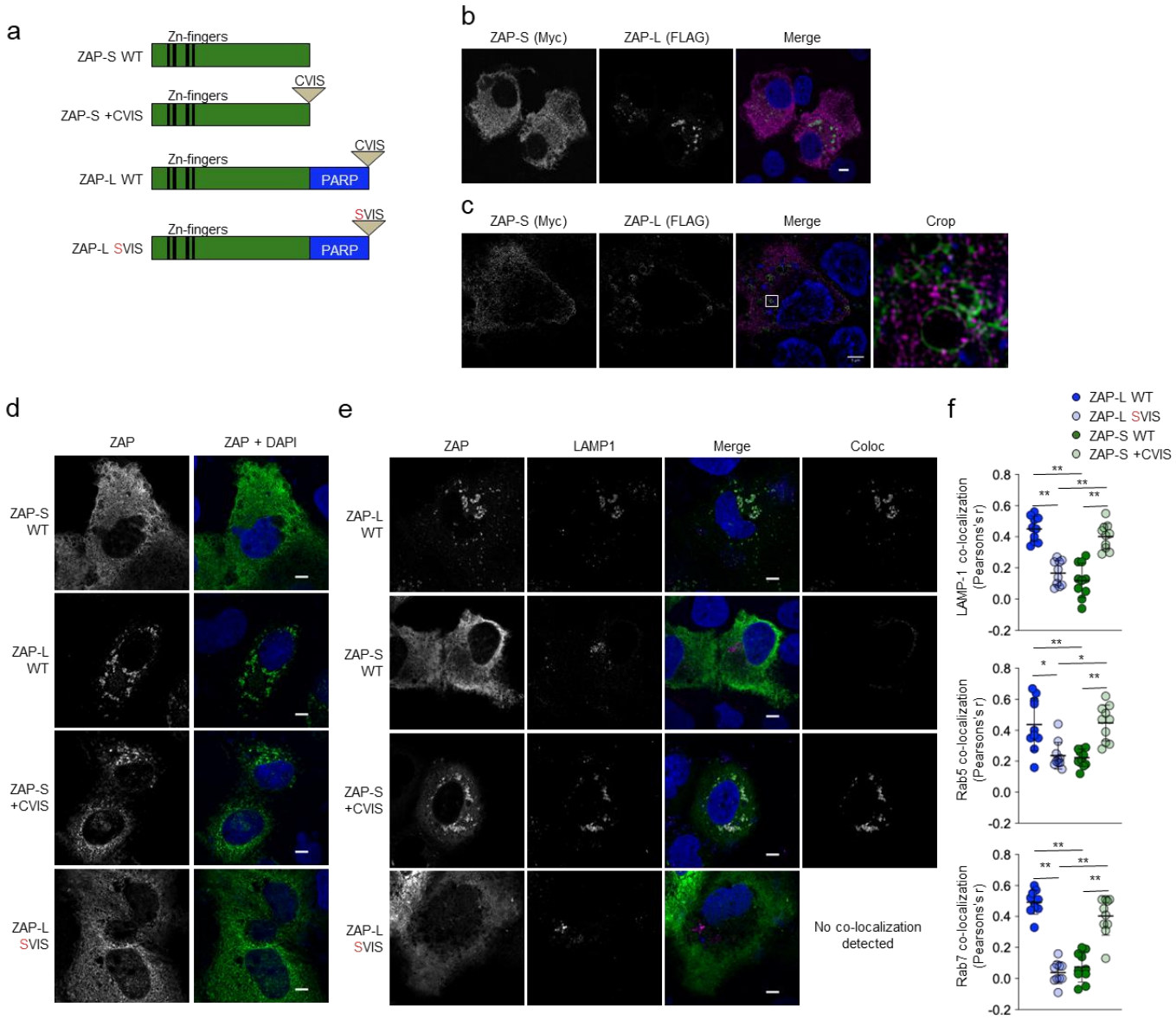

Figure 2.4. ZAP-L and ZAP-S localize to different subcellular compartments.

(a) Schematic of WT ZAP-S and WT ZAP-L and their CaaX motif (CVIS) mutants generated by site-directed mutagenesis. **(b)** Confocal immunofluorescence microscopy of Myc-tagged ZAP-S and FLAG-tagged ZAP-L upon co-expression in Huh7 ZAP KO cells. The scale bar represents 5 µm. **(c)** Super-resolution structured illumination microscopy (SIM) of Myc-tagged ZAP-S and FLAG-tagged ZAP-L co-expressed in Huh7 ZAP KO cells. **(d)** Confocal immunofluorescence microscopy of tagless WT ZAP-S, WT ZAP-L, or their respective CaaX motif mutants upon

expression in Huh7 ZAP KO cells. The scale bar represents 5 µm. **(e)** Confocal immunofluorescence microscopy of ZAP and LAMP1 upon co-expression of mCherry-LAMP1 and tagless WT ZAP-S and WT ZAP-L, or their CaaX motif mutants. The scale bar represents 5 µm. For (b-e) representative micrographs of three independently performed experiments are depicted. **(f)** Quantification of co-localization of ZAP with LAMP1-, Rab5-, and Rab7-positive pixels. The correlation coefficients (Pearson's r) of cells (n=10) from two independent experiments are shown and were calculated using the Fiji Coloc 2 plugin and one-way ANOVA with Tukey's post-test. Error bars show mean ± SD. *P < 0.01; **P < 0.001.

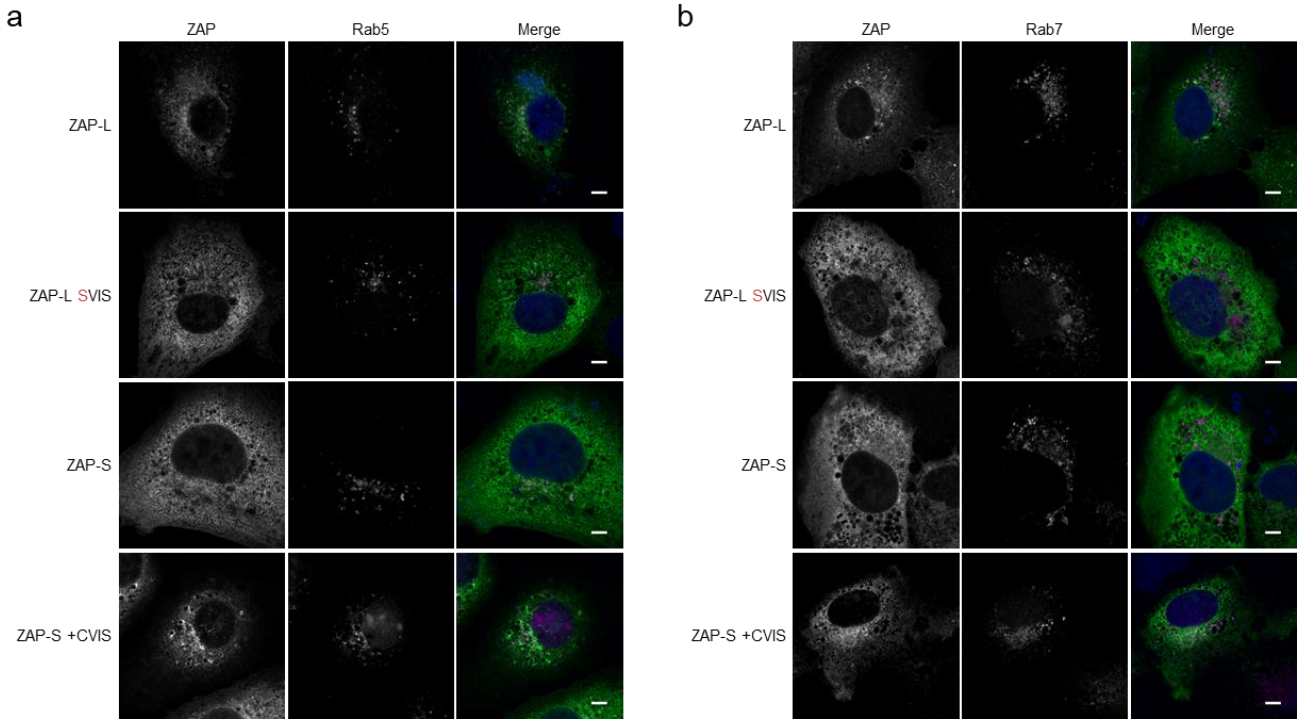

Supplementary Figure 2.4 (related to 2.4).

(a, b) Confocal immunofluorescence microscopy of ZAP and (a) Rab5 or (b) Rab7 after co-expression of mCherry-Rab5 or mCherry-Rab7 and tag-less ZAP-S, ZAP-L, or their CaaX mutants in Huh7 ZAP KO cells. The scale bar represents 5 µm. Representative micrographs of three independent experiments with similar results are shown.

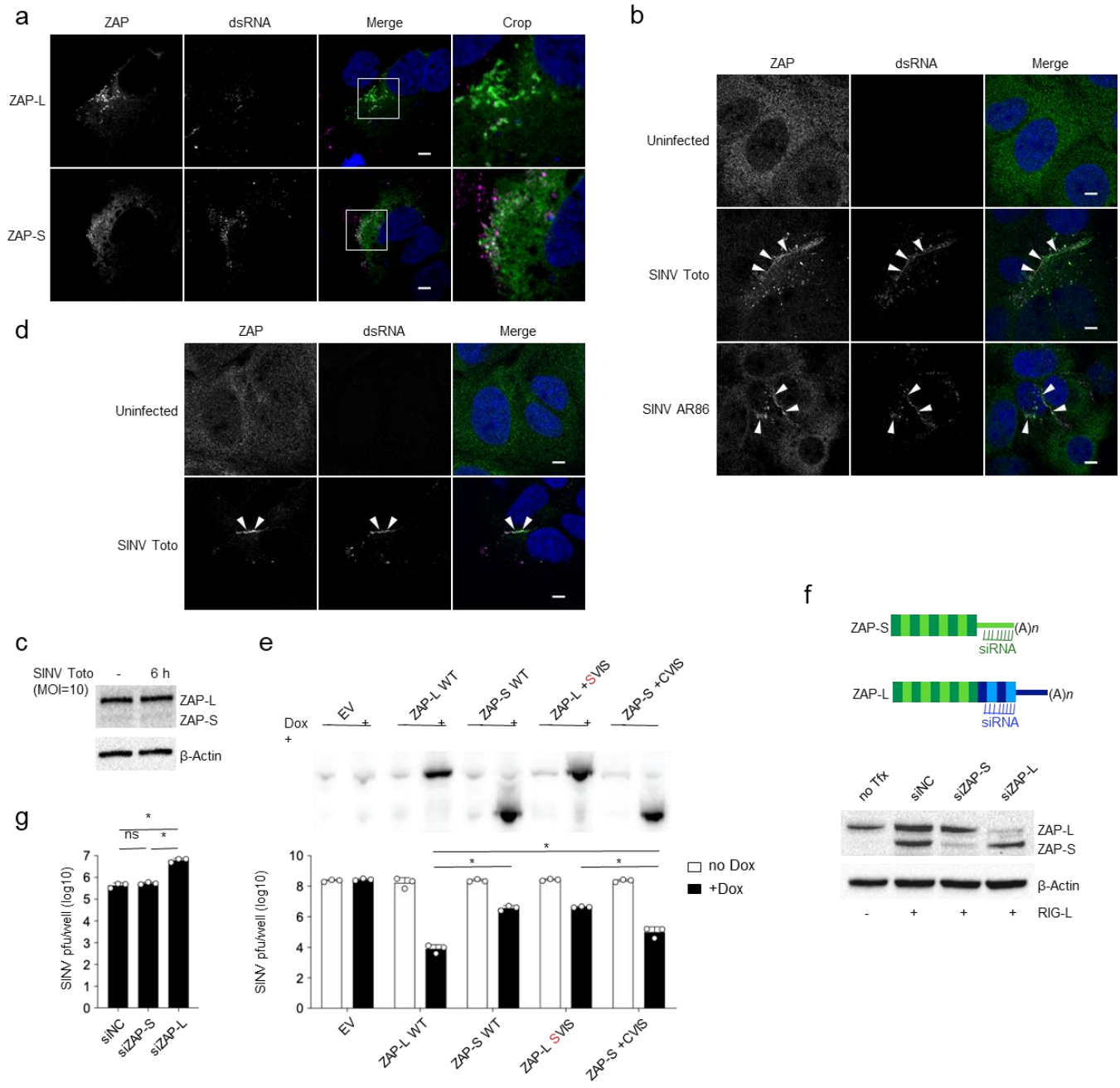

Figure 2.5. ZAP-L targets alphavirus RNA at viral replication sites.

(a) Confocal immunofluorescence microscopy of ZAP and SINV dsRNA in Huh7 ZAP KO cells expressing WT ZAP-L or WT ZAP-S 6 hpi with SINV Toto (MOI=10). The scale bar represents 5 µm. **(b)** Confocal immunofluorescence microscopy of endogenous ZAP and SINV (strains Toto and AR86) dsRNA 6 hpi of Huh7 wild-type cells (MOI=10). (c) Western blot of endogenous ZAP

isoform expression in Huh7 wild-type cells 6 hpi with SINV Toto (MOI=10). **(d)** Confocal immunofluorescence microscopy of ZAP and viral dsRNA in Huh7 IRF3-/- cells 6 hpi with SINV Toto (MOI=10). The scale bar represents 5 µm. **(e)** Viral titers from doxycycline-inducible HEK 293T cells expressing WT ZAP-S, WT ZAP-L or their respective CaaX motif mutants 24 hpi with SINV (MOI=0.1). Bars show mean ± SD. Data is representative of three independently performed experiments with replicates (n=3) and similar results. **(f)** Schematic of ZAP isoform-specific siRNA design and Western blot of ZAP isoform expression showing specificity of siRNAs. **(g)** Viral titers after siRNA-mediated knockdown of endogenous ZAP-S or ZAP-L in Huh7 wild-type cells 16 hpi with SINV (MOI=0.1). Bars show mean ± SD. Data is representative of three independently performed experiments with replicates (n=3) and similar results. For (a-d, f) representative micrographs and Western blots of three independently performed experiments with similar results are depicted. Data were analyzed using (e) two-way ANOVA with Sidak's post-test or (g) one-way ANOVA with Tukey's post-test. *$P < 0.001$; ns, not significant.

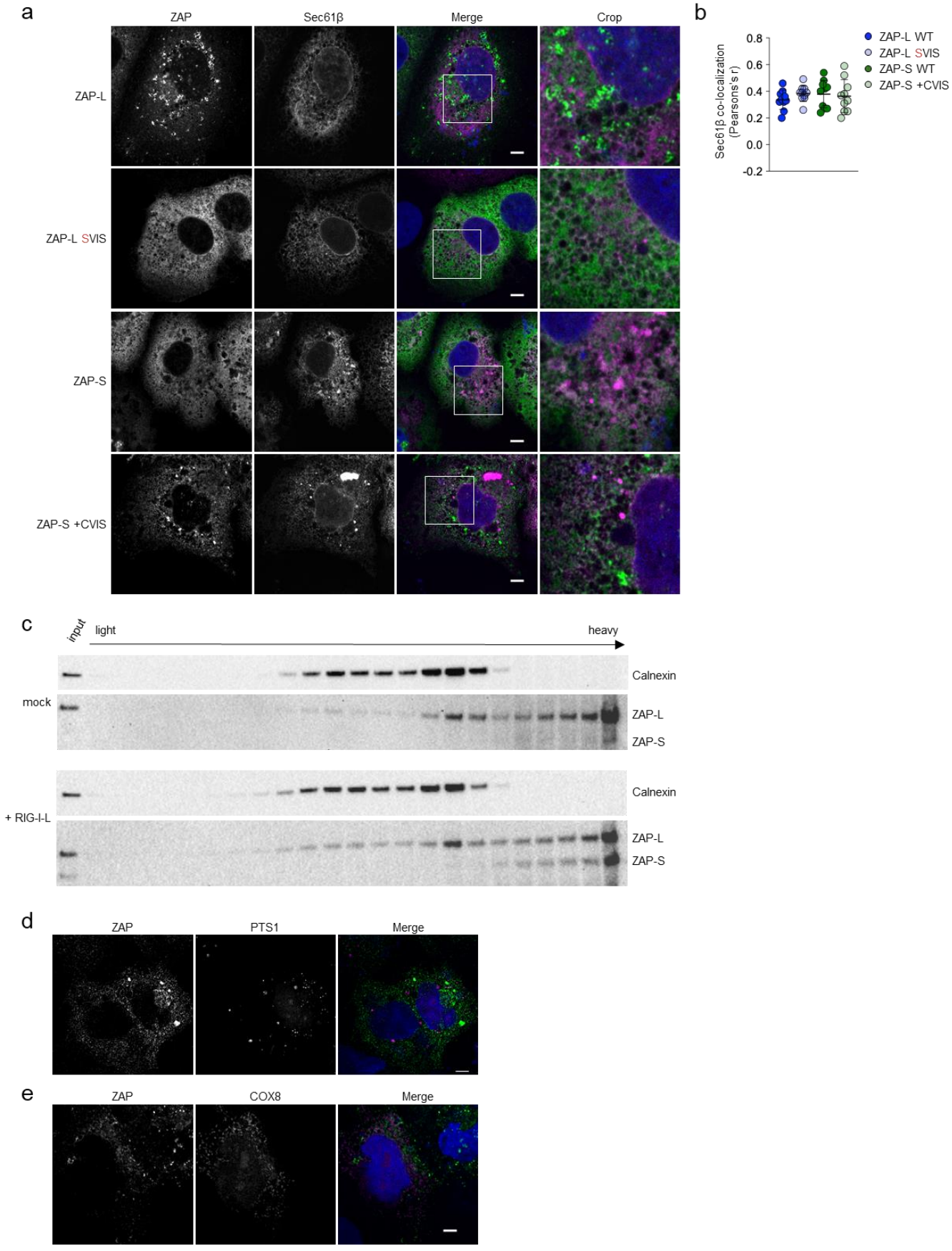
a
ZAP
Sec61β
Merge
Crop
ZAP-L
ZAP-L SVIS
ZAP-S
ZAP-S +CVIS
b
Sec61β co-localization (Pearsons's r)
0.8
0.6
0.4
0.2
0.0
-0.2
ZAP-L WT
ZAP-L SVIS
ZAP-S WT
ZAP-S +CVIS
c
input
light
heavy
mock
Calnexin
ZAP-L
ZAP-S
+ RIG-I-L
Calnexin
ZAP-L
ZAP-S
d
ZAP
PTS1
Merge
e
ZAP
COX8
Merge

Supplementary Figure 2.5 (related to 2.5).

(a) Confocal immunofluorescence microscopy of ZAP and the endoplasmic reticulum marker Sec61β. Representative micrographs of three independent experiments with similar results are shown. **(b)** Quantification of co-localization of ZAP-positive and Sec61β-positive pixels. The correlation coefficients (Pearson's r) of 10 cells were analyzed using the Fiji Coloc 2 plugin. Error bars show mean ± SD. **(c)** Membrane flotation assay and sedimentation of ZAP-L, ZAP-S, and the endoplasmic reticulum marker calnexin in Huh7 WT cells treated with or without 0.25 μg/ml RIG-I ligand for 24 h. A representative Western blot of two independently performed experiments with similar results is shown. (d, e) Confocal immunofluorescence microscopy of ZAP and **(d)** the peroxisomal marker PTS1 and **(e)** the mitochondrial marker COX8 after co-expression of mCherry-tagged PTS1 and COX8 together with tag-less ZAP-L. The scale bar represents 5 μm. (d,e) Representative micrographs of three independent experiments with similar results are shown.

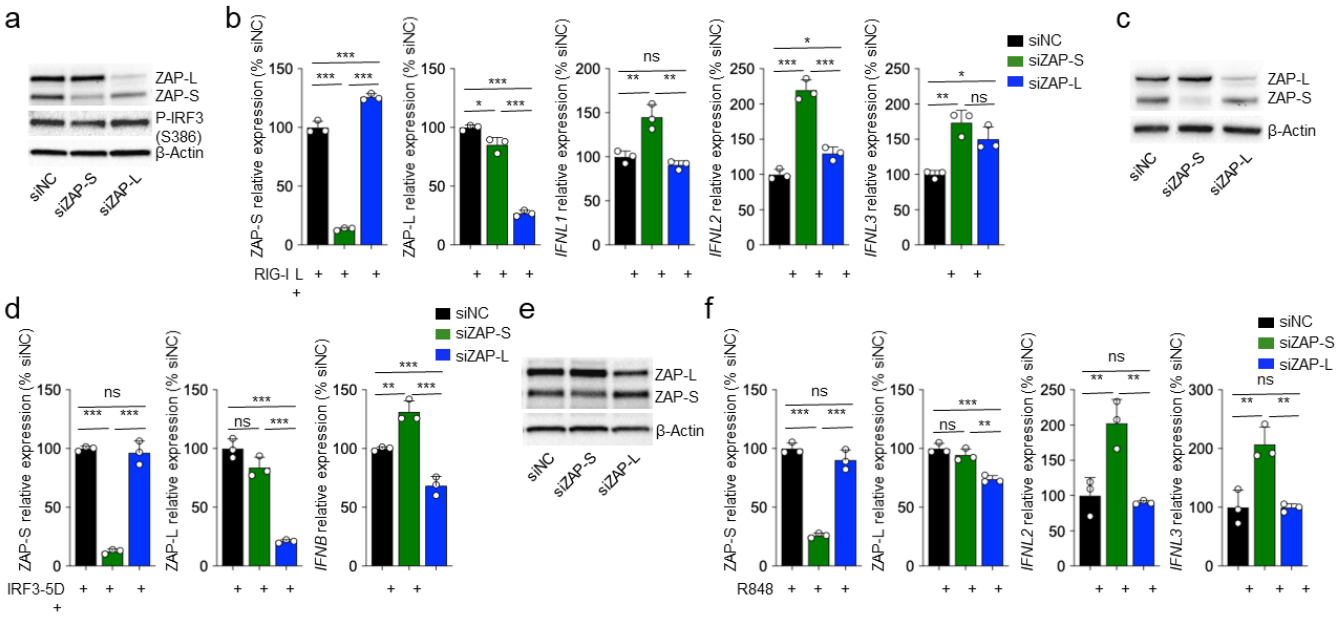

Figure 2.6. ZAP-S, but not ZAP-L suppresses IFN.

(a) Western blot of ZAP isoform expression and **(b)** *ZAP-S*, *ZAP-L*, *IFNB*, *IFNL2* and *IFNL3* mRNA expression in Huh7 wild-type cells after isoform-specific knockdown of ZAP and stimulation with 0.5 µg/ml poly U/UC RNA (RIG-I L) for 42 h. Bars show mean ± SD. **(c)** Western blot of ZAP isoform expression and **(d)** *ZAP-S*, *ZAP-L* and *IFNB* mRNA expression in Huh7 wild-type cells after isoform-specific knockdown of ZAP and overexpression of IRF3-5D for 42 h. Bars show mean ± SD. **(e)** Western blot of ZAP isoform expression and **(f)** *ZAP-S*, *ZAP-L*, *IFNL2* and *IFNL3* mRNA expression in CAL-1 cells after isoform-specific knockdown of ZAP and stimulation with 1 µg/ml R848 for 3 h. Bars show mean ± SD. For (a-f) data is representative of three independently performed experiments with replicates (n=3) and similar results. Data were analyzed using one-way ANOVA with Tukey's post-test. *P < 0.05; **P < 0.01; ***P < 0.001; ns, not significant.

a

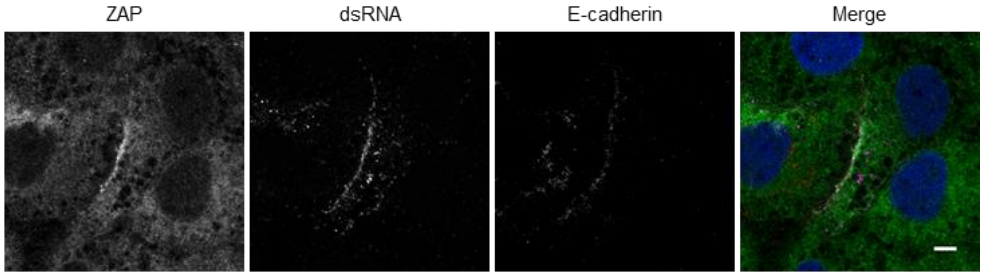
ZAP
dsRNA
E-cadherin
Merge

b

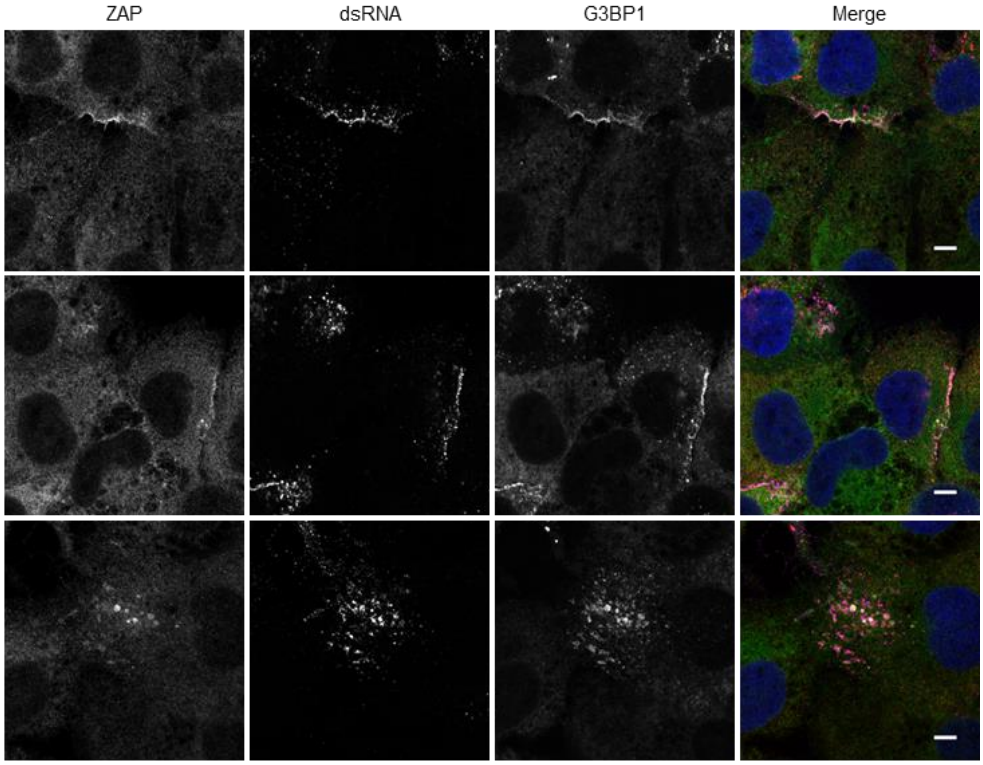
ZAP
dsRNA
G3BP1
Merge

c

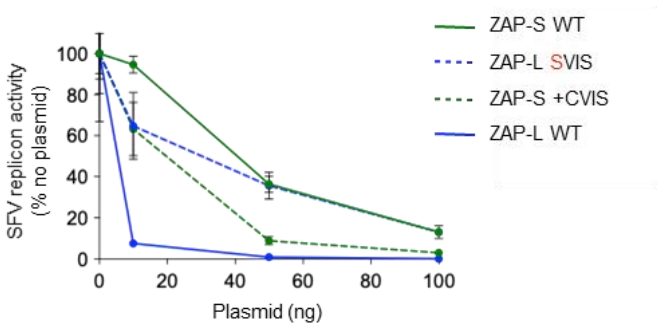
SFV replicon activity
(% no plasmid)
100
80
60
40
20
0
0
20
40
60
80
100
Plasmid (ng)
ZAP-S WT
ZAP-L SVIS
ZAP-S +CVIS
ZAP-L WT

Supplementary Figure 2.6 (related to 2.6).

(a) Confocal immunofluorescence microscopy of endogenous ZAP, SINV dsRNA, and E-cadherin in Huh7 WT cells upon infection with SINV Toto (MOI = 1; 6 h post-infection). The scale bar represents 5 µm. **(b)** Confocal immunofluorescence microscopy of endogenous ZAP, SINV dsRNA, and G3BP1 in Huh7 WT cells upon infection with SINV Toto (MOI = 1; 6 h post-infection). The scale bar represents 5 µm. (a, b) Representative micrographs of three independent experiments with similar results are shown. **(c)** Replication activity of a Semliki Forest virus (SFV) luciferase replicon in doxycycline-inducible HEK 293T cells expressing ZAP-S WT, ZAP-L WT, or their respective CaaX motif mutants. A representative experiment with replicates (n = 3) of three independently performed experiments with similar results are shown. Symbols show mean ± SD.

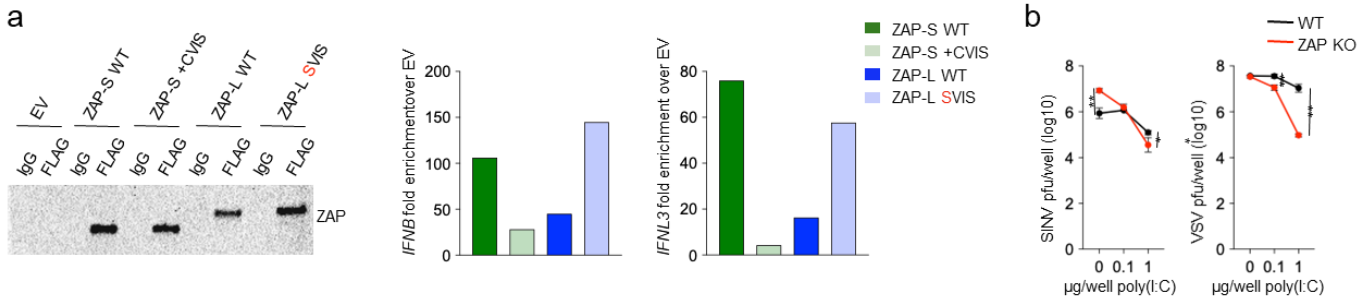

Figure 2.7. Localization of ZAP isoforms determines binding of IFN mRNA.

(a) RNA immunoprecipitation of FLAG-tagged WT ZAP-S, WT ZAP-L, their respective CaaX mutants, and empty vector (EV) control in Huh7 ZAP KO cells after stimulation with 0.25 µg/ml poly U/UC RNA for 24 h. A representative experiment of three independent experiments with similar results is shown. **(b)** SINV titers 16 hpi and Vesicular stomatitis virus (VSV) titers 12 hpi in Huh7 wild-type and ZAP KO cells with or without poly(I:C) pre-treatment for 16 h. Symbols show mean ± SD. Data is representative of three independently performed experiments with

replicates (n=3). Data were analyzed using two-way ANOVA with Tukey's post-test. *P < 0.01; **P < 0.001.

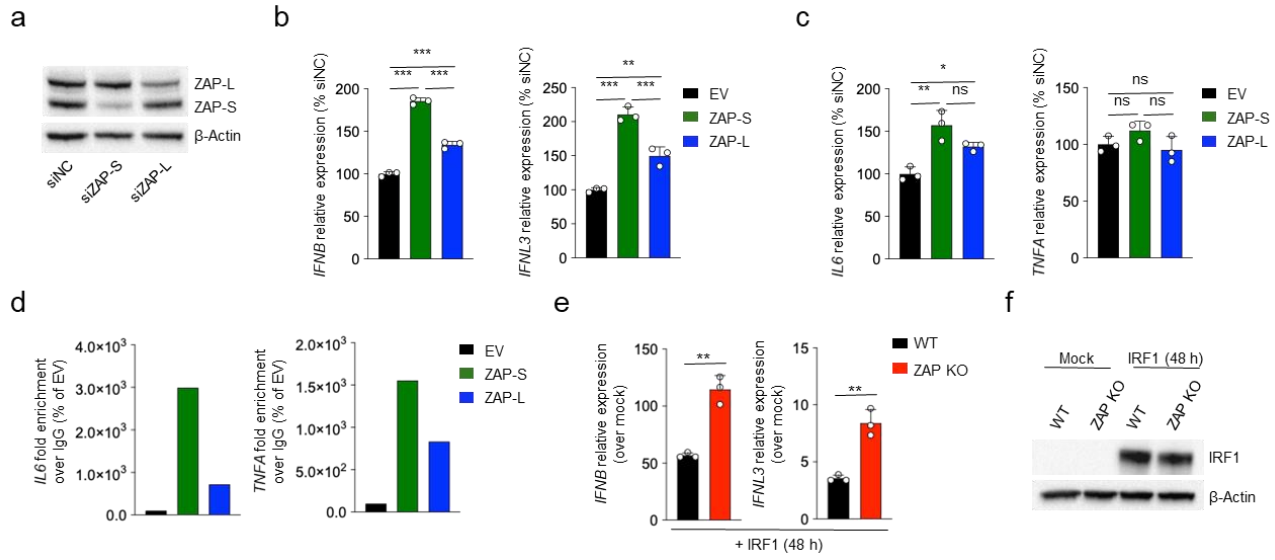

Supplementary Figure 2.7 (related to 2.7).

(a) Western blot of ZAP isoform expression and **(b)** *IFNB* and *IFNL3* mRNA expression in HEK 293 cells after isoform-specific knockdown of ZAP and stimulation with 1 µg/ml RIG-I ligand for 30 h. (a, b) A representative experiment with replicates (n = 3) of three independently performed experiments with similar results is shown. Bars show mean ± SD. **(c)** *IL6* and *TNFA* mRNA expression in Huh7 cells upon isoform-specific knockdown of ZAP and stimulation with 0.5 µg/ml RIG-I ligand for 42 h. A representative experiment with replicates (n =3) of two independently performed experiments with similar results is shown. Bars show mean ± SD. **(d)** ZAP RNA-IP performed in Huh7 ZAP KO cells after expression of FLAG-tagged ZAP-S, FLAG-tagged ZAP-L and FLAG-empty vector (EV) control, and stimulation with 0.2 µg/ml RIG-I ligand for 24 h. A representative experiment of two independently performed experiments with similar results is shown. **(e)** Expression of *IFNB* and *IFNL3* mRNA and **(f)** Western blot of IRF1 protein expression in Huh7 WT and ZAP KO cells 48 h after

overexpression of IRF1. (e, f) A representative experiment with replicates (n = 3) of three independently performed experiments with similar results is shown. Bars show mean ± SD. Data were analyzed using (b, c) one-way ANOVA with Tukey's post-test or (e) unpaired two-tailed Student's t-test. *P < 0.05; **P < 0.01; ***P < 0.001; ns, not significant.

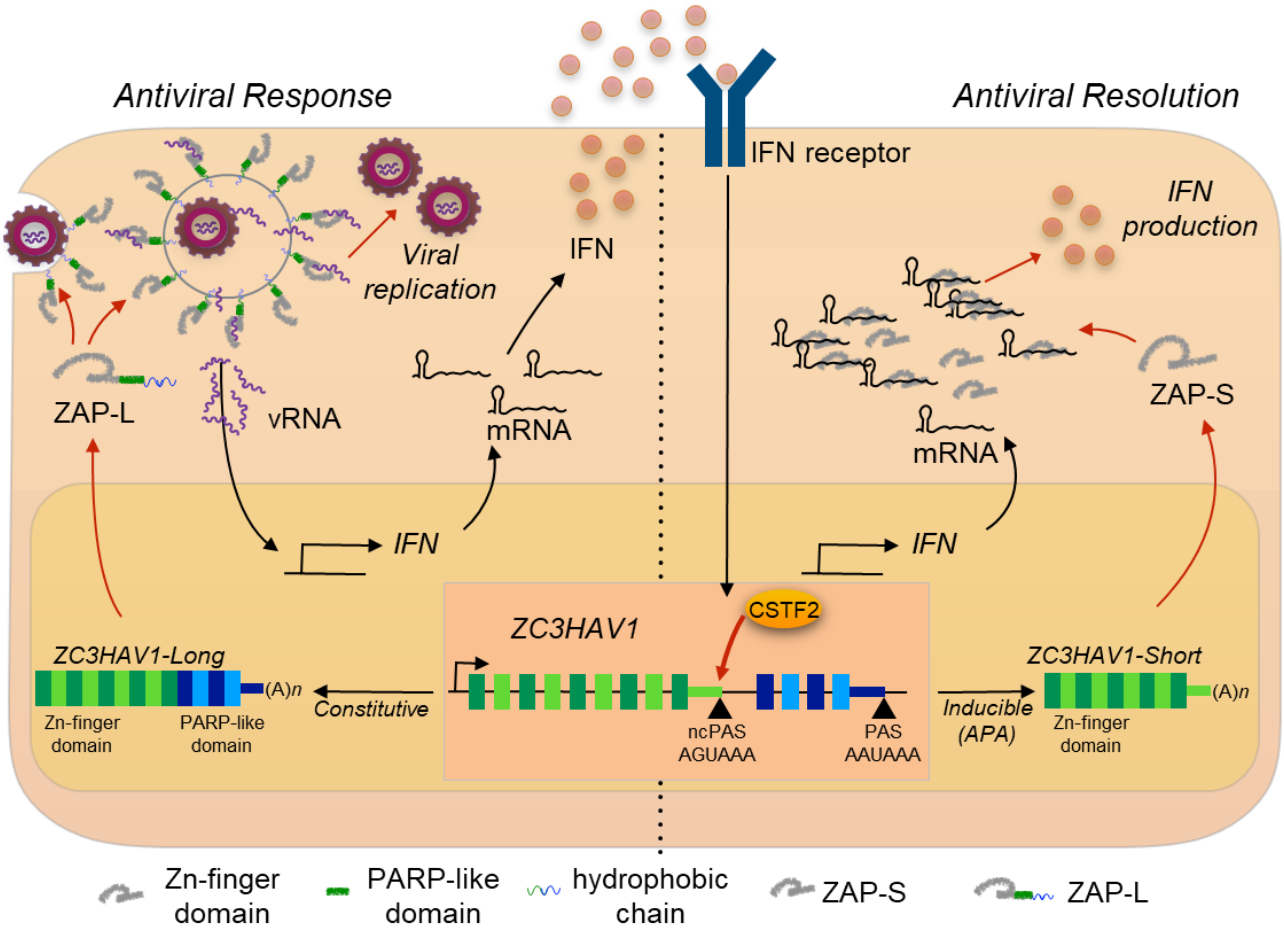

Supplementary Figure 2.8. Model.

Model of ZAP-mediated post-transcriptional regulation during innate antiviral immunity. Constitutively expressed ZAP-L localizes to endolysosomes and sites of Sindbis virus replication at the plasma membrane to target viral RNA (vRNA) and inhibit viral replication. Escaping vRNA triggers expression and secretion of type I and III IFNs, which engage and signal

through the IFN receptors. This induces CSTF2-mediated alternative polyadenylation and alternative last exon usage of ZC3HAV1 and expression of ZAP-S, which then binds to IFN mRNA in the cytoplasm to mediate resolution of the antiviral innate immune response.

Table 2.1. Overview of ZAP co-localization with different organelles.

Organelle	Marker	ZAP-S WT	ZAP-L WT	ZAP-S +CVIS	ZAP-L SVIS
Early endosome	Rab5	no	yes	yes	no
Late endosome	Rab7	no	yes	yes	no
Lysosome	LAMP1	no	yes	yes	no
Mitochondria	COX8	no	no	no	no
Endoplasmic reticulum	Sec61β	no	no	no	no
Peroxisomes	PTS1	no	no	no	no

Chapter 3. Endomembrane targeting of human OAS1 p46 augments antiviral activity

Frank W. Soveg*, Johannes Schwerk*, Nandan S. Gokhale, Karen Cerosaletti, Alison M. Kell, Adriana Forero, Katharina Esser-Nobis, Julian R. Smith, Justin A. Roby, Tien-Ying Hsiang, Snehal Ozarkar, Jonathan M. Clingan, Eileen T. McAnarney, Amy E. L. Stone, Uma Malhotra, Cate Speake, Joseph Perez, Chiraag Balu, Shivam A. Zaver, Jennifer Hyde, Joshua J. Woodward, Vineet D. Menachery, Saumendra N. Sarkar, Daniel B. Stetson, Jane H. Buckner, Michael Gale Jr., and Ram Savan.

*equal contribution

3.1 Introduction

Oligoadenylate synthetase (OAS) proteins are a family of innate viral RNA sensors critical for cell-intrinsic defense against viruses through activation of the latent endoribonuclease RNase L (*155*). Recognition of viral RNA induces a conformational change in OAS proteins to reveal a catalytic pocket where ATP is converted to the second messenger 2′-5′A (*156*). Binding to 2′-5′A dimerizes and activates RNase L, which proceeds to cleave cellular and viral RNA in order to block viral replication (*157*). Although the importance of RNase L in restricting a variety of viruses is well documented, it is unclear how individual OAS proteins contribute to this breadth of antiviral activity (*158*). Interestingly, the C-terminal region of human OAS1 is alternatively spliced to produce several isoforms resulting in protein products p42, p44, p46, p48, and p52, named according to their molecular weight (*159*). All human OAS1 isoforms share the first five exons of OAS1, which contain the RNA binding and catalytic domains, but each isoform splices a distinct sixth exon to generate unique C-termini. The specific antiviral roles of individual human OAS1 isoforms remain unexplored. The production of OAS1 p46 is controlled

by a SNP in the splice-acceptor site of exon 6 in OAS1 (rs10774671 A>G). The G allele of this SNP shifts the splice acceptor site in exon 6 by one nucleotide to generate p46, while other OAS1 isoforms, primarily p42, are produced when the A allele is present (*160*). OAS1 p46 is unique among OAS1 isoforms because it is the only isoform with a C-terminal CaaX (cysteine-aliphatic-aliphatic-any residue) motif. Proteins containing CaaX motifs at their C-termini undergo post translational lipidation termed prenylation and are targeted to the cytosolic face of intracellular organelle membranes of the endomembrane system following post-prenylation processing at the endoplasmic reticulum (*102*). The significance of the CaaX motif in OAS1 p46 and whether endomembrane targeting might alter the antiviral activity of OAS1 is unknown.

How the subcellular targeting of OAS family members impacts their specificity and antiviral activity is unclear. Most intracellular viral RNA sensors localize to the cytosol where they are poised to sense accumulating viral RNA during infection (*161, 162*). However, since many RNA viruses replicate in close association with intracellular membranes, placing OAS proteins at membranous compartments within cells may augment sensing in certain contexts. Notably, positive-strand RNA viruses, such as flaviviruses, picornaviruses and coronaviruses, replicate their RNA within modified host organelles of the endomembrane system (*163*). These replication organelles pose a problem for cytosolic innate immune sensors of viral RNA as they shield viral RNA from detection by sensors such as RIG-I (*79*). Whether or not the host has evolved strategies to surveil specific intracellular membranes for viral replication is unclear. We therefore hypothesized OAS1 p46, through its CaaX motif, is targeted to the endomembrane system and this targeting gives it enhanced access to viral RNA during infection. In support of this model, we show the prenylated isoform, OAS1 p46, is targeted to Golgi membranes and this membrane-targeting results in enhanced detection of viral RNA and augmented antiviral activity

against positive-strand RNA viruses such as flaviviruses, picornaviruses, and SARS-CoV-2. Our genetic data further supports OAS1 rs10774671 A/G as the causal variant that predicts severity of COVID-19. More broadly, this work reveals how intracellular membrane targeting of OAS1 is critical for detecting human pathogenic viruses that replicate on organelle membranes**.**

3.2 Results

3.2.1 The p42 and p46 isoforms of OAS1 are expressed in human cells

Alignment of the C-terminal regions of the five OAS1 isoforms revealed a C-terminal CaaX motif present only in the p46 isoform, which may impart this isoform with a unique function (Fig 3.1 A, S3.1 A, S3.1 C). OAS1 proteins from diverse vertebrate species have a CaaX motif at their C-termini, suggesting the CaaX motif has a critical role in the function of OAS1 (Fig S3.1 B). We determined the protein expression of OAS1 isoforms across several human cell lines and assessed the impact of the SNP (rs10774671) on the expression of OAS1 isoforms. This SNP is in the splice acceptor site of exon 6 in OAS1 and the G allele controls the production of the p46 isoform (*160*). Genotyping revealed the A549 cell line carried only the A allele, PH5CH8 and THP-1 cell lines had both the A and G alleles, and Daudi cells carried only the G allele at rs10774671 (Fig 3.1 B). We then treated these cells with interferon beta (IFNβ) and evaluated OAS1 protein expression by immunoblot using an N-terminal OAS1 antibody that recognizes all isoforms. We detected only two OAS1 isoforms at molecular weights of 42 and 46 kilodaltons in cells with at least one copy of the G allele (Fig 3.1 B). Only isoforms p42 or p46 were expressed in A/A or G/G cells, respectively, and only the p42 and p46 isoforms were detected after IFNβ treatment or Sendai virus infection (Fig S3.1 D). We did not observe expression of the p44, p48, or p52 isoforms. This outcome is consistent with previous reports

demonstrating the p44, p48, and p52 isoforms are weakly expressed at the mRNA level, and unstable at the protein level (*164, 165*).

3.2.2 The p46 isoform of OAS1 is geranylgeranylated

One of the major differences between OAS1 p42 and p46 is the presence of a C-terminal CaaX motif in p46 (Fig S3.1 C). Proteins containing CaaX motifs at their C-termini are prenylated and targeted to the cytosolic face of cellular membranes of the endomembrane system, including the endoplasmic reticulum and Golgi apparatus (*102*). Depending on the identity of the "X" amino acid, CaaX-containing proteins can be either farnesylated or geranylgeranylated by the respective farnesyl or geranylgeranyl transferases. CaaX motifs with a leucine in the "X" position are preferentially geranylgeranylated by geranylgeranyl transferase I (GGTaseI) (*101*). In order to test if the CaaX motif in p46 is geranylgeranylated, we performed an in vitro geranylgeranylation detection assay using a click chemistry approach (*166*). We generated OAS1 KO 293T cells using CRISPR/Cas9 gene editing (Fig S3.1 E). OAS1 KO 293T cells were transfected with N-terminal FLAG-tagged OAS1 p42, p46, p42CTIL, and p46ATIL expression constructs. The p42CTIL construct represents p42 with the addition of the CaaX (CTIL) motif from p46, which will allow us to test if the CaaX motif from p46 is sufficient to drive geranylgeranylation of p42. The p46ATIL construct was generated by mutating the CaaX cysteine to an alanine (C>A) to disrupt its prenylation, allowing us to test if this motif is necessary for its geranylgeranylation. Immunoblotting of the immunoprecipitated OAS1 proteins revealed CaaX-containing p46 and p42CTIL proteins were geranylgeranylated, while p42 and p46ATIL were not (Fig 3.1 C). These data confirm the p46, but not p42, isoform of OAS1 is geranylgeranylated and demonstrate the CaaX motif is necessary and sufficient for geranylgeranylation of OAS1.

3.2.3 OAS1 p46 localizes to the endomembrane system

Based on the differential geranylgeranylation of the p42 and p46 OAS1 isoforms, we hypothesized these proteins would localize to unique subcellular compartments. Since we verified the OAS1 isoforms produced in several human cell lines, we could stratify these cells into cells capable or incapable of producing p46. PH5CH8, THP-1, and Daudi cells all produce p46 while A549 cells only produce p42 (Fig 3.1 B), a fact we took advantage of to evaluate if OAS1 isoforms localize to different compartments under endogenous expression conditions. Using confocal laser scanning microscopy (cLSM), we observed OAS1 localization at a perinuclear compartment in p46-producing cells after IFNβ treatment, while, in contrast, OAS1 localized to the cytosol and nucleus in cells incapable of producing p46 (Fig S3.1 F). Co-staining with Golgin-97, a marker of the trans-Golgi network, identified this organelle as a site of OAS1 localization in p46-producing cells (Fig 3.1 D, E, S3.1 G). Cells capable of producing p46 showed a significant increase in OAS1 colocalization with the Golgi over A549 cells that only produce p42 (Fig 3.1 D, E, S3.1 G). These data demonstrate OAS1 localizes to an intracellular organelle membrane in cells capable of producing p46.

The endogenous localization patterns of OAS1 suggested the p42 and p46 isoforms localize to distinct subcellular compartments, a hypothesis we tested by performing cLSM on OAS1 KO Huh7 cells ectopically expressing p42 or p46 isoforms (Fig 3.1 F, G, S3.1 H). OAS1 localized to the Golgi in cells ectopically expressing p46, while the p42 isoform localized to the cytosol and the nucleus (Fig 3.1 F, G). Compared with p42, p46 showed significantly stronger localization to the Golgi (Fig 3.1 F, G). We next tested the contribution of the CaaX motif to the Golgi localization of p46 by expressing p46ATIL and evaluating its localization by microscopy. The CaaX mutant, p46ATIL (C>A), instead localized to the cytosol and nucleus, similar to p42,

indicating the CaaX motif is necessary for Golgi targeting of p46 (Fig 3.1 F, G). We then tested if adding the CaaX motif to the p42 isoform is sufficient to drive p42CTIL to the Golgi. Consistent with our hypothesis, ectopically expressed p42CTIL localized to the Golgi and showed significantly stronger localization to the Golgi over p42, confirming the CaaX motif is both necessary and sufficient to localize OAS1 isoforms to the Golgi (Fig 3.1 F, G). These findings were further confirmed in A549 cells, using OAS1 KO A549 cells ectopically expressing p42, p46, p42CTIL, and p46ATIL (Fig S3.1 I-K). When expressed in OAS1 KO Huh7 cells, the p44, p48, and p52 isoforms localized to the cytosol and nucleus in a manner similar to p42 (Fig S3.1 L, M) These experiments demonstrate the p46 isoform of OAS1 localizes to the endomembrane system, particularly the Golgi, in a prenylation-dependent manner.

3.2.4 OAS1 p42 and p46 are differentially antiviral

The differential localization of OAS1 isoforms led us to hypothesize these isoforms have differential antiviral activity. Specifically, localization of p46 to the endomembrane system led us to hypothesize this isoform may have enhanced antiviral activity against viruses that use these organelle membranes for replication. Encephalomyocarditis virus (EMCV) is a positive-strand RNA virus that is sensitive to the OAS/RNase L pathway and replicates on organelles of the endomembrane system, particularly ER and Golgi membranes (*167, 168*). We used this virus to investigate whether OAS1 isoforms confer different antiviral activity against a virus that uses the endomembrane system for replication. We transfected expression plasmids encoding p42, p46, or an empty vector control in OAS1 KO 293T cells, and then infected with EMCV at MOI of 0.001 at 24h post-transfection (Fig 3.2 A). At 24h post-infection, total RNA and culture supernatants were collected for qPCR on viral RNA or plaque assay, respectively. We found p42 expression

led to a significant five-fold reduction in vRNA over control, while p46 expression led to a significant fiftyfold reduction over EV and a significant ten-fold reduction over p42 at 24h post-infection (Fig 3.2 B). Quantification of viral titer from supernatants by plaque assay showed p46 expression led to a significant hundred-fold reduction in EMCV titer over control and a significant 50-fold reduction over p42. In contrast, the p42 isoform reduced EMCV titer by five-fold over control (Fig 3.2 C, S3.2 A). We also compared the antiviral activity of p44, p48, and p52 against EMCV over a range of doses and found their antiviral activity was inferior to p46 (Fig 3.2 D, E). These data demonstrate, among OAS1 isoforms, OAS1 p46 confers the strongest antiviral activity against EMCV.

Next, we tested the ability of endogenously expressed OAS1 isoforms to restrict EMCV using an siRNA knockdown approach in THP-1 cells (A/G at rs10774671), which express both the p42 and p46 isoforms. We transfected PMA differentiated THP-1 macrophages with siRNAs against both OAS1 isoforms, p42, or p46 and then infected with EMCV (Fig 3.2 F). Knockdown of total OAS1 or p46 led to a significant four-fold increase in viral titer compared to a non-targeting control (NC), whereas specific knockdown of p42 had no effect on viral titer compared to NC control siRNA (Fig 3.2 G, S3.2 B). Collectively, these data show major antiviral differences in OAS1 isoforms at endogenous levels of expression and support an important role for p46, but not p42, in restricting a virus that utilizes the endomembrane system for replication.

3.2.5 The antiviral function of OAS1 isoforms require catalytic activity and RNase L

The differences in the antiviral activity and localization of p42 and p46 led us to hypothesize these isoforms may utilize unique antiviral mechanisms. Both RNase L and 2′-5′A independent antiviral mechanisms have been documented for OAS proteins, but whether human OAS1 p42 and p46 isoforms differentially utilize 2′-5′A or RNase L is unknown (13, 18, 19). In

order to ablate catalytic activity and test if both OAS1 isoforms required 2′-5′A synthetase activity to be antiviral, we mutated two key aspartic acid residues required for synthetase activity, D75 and D77, in the catalytic core of p42 and p46 to alanine ($D^{75}A^{76}D^{77}$>$A^{75}A^{76}A^{77}$) which we will refer to as catalytic mutant hereafter (*169*). We expressed these catalytically inactive OAS1 isoforms alongside their corresponding wild type constructs and tested their ability to restrict EMCV (Fig 3.3 A). As before, expression of p42 and p46 in OAS1 KO cells reduced EMCV vRNA. However, the catalytically inactive OAS1 constructs failed to reduce levels of EMCV viral RNA (Fig 3.3 B). Additionally, compared to the control, expression of p42 and p46 significantly reduced EMCV viral titer (p42, tenfold; p46, hundredfold) and both isoforms required catalytic activity for antiviral function, as expression of the catalytic mutants did not reduce EMCV titer compared to the control (Fig 3.3 C). Furthermore, the catalytic mutants failed to reduce EMCV RNA compared to their wild type counterparts over a range of protein expression (Fig S3.3 A, B). These data indicate the ability to synthesize 2′-5′A is essential for the antiviral activity of OAS1 p42 and p46 against EMCV.

We next tested if p42 and p46 require RNase L for their antiviral activity by expressing p42 or p46 in RNase L-deficient 293T cells (Fig 3.3 D, S3.3 C). Compared to non-targeted Cas9 control cells, expression of p42 and p46 in RNase L KO 293T cells had no impact on EMCV vRNA or titers (Fig 3.3 E, F). Next, we tested if RNase L expression was sufficient to rescue the antiviral activity of OAS1 isoforms in RNase L KO 293T cells. For this, RNase L was ectopically expressed in RNase L KO 293T cells (Fig S3.3 D). Cells complemented with RNase L and expressing p46 showed a significant reduction in EMCV RNA and titer over control (Fig S3.3 E, F). Although not significant, complementing p42 expressing cells with RNase L showed

a trend in reducing viral RNA and titer (Fig S3.3 E, F). These experiments show that RNase L is required for the antiviral activity of OAS1 p42 and p46 against EMCV.

Cleavage of cellular RNA by RNase L has been shown to generate immunostimulatory RNAs that are sensed by RIG-I and MDA5 and increase antiviral protection through the production of interferon (*170*). To test if the differences in antiviral activity of p42 and p46 could be explained by differential production of immunostimulatory RNAs, we tested the antiviral activity of p42 and p46 in wild type or IRF3 KO 293FT cells (Fig 3.3 G). In wild type cells, p42 and p46 reduced EMCV RNA significantly over the control. Importantly, loss of IRF3 expression did not impede the ability of p46 to restrict EMCV, as EMCV RNA was significantly reduced over control in IRF3 KO cells expressing p46 (Fig 3.3 H). Expression of p42 in IRF3 KO cells showed a trend towards reducing EMCV RNA (Fig 3.3H). These data confirm p42 and p46 are antiviral in the absence of additional factors that are induced by IRF3. Collectively, these data demonstrate p42 and p46 both use the 2′-5′A/RNase L pathway to confer antiviral activity and that some other feature must be important for their differential antiviral activities.

3.2.6 Endomembrane targeting of p46 through the CaaX motif enhances access to viral RNA

Since the CaaX motif localizes p46 to the endomembrane system, we investigated if this motif played a role in the enhanced antiviral activity of p46 against EMCV. During picornavirus infection, utilization of ER and Golgi membranes for replication organelle biogenesis results in population of the cytosol with replication compartments that are sites of vRNA synthesis (*24*, *167*). Therefore, we hypothesized endomembrane localization of p46 places this viral RNA sensor on membranes utilized by EMCV for replication and would allow p46 enhanced access to EMCV RNA. In contrast, p42 would have limited access to viral RNA as it is localized to the

cytosol and nucleus. We determined the localization of p42 and p46 during EMCV infection by infecting OAS1 KO Huh7 cells expressing p42 or p46 with EMCV and then stained for OAS1 and dsRNA followed by cLSM. In mock infected cells expressing p46, this isoform was localized to perinuclear structures (Fig 3.4 A). In cells infected with EMCV, p46 was no longer perinuclear and instead redistributed throughout the cell to sites of vRNA accumulation (Fig 3.4 A). In contrast, p42 remained in the cytosol and nucleus before and after infection (Fig 3.4 A). These data suggest p46 is proximal to sites of EMCV vRNA replication. We next used an RNA immunoprecipitation approach to test whether OAS1 p46 has enhanced access to EMCV viral RNA and if the CaaX motif is important for its ability to bind viral RNA. Since RNase L cleaves RNA and is required for OAS1 mediated restriction of EMCV, RNase L deficient Huh7 cells allowed us to test OAS1 isoform binding to EMCV RNA in samples with equivalent amounts of viral RNA (Fig 3.4 B). N-terminally FLAG-tagged OAS1 p42, p46, p42CTIL and p46ATIL isoforms were expressed in OAS1 KO Huh7 cells, which are also devoid of RNase L expression (Fig S3.4 A). Expression of OAS1 isoforms in OAS1 KO Huh7 cells had no impact on viral RNA levels (Fig 3.4 B). However, qPCR on EMCV RNA after FLAG immunoprecipitation revealed p46 trended to bind more vRNA than p42 (Fig 3.4 B). Adding a CaaX motif to p42 (p42CTIL) did not significantly increase the ability of p42 to pull down vRNA (Fig 3.4 B). In contrast, mutating the CaaX motif on p46 (p46ATIL) caused a significant loss in vRNA binding (Fig 3.4 B). These data confirm endomembrane targeting through the CaaX motif is required for the p46 isoform to bind EMCV RNA, as mutating the CaaX motif completely ablated the ability of p46 to access viral RNA (Fig 3.4 B).

We next tested the importance of the CaaX motif to the antiviral activity of OAS1 by expressing p42, p46, p42CTIL, or p46ATIL in OAS1 KO 293T cells followed by infection with

EMCV (Fig 3.4 C). Compared to cells expressing p46, cells expressing CaaX-mutant p46ATIL showed a significant five-fold increase in EMCV RNA as well as an increase in viral titer (Fig 3.4 D, E); a decreased antiviral activity similar to the p42 isoform. Intriguingly, addition of a CaaX motif to OAS1 p42 did not increase the antiviral activity of p42 (Fig 3.4 D, E). One possible explanation for this discrepancy could be that the peptide sequence in the unique C-terminus of p42 contains a motif that is inhibitory to its antiviral activity. We therefore generated another OAS1 variant which contains a CaaX motif directly downstream of the common OAS1 peptide sequence shared between all OAS1 isoforms, hereinafter referred to as OAS1 common+CTIL (Fig 3.4 F). We tested the antiviral activity of OAS1 common+CTIL compared to the p42 and p46 isoforms. At similar protein expression levels, OAS1 common+CTIL did not confer significantly increased antiviral activity over the empty vector control and showed viral RNA levels similar to those in cells expressing the p42 isoform (Fig 3.4 G, H). Interestingly, the OAS1 common+CTIL variant showed significantly decreased colocalization with Golgi membranes compared to p46 and appeared cytosolic and nuclear, as observed above for CaaX-deficient p42 (Fig S3.4 B). Together, these data indicate membrane targeting of OAS1 p46 through a CaaX motif is crucial for its antiviral activity against EMCV. However, a CaaX motif alone is not sufficient to provide optimal antiviral activity against EMCV. Overall, these data suggest other features in the unique C-termini of OAS1 p42 and p46 contribute to their individual antiviral activity.

3.2.7 Combined effects of CaaX motif, C-terminus length and oligomerization domain confer differential antiviral activity of OAS1 isoforms

Since the unique C-terminus of p46 is longer than the unique C-terminus of p42 (50 versus 18 amino acids), we tested if the unique sequence in p46 contains additional motifs

important for its antiviral activity. We tested this by generating sequential hexameric alanine substitution mutants throughout the C-terminus of OAS1 p46 and compared their antiviral activity against EMCV alongside p46 and CaaX-deficient p46ATIL (Fig 3.5 A). As expected from our previous experiments, p46ATIL had reduced antiviral activity when compared with p46 (Fig 3.5 B, 3.5 C, S3.5 A). However, compared to p46, none of the alanine substitution mutants affected viral RNA levels significantly (Fig 3.5 C, S3.5 A). Notably, mutant 8 showed a trend toward increased EMCV RNA levels, suggesting the mutated amino acids in this mutant might contribute to the antiviral activity of OAS1 p46. Although OAS1 p46 mutant 8 localized to the Golgi, compared with p46, this mutant had a slight but significant decrease in its correlation with Golgin-97 (Fig. S3.5 B, C). In fact, the $E^{392}E^{393}D^{394}$ peptide sequence is conserved in most mammalian OAS1 p46 orthologous isoforms, which suggests a function for this motif (Fig S3.1 B). Nevertheless, none of the alanine substitution mutants affected EMCV RNA levels as strongly as p46ATIL.

Previous studies have demonstrated a three amino acid motif ($C^{331}F^{332}K^{333}$), present in all OAS1 isoforms, is critical for OAS1 oligomerization and 2′-5′A production (*171*). The CFK motif is close to the unique C-termini of p42 and p46, however, the requirement of the CFK domain for the antiviral activity of these proteins is unknown. Therefore, we generated OAS1 p42 and p46 CFK mutants ($C^{331}F^{332}K^{333} \rightarrow A^{331}A^{332}A^{333}$) and compared their antiviral activity against EMCV to their wild type counterparts. Relative to wild type p42 and p46, mutation of the CFK domain led to a significant loss in the ability of p42 and p46 to reduce EMCV RNA by threefold and twofold, respectively (Fig 3.5 D, E). Strikingly, ablation of the CFK motif in p42 resulted in complete loss of its antiviral activity, demonstrated by similar EMCV RNA levels as cells expressing an empty vector control (Fig 3.5 D, E). Interestingly, loss of the CFK motif in

p46 did not completely ablate the antiviral activity of this isoform. EMCV RNA levels in p46 CFK mutant expressing cells were similar to those cells expressing p42 (Fig 3.5 D, E). Mutating the CFK motif on OAS1 did not alter the localization of either isoform (Fig S3.5 D, E). This suggests that the antiviral activity of OAS1 p42 is completely dependent on the CFK oligomerization motif, whereas p46 only partially depends on the CFK oligomerization motif for its antiviral activity.

Since p46 is prenylated and embedded in cellular membranes, the longer C-terminus of p46 may function as a flexible linker to facilitate optimal oligomerization. This may explain why adding a CaaX motif to p42 is not sufficient to enhance its antiviral activity (see Fig 3.4 C-E). To test this, we generated several C-terminal truncation mutants of p46 termed p46 Δ 12aa, Δ 22aa, and Δ 32aa, respectively, and tested their antiviral activity against EMCV alongside p46 and p42CTIL (Fig 3.5 F). Compared to p46, the truncation mutants showed a length dependent decrease in their ability to reduce EMCV RNA (Fig 3.5 G, H). The Δ 22aa and Δ 32aa deletion mutants had similar antiviral activities as p42CTIL, which is identical in length to the Δ 32aa mutant (Fig 3.5 H). Compared with p46, all the p46 truncation mutants localized to the Golgi (Fig S3.5 F). However, there was a slight but significant decrease in the correlation of p46 Δ 32aa with the Golgi (Fig S3.5 G). These data suggest that, in addition to the CaaX motif and an oligomerization domain, the C-terminal length of p46 is important for its antiviral activity.

3.2.8 OAS1 p46 has broad antiviral activity against viruses that use the endomembrane system for replication

We sought to define the antiviral activity of OAS1 isoforms against other positive-strand RNA viruses that use the endomembrane system for replication. We tested if OAS1 isoforms are differentially antiviral against WNV by infecting OAS1 KO 293T cells expressing p42, p46, or

control with WNV. West Nile Virus, like all flaviviruses, replicates on membranes of the endomembrane system, primarily ER-derived membranes (*172*). Expression of p46 led to a 90% reduction in WNV titer relative to control, while p42 did not significantly impact WNV titer (Fig 3.6 A). These data demonstrate p46 has enhanced antiviral activity against WNV.

We tested if the enhanced antiviral activity of p46 against West Nile virus could be explained by p46 localizing to sites of flavivirus RNA replication. We used cLSM to evaluate the localization of p42 and p46 during flavivirus infection. We infected OAS1 KO 293T cells expressing p42 and p46 with WNV, followed by staining for OAS1, dsRNA, and the endoplasmic reticulum protein disulfide-isomerase A3 (PDIA3), since WNV replicates within invaginations of the ER membrane. During WNV infection, we observed p42 in the cytosol and p42 did not appear to be recruited to sites of WNV RNA production (Fig 3.6 B, bottom panel, arrows). However, during WNV infection, p46 localized to PDIA3-positive replication sites (Fig 3.6 B, top panel, arrows). Quantification of OAS1 isoforms relative to PDIA3 revealed a significant increase in the correlation of p46, but not p42, to PDIA3-positive membranes during infection, suggesting p46 is recruited to sites of WNV replication (Fig 3.6 B, C). Quantification of OAS1 isoform localization to viral RNA revealed OAS1 p46 has significantly stronger localization to dsRNA during WNV infection than p42 (Fig 3.6 D).

We evaluated whether p46 was present in the Golgi during WNV infection by staining for OAS1, Golgin-97, and dsRNA in cells infected with WNV. OAS1 p46 was significantly more correlated with the Golgi than p42 in both uninfected and WNV-infected cells (Fig S3.6 A, B). However, WNV infection caused a significant decrease in the association of p46 with Golgin-97 (Fig S3.6 A, B). This suggests p46 may be recruited from the Golgi to sites of WNV

replication. This is consistent with previous observations that Golgi membranes and proteins, including RNA binding proteins, are recruited to the replication organelles of flaviviruses (*173*). Zika virus is another flavivirus that utilizes ER membranes for replication, and we tested if p46 localizes to sites of ZIKV replication at the ER (*26*). We saw p46, but not p42, localized to the replication sites of Zika virus at the ER (Fig S3.6 C). Overall, these data suggest endomembrane localization of OAS1 p46 allows this protein to access sites of flavivirus RNA replication.

The human pathogenic picornavirus coxsackievirus B3 (CVB3) replicates within modified Golgi membranes and thus p46 may also be positioned to readily sense CVB RNA (*24*). We tested the antiviral activity of OAS1 p42 and p46 against CVB3 by infecting OAS1 KO 293T cells expressing p42, p46 or a control. Analysis of CVB RNA at 24h post infection revealed a 70% reduction in viral RNA in p46 expressing cells compared to control, while p42 had almost no effect on viral RNA (Fig S3.6 D). When we evaluated CVB3 titers at 48h post infection, we found p46 expression led to a significant 50% reduction in viral titers (Fig 3.6 E). These data suggest OAS1 p46 may have broad antiviral activity against members of the picornavirus family, while p42 is less effective.

Coronaviruses, another family of positive-strand RNA viruses, use the endomembrane system for replication using primarily endoplasmic reticulum-derived membranes (*11, 163*). We therefore hypothesized p46 may have enhanced antiviral activity against coronaviruses. We assessed the antiviral activity of p42 and p46 against SARS-CoV-2. Expression of p42 led to a five-fold reduction in SARS-CoV-2 titer (Fig 3.6 F). However, p46 had a significant five-fold greater antiviral activity over p42 (tenfold over EV) against SARS-CoV-2 (Fig 3.6 F). Importantly, the enhanced antiviral activity of p46 against SARS-CoV-2 depended on the CaaX motif, as p46ATIL lost antiviral activity relative to p46 and had decreased antiviral activity

similar to p42. This suggests endomembrane targeting of p46 is critical to its enhanced antiviral activity against SARS-CoV-2 (Fig 3.6 F).

We next tested the antiviral activity of p42 against RNA viruses that do not replicate on intracellular organelle membranes. Influenza A virus (IAV), a negative-sense RNA virus, replicates within the nucleus where p42 also localizes and is sensitive to the OAS/RNase L pathway (*174, 175*). To test if OAS1 isoforms are differentially antiviral against IAV, we infected OAS1 KO 293T cells expressing p42, p46, or a control with influenza A/PR/8/34 (Fig S3.6 E). Viral RNA analysis revealed neither OAS1 isoform impacted IAV RNA levels significantly at 24h post infection. Mutations in IAV NS1 disrupting RNA binding render this virus sensitive to the OAS/RNase L pathway, although it is unclear if OAS1 isoforms are differentially antiviral against IAV (*175*). We found expression of p42 or p46 had no impact on the replication of this NS1-mutant IAV (Fig S3.6 F). Collectively these data suggest OAS1 p46 is broadly antiviral against viruses that use the endomembrane system for replication.

3.2.9 OAS1 rs10774671 is associated with severe COVID-19 disease.

Since the OAS1 rs10774671 A/G variant generates the OAS1 p42 and p46 isoforms, respectively, that affected the response to SARS-CoV-2 infection, we tested whether this SNP is associated with COVID-19 disease severity. We hypothesized that the A allele, that encodes the p42 isoform would increase the risk of severe COVID-19 complications due to reduced antiviral activity compared to the G allele that generates p46. To test this, we genotyped the rs10774671 SNP in 35 COVID-19 severe cases (hospitalized, requiring mechanical ventilation) and 99 ancestry matched healthy controls (Table S3.3). Association was tested by logistic regression, adjusting for sex and ancestry. We detected association of rs10774671 in severe COVID-19 cases ($p=0.017$, Odds Ratio 2.85, 95% CI 1.20-6.76) using a recessive model with AA as the risk

genotype, indicating that even one copy of the G allele encoding p46 was protective for severe COVID-19 disease (dominant model p=0.017, Odds Ratio 0.35, 95% CI 0.15-0.83). Thus, homozygosity for the A allele at OAS1 rs10774671 encoding the OAS1 p42 isoform contributes genetic risk for severe disease in SARS-CoV-2 infected patients even in this small cohort.

3.3 Discussion

In this study, we show endomembrane targeting of OAS1 p46 bestows this isoform with enhanced antiviral activity against viruses that use the endomembrane system for replication. The p46 isoform contains a functional CaaX motif that targets this isoform to the endomembrane system, primarily to Golgi membranes, while other OAS1 isoforms localize to the cytosol and nucleus. Compared with p42, the p46 isoform has enhanced antiviral activity against picornaviruses, flaviviruses, and SARS-CoV-2, all viruses that replicate their RNA within modified organelles of the endomembrane system (*11, 24, 26, 167*). Although replicating in these modified endomembrane compartments is an important immune evasion strategy of positive-strand RNA viruses, out data shows localizing OAS1 p46 to the endomembrane system results in enhanced access to viral RNA and activation of RNase L dependent antiviral activity. In contrast, p42, which is localized to the cytosol and nucleus, has comparatively weak ability to sense viral RNA and initiate antiviral activity against viruses that replicate within intracellular membranes.

Placement of innate immune sensors at intracellular membranes is an antiviral strategy likely difficult for positive-strand RNA viruses to evade, as these viruses are unlikely to evolve away from this fundamental replication strategy. Secondly, many positive-strand RNA viruses depend on lipid products of the mevalonate pathway or prenylation for replication and therefore

cannot broadly antagonize this pathway (*176*). Viral antagonism by specifically targeting OAS1 p46 protein or directly blocking its prenylation or splicing could be possible. Alternatively, viral interference of the OAS-RNase L pathway would negate the antiviral activity OAS1 p46.

We also show addition of the CaaX motif to p42 is not sufficient to enhance its ability to bind viral RNA or increase its antiviral activity. This suggests the CaaX motif is just one of the crucial features in the unique OAS1 p46 C-terminal region that contributes to differential antiviral activity. Tetramerization of OAS1 has been proposed as a requirement for synthesis of the second messenger 2′-5′A, indicating that several OAS1 molecules in close proximity are required to induce 2′-5′A synthesis upon viral RNA binding and to subsequently activate the RNase L pathway (*171*). Aggregation of several OAS1 proteins around viral dsRNA might also increase the number of RNA-binding domains within the OAS1/vRNA complex, thereby allowing access to longer vRNA and increased 2′-5′A synthesis. Mutation of the CFK oligomerization motif in OAS1 p42 led to a complete loss of antiviral activity, while the p46 CFK mutant maintained antiviral activity similar to that of the wildtype p42 isoform. This suggests a model in which OAS1 p46 without a functional CFK oligomerization domain still maintains residual antiviral activity. These data show p46 proteins might oligomerize which is further aided by CaaX motif-mediated localization at Golgi membranes. Together, we have defined features including the CaaX motif in the unique C-terminus that contribute to the enhanced antiviral activity of p46. The unique alternatively spliced C-terminal region including the oligomerization and prenylation motifs in p46 is maintained across vertebrates presumably because it displays the strongest antiviral activity compared to other OAS1 isoforms (Fig. 7).

The G allele controlling OAS1 p46 expression was originally identified as a West Nile virus resistance allele, although the mechanism accounting for the protection conferred by this SNP was lacking (*160*). In this study, we also show this OAS1 splice site variant affects COVID-19 outcome. We found the A allele contributes to genetic risk for severe COVID-19 disease in patients who required mechanical ventilation compared to healthy control subjects. We propose the G allele association with protection against severe COVID-19 is explained by the enhanced antiviral activity of OAS1 p46 against SARS-CoV-2, which contributes to early control of viral replication. We have shown that the splice-site SNP controls the subcellular targeting of a critical viral RNA sensor, OAS1, which may allow the host to respond to viral evolutionary pressures and replication strategies. Interestingly, the G allele is ancestral and prevalent in African populations, in contrast the A allele is prevalent in rest of the world. Previous studies have documented reintroduction of the G-allele into Homo sapiens populations by introgression from Neanderthals and this could have implications for COVID-19 disease (*177*). This suggests there are strong selective pressures, presumably viral, impacting the prevalence of this causal splice site-SNP in human populations. Although we did not identify this in our study, we predict OAS1 p42 confers resistance to some important human pathogen. This is further supported by the genetic association of the A allele with multiple autoimmune disorders, as enhanced immune responses are sometimes made at a tradeoff for overall host fitness (*164, 178, 179*).

The broad number of RNA- and even DNA-viruses inhibited by the OAS/RNAse L pathway has raised interesting questions about the determinates of OAS antiviral specificity (*158*). In humans, the OAS family is comprised of three catalytically active OAS proteins: OAS1, OAS2, and OAS3. OAS1 contains an RNA binding domain and a catalytically active domain, while OAS2 contains a catalytically inactive repeat of this unit, and OAS3 contains two

catalytically inactive repeats of this unit (*155*). Although the OAS proteins have different RNA binding capabilities and favor synthesis of different lengths of 2′-5′A, we demonstrate a novel mechanism where subcellular localization also determines the antiviral specificity of these proteins (*180*). Based on the reduction of vRNA in our study, we propose a model in which 2′-5′A locally activates RNase L around sites of viral replication.

To conclude, this work highlights intracellular targeting as a crucial determinant for the specificity of OAS1. By positioning viral RNA sensors at different subcellular sites of viral RNA accumulation, the host can potentially respond to diverse replication strategies in the cytosol, nucleus, or on intracellular membranes. Although this work focused on OAS1 and the detection of viral nucleic acids, subcellular targeting is likely also important for function of other OAS proteins. This work opens the door for future studies on the subcellular localization of other OAS proteins, which will help clarify how this innate sensing pathway is able to respond to viral pathogens with diverse intracellular replication strategies.

3.4 Materials and Methods

Cell culture conditions and treatments

All cells were incubated at 37° C with 5% CO2. HEK293T, A549, Vero, PH5CH8, Huh7, and HeLa cells were grown in DMEM (Sigma) containing 10% heat-inactivated fetal bovine serum (FBS) (Atlanta Biologicals) and 1% penicillin-streptomycin-glutamine (Mediatech). Daudi cells were cultured in RPMI 1640 (Sigma) containing 10% heat-inactivated FBS (Atlanta Biologicals) and 1% penicillin-streptomycin-glutamine (Mediatech). THP-1 cells were cultured in RPMI 1640 (Sigma) containing 10% heat-inactivated FBS (Atlanta Biologicals), 1% penicillin-streptomycin-glutamine (Mediatech), 10 mM Hepes (Corning), 1x NEAA (Corning), 1 mM sodium pyruvate (Corning), and 50 μM 2-mercaptoethanol (Sigma).

Where applicable, THP-1 cells were differentiated in THP-1 media containing 40 nM of PMA (Sigma-Aldrich) for 24h. Recombinant human IFNβ (PBL Interferon Source) was used at 200-1000 IU/mL.

Generation of knockout cell lines using CRISPR/Cas9 gene editing

Cloning of OAS1 targeting guide RNA (gRNA) 5′-GTGCATGCGGAAACACGTGTCTGG-3′ into pRRLU6-empty-gRNA-MND-Cas9-t2A-Puro vector or RNase L targeting gRNA 5′-GTTATCCTCGCAGCGATTGCGGGG-3′ into pRRLU6-empty-gRNA-MND-Cas9-t2A-Blast was achieved using the In-Fusion enzyme mix (Clontech). OAS1 and RNASEL KO 293T were generated using lentiviral transduction as described previously followed by selection in 2 μg/mL puromycin or blasticidin (*181*). Transient transfection was utilized to knockout OAS1 in A549 and Huh7 cells. Cells were transfected with OAS1 gRNA or a Cas9-expressing control vector using TransIT-X2 (Mirus Bio) according to the manufacturer's instructions. At 24h post transfection, cells were selected with 2 μg/mL puromycin. Knockouts were validated by western blotting.

Generation of 293T-ACE2 cells

Lentiviral expression vector for ACE2 (pLEX-ACE2) was generated by amplifying the ACE2 sequence from cDNA from Huh7 cells 5′-GACTCTACTAGAGGATCCGCCACCATGTCAAGCTCTTCCTGGCTCC-3′ and 5′-GGGCCCTCTAGACTCGAGCTAAAAGGAGGTCTGAACATCATCAGTG-3′. This amplicon was cloned into a pLEX lentiviral backbone cut with BamHI and XhoI using the InFusion HD kit

(Takara). pLEX-ACE2 was co-transfected with psPAX2 and pMD2.G into 293FT cells for lentiviral packaging. 293T cells were transduced with ACE2-expressing lentivirus and selected with puromycin (2 μg/mL) for 4 days to generate 239T-ACE2 cells. ACE2 expression was verified by immunoblot (Proteintech).

Immunoblotting

Cells were lysed in RIPA buffer (+1× HALT protease and phosphatase inhibitor), and 10-30 μg total protein from whole-cell lysates was run on SDS–PAGE and transferred to polyvinylidene difluoride membranes (Thermo Scientific). The membranes were blocked in 5% milk in PBS-T (pPBS/Tween 20). Primary antibody incubation with antibodies against OAS1 (CST), RNase L (CST), or FLAG (Sigma) were performed in 5% milk in PBS-T overnight at 4°C. Membranes were washed for 5 minutes in PBS-T three times. Secondary antibody incubation was performed in 5% milk in PBS-T at room temperature for one hour and after membranes were washed for 5 minutes in PBS-T three times. Membranes were imaged on a Chemidoc XR system.

OAS1 siRNA knockdown

Dicer-substrate short interfering RNAs against a common region of OAS1 or the unique 3′UTR of p42 or p46 were custom designed and procured from Integrated DNA Technologies (Table S1). THP-1 cells were differentiated with PMA for 24h. At 24h post treatment, cells were transfected with 20 nM of siRNA using TransIT-X2 (Mirus Bio) according to the manufacturer's instructions. Viral infections were performed at 24h post-transfection.

Cloning

Expression plasmids encoding OAS1 p42, p42CTIL, p44, p46, p46ATIL, p48 and p52 were generated by Gibson assembly of the common OAS1 sequence with the isoform-specific sequence into the pCDNA3.1 vector (Table S1). Empty pcDNA3.1 was cut using BamHI and XbaI. A Gibson assembly compatible fragment for the common sequence of OAS1 was PCR-amplified from an OAS1 expression plasmid (gift from Dan Stetson) using primers 5′-TGGTACCGAGCTCGATGATGG ATCTCAGAA-3′ and 5′-CAGCAGAATCCAGG AGCTCACTGG-3′. Gibson assembly compatible fragments for the unique sequences of p42, p42CTIL, and p44 were generated by PCR amplification of annealed sense and antisense oligos (Table S1). Gibson assembly compatible sequences for the unique portions for p46, p46ATIL, and p48, were generated by PCR amplification of gBlocks. N-terminal FLAG-tagged versions of OAS1 p42 and p46 were generated by cutting pcDNA3.1 OAS1 p42, p42CTIL, p46 and p46ATIL with BamHI and cloning of a 3xFLAG fragment by PCR amplification from pEF FLAG-ZAP-L (*182*) and Gibson assembly using primers 5′-CGACTCACTATAGGGAGACCCAAGCTTGGTACCGAGC TCGATGGACTACAAAGAC-3′ and 5′-GTCCAGAGATTTGGCTGGGGTATTTC TGAGATCCATCATGCTTGTCATCGTCATCCTTGTAATCGATG-3′ (Table S1). Expression plasmids encoding p42DADA, p46DADA in pCDNA3.1 were generated by site-directed mutagenesis on pCDNA3.1 p42 or p46. FLAG-tagged expression plasmids encoding p46 common+CTIL, p46 alanine mutant 9, p46 Δ12aa, p46 Δ 22aa, p46 Δ 32aa, p42 CFK mutant, and p46 CFK mutant were generated by site-directed mutagenesis on pCDNA3.1 FLAG-p46. Site-directed mutagenesis was performed using the QuikChange Lightning kit (Agilent) according to the manufacturer's instructions. All primers used for site-directed mutagenesis are

listed in Table S1. OAS1 p46 C-terminal alanine mutants 1-8 were generated by ligation of mutant gBlocks (Table S1). Briefly, pcDNA3.1 FLAG-OAS1 p46 was cut with KflI and ApaI. Alanine mutant gBlocks were PCR-amplified using the following primer pair 5′-TAAGAATTGGGATGGGTCCCCAG-3′ and 5′-GACACTATAGAATAGGGCCCTCTAGA-3′ and then cut with with KflI and ApaI. Ligation was performed using T4 DNA ligase (Thermo Fisher Scientific) according to the manufacturer's instructions.

Geranylgeranyl click chemistry immunoprecipitation

Geranylgeranyl click chemistry IP reactions were performed using the Click-iT labeling kit and reagents (Thermo Fisher) according to the manufacturer's instructions with the following modifications. 293T OAS1 KO cells were incubated with 25 μM geranylgeranylalcohol azide (GGAA) and transfected with 250 ng/ml pCDNA3.1 FLAG-tagged OAS1 expression constructs 3h after addition of GGAA. 24h after transfection, cells were lysed in Co-IP (50 mM Tris-HCl, pH 7.5; 150 mM NaCl; 0.5% NP40; 1 mM EDTA) buffer and OAS1 proteins were immunoprecipitated from the lysate using 20 μg anti-FLAG antibody (Sigma) and Dynabeads Protein G. After 5 washes in Co-IP buffer, the Dynabeads were resuspended in 50 μl 50 mM Tris-HCl, pH 8, and the click chemistry reaction was performed according to the manufacturer's instruction. Immunoprecipitated protein were immunoblotted and probed for presence of geranylgeranyl azide-biotin labeling using an HRP-conjugated streptavidin antibody.

Virus infections and titer quantification

Encephalomyocarditis virus (ATCC VR-1762) was grown and titered in Vero cells. West Nile virus Texas was provided by the Gale laboratory and grown as previously described (*183*).

CVB3-Nancy was prepared as previously described (*25*)(kind gift from Raul Andino). Influenza virus A/PR/8/34 was purchased from ATCC. Influenza A virus A/Udorn/72 H3N2 R38A was provided by the Gale laboratory and prepared as described previously (29). For EMCV, WNV, CVB, and IAV infections, OAS1 KO 293T cells were seeded in 12 well plates coated with 10 μg/mL poly-L-ornithine hydrobromide (Sigma) and allowed to adhere overnight. Plasmids were then transfected using TransIT-X2 (Mirus Bio). At 24h post transfection, cells were infected with EMCV, WNV, or CVB at the indicated MOIs for 1h with gentle rocking. After 1h the inoculum was removed, and fresh media was added. For virus titer quantification, culture supernatants were serially diluted in DMEM using 96 well plates. For EMCV and WNV, titration was performed on Vero cells grown to 90% confluency in 6-well plates. For CVB, titration was performed on HeLa cells grown to 90% confluency in 6-well plates. IAV was titered on MDCK cells grown to 90% confluency in 12-well plates. The inoculum was removed after 1h of gentle rocking and a 0.8% agarose overlay was added containing the following: 0.8% UltraPure Low Melting Point Agarose (Thermo Fisher), 1x DMEM, 0.15% Sodium Bicarbonate, 10% heat-inactivated fetal bovine serum (FBS) (Atlanta Biologicals) and 1% penicillin-streptomycin-glutamine (Mediatech). For EMCV plates were fixed with 4% paraformaldehyde (Santa Cruz Biotechnology) at 24h post infection followed by staining with a 5% crystal violet solution prepared by dissolving crystal violet (Sigma Aldrich) in a 50/50 mixture of 100% ethanol and deionized water. For IAV plates were fixed with 4% paraformaldehyde (Santa Cruz Biotechnology) at 24h post infection followed by staining with a 5% crystal violet solution. For CVB plates were fixed with 4% paraformaldehyde (Santa Cruz Biotechnology) at 24h post infection followed by staining with a 5% crystal violet solution. For WNV a neutral red overlay containing 0.01% neutral red (Sigma-Aldrich) 0.8% UltraPure Low Melting Point Agarose

(Thermo Fisher), 1x DMEM, 0.15% sodium bicarbonate, 10% heat-inactivated fetal bovine serum (FBS) (Atlanta Biologicals) and 1% penicillin-streptomycin-glutamine (Mediatech) was added at 48h post infection and plaques were read 24h later.

SARS-CoV-2 strain USA/WA-1/2020 (gift of Dr. Michael Gale Jr.) was propagated and titered on VeroE6 cells (gift of Dr. Ralph Baric). For infections, 293T-ACE2 cells seeded in 24-well plates (100,000 cells/well) were transfected with 250ng of plasmid (Empty vector, p42, p46, and p46 ATIL) using the TransIT X2 kit (Mirus). A duplicate plate was transfected at the same time in order to confirm OAS1 expression by immunoblot. 24 hours post-transfection, cells were infected with SARS-CoV-2 at an MOI of 0.1 in serum free DMEM for 1 hr, and media was replenished with DMEM containing 4% serum. Supernatants were harvested at 48hpi, and serial dilutions were tittered on Vero E6 cells seeded at 90% confluency in 12-well plates. Inoculum was removed after 1 hr of gentle rocking and replenished with an agarose overlay containing 0.4% Noble Agar (Thermo Fisher) in DMEM containing 10% serum. At 72 hpi, plates were fixed with 10% formaldehyde and stained with crystal violet solution (0.1% crystal violet and 20% methanol in water).

Confocal laser scanning microscopy

For all microscopy experiments, cells were seeded on #1.5 12-mm coverslips (Bioscience Tools) coated with 10 μg/mL poly-L-ornithine hydrobromide (Sigma) and allowed to adhere overnight. For experiments testing endogenous OAS1 localization, cells were treated with IFNβ for 24h.

For experiments testing OAS1 localization in dox-inducible OAS1 A549 cells, cells were treated with 200 ng/mL doxycycline for 24h. For experiments testing localization of OAS1 in Huh7 cells, plasmids were transfected for 24h using Lipofectamine 3000 (Thermo Fisher) according to the manufacturer's instructions. At 24h post treatment/expression, cells were washed with PBS and then fixed in 4% PFA (Electron Microscopy Sciences) in PBS for 10 min at room temperature, washed with PBS, and then permeabilized with PBS containing 0.1% Triton X-100 for 10 minutes at room temperature. Cells were washed with PBS and then resuspended in a 3% BSA/PBS blocking solution for 1 hour. After blocking, cells were stained with rabbit anti-OAS1 (CST) and mouse IgG1 anti-Golgin 97 (CST) in PBS containing 1% BSA and 0.3% Triton X-100 for 1 hour in the dark at room temperature (Table S2). Cells were washed three times with PBS and then stained with the secondary antibodies goat anti-rabbit IgG Alexa Fluor 488 (Themo Fisher) and goat anti-mouse IgG Alexa Fluor 648 (Thermo Fisher) in PBS containing 1% BSA and 0.3% Triton X-100 for 1 hour in the dark at room temperature (Table S2). Samples were washed once with PBS, stained with DAPI in PBS for 10 minutes in the dark, followed by washing three times with PBS and then mounted with ProLong Glass antifade mounting media (Thermo Fisher). Samples were cured in the dark at room temperature for 24-48h prior to imaging.

For experiments testing OAS1 localization during viral infections, OAS1 was expressed as described above. At 24h post transfection, cells were infected with the indicated virus for 1h with gentle rocking followed by removal of the inoculum and replacement with fresh media. At 24h post treatment/expression, cells were washed with PBS and then fixed in 4% PFA (Electron Microscopy Sciences) in PBS for 10 min at room temperature, washed with PBS, and then

permeabilized with PBS containing 0.1% Triton X-100 for 10 minutes at room temperature. Cells were washed with PBS and then resuspended in a 3% BSA/PBS blocking solution for 1 hour. After blocking, cells infected with EMCV were stained with rabbit anti-OAS1 (CST) and mouse IgG1 anti-dsRNA 9D5 (Adam Geballe, Fred Hutchinson Cancer Research Center, WA) in PBS containing 1% BSA and 0.3% Triton X-100 for 1 hour in the dark at room temperature. Cells infected with WNV were stained with rabbit anti-OAS1 (CST), mouse IgG1 anti Golgin 97 (CST) or mouse anti IgG1 PDIA3 (Sigma-Aldrich) and mouse IgG2a anti-dsRNA J2 (Scicons) in PBS containing 1% BSA and 0.3% Triton X-100 for 1 hour in the dark at room temperature (Table S2). EMCV infected cells were washed three times with PBS and then stained with the secondary antibodies goat anti-rabbit IgG Alexa Fluor 488 (Themo Fisher) and goat anti-mouse IgG Alexa Fluor 648 (Thermo Fisher) in PBS containing 1% BSA and 0.3% Triton X-100 for 1 hour in the dark at room temperature. WNV infected cells were washed three times with PBS and then stained with the secondary antibodies goat anti-rabbit IgG Alexa Fluor 488 (Themo Fisher), goat anti-mouse IgG1 (Thermo Fisher) and goat anti-mouse IgG2a Alexa Fluor 648 (Thermo Fisher) in PBS containing 1% BSA and 0.3% Triton X-100 for 1 hour in the dark at room temperature (Table S2). Samples were washed once with PBS, stained with DAPI in PBS for 10 minutes in the dark, followed by washing three times with PBS and then mounted with ProLong Glass antifade mounting media (Thermo Fisher). Samples were cured in the dark at room temperature for 24-48h prior to imaging. Samples were imaged using a Nikon Eclipse Ti laser scanning confocal microscope using a 60x oil-immersion lens. Images were processed and analyzed using the NIS elements software and Fiji. Quantification of colocalization was performed using the Fiji Coloc 2 plugin.

RNA isolation, reverse transcription, and qPCR

Total RNA was isolated using the NucleoSpin RNA kit (Macherey-Nagel) according to the manufacturer's protocol. cDNA was synthesized from 1 μg total RNA using the QuantiTect RT kit (Qiagen) according to the manufacturer's instructions. qPCR was carried out using the ViiA7 qPCR system with TaqMan reagents using TaqMan primers/probes (Life Technologies) for EMCV 5′UTR (Table S1).

RNA immunoprecipitation

OAS1 KO Huh7 cells were seeded the day before transfection with FLAG-p42, FLAG-p42CTIL, FLAG-p46, FLAG-p46ATIL or an EV control using TransIT-X2 (Mirus Bio). At 24h post transfection, cells were infected with EMCV at an MOI of 0.001. At 12h post infection, cells were harvested and lysed in RNA-IP lysis buffer (100 mM KCl, 5 mM MgCl2, 10 mM HEPES pH 7.4, 0.5% NP-40, 1 mM DTT, 1× HALT protease inhibitor, 100 U/ml RNasin and 2 mM ribonucleoside-vanadyl complex). Nuclei and debris were removed from the cytosolic lysate by centrifugation at 8,000 g at 4 °C for 10 min. Next, 400 μg protein from the cytosolic lysate was incubated with 5 μg anti-FLAG mouse IgG1 (M2, Sigma) or mouse IgG1 control overnight at 4 °C, with rotation. The next day, 0.75 mg Dynabeads Protein G (Invitrogen) was added and the lysate was incubated for 2h at 4 °C with rotation. After washing, coprecipitated RNA was isolated from IgG1-protein complexes by chloroform-isoamyl alcohol extraction, reverse transcribed into cDNA (QuantiTect RT kit, Qiagen) and analyzed by qPCR.

Genetic association

Samples from a cohort of 35 severe COVID-19 cases were collected starting in April 2020 at Virginia Mason Medical Center and Benaroya Research Institute. Severity was based on hospitalization in the critical care unit with mechanical ventilation. A cohort of 99 healthy control subjects matched for ancestry was assembled from participants in the healthy control registry at Benaroya Research Institute. The study was approved by the Institutional Review Board at Benaroya Research Institute. A description of the cohorts is presented in Table S3. DNA samples from these subjects were genotyped for OAS1 rs10774671 using a Taqman SNP genotyping assay (Thermo Fisher). Genotypes passed Hardy Weinberg equilibrium analysis. Association testing was performed using gPLINK v2.050 by logistic regression adjusting for sex and ancestry (race/ethnicity).

Statistics

Statistical analyses were performed with Prism 8 and the specific statistical analyses performed are indicated in the figure legends.

Model generation

BioRender software was used to prepare schematics used in the manuscript.

3.5 Acknowledgements

This project was funded by National Institutes of Health grants (nos. AI145974, AI108765, AI135437 to R.S.; AI104002, AI118916, AI145296, AI127463, AI100625 to MG); T32 and F31 training grants (nos. AI106677, GM007270, and AI140530 to F.W.S.; T32 HL007312 to AFR); a Postdoctoral Research Fellowship from the German Research Foundation (no. SCHW 1881/1-1 to J.S.); JMC received support from the Cancer Research Institute

Irvington Fellowship Program. We thank the BRI COVID-19 Research Team for collective the samples for genetic analysis. We thank M. A. Davis (UW Immunology) for help with confocal laser scanning microscopy.

3.6 Figures

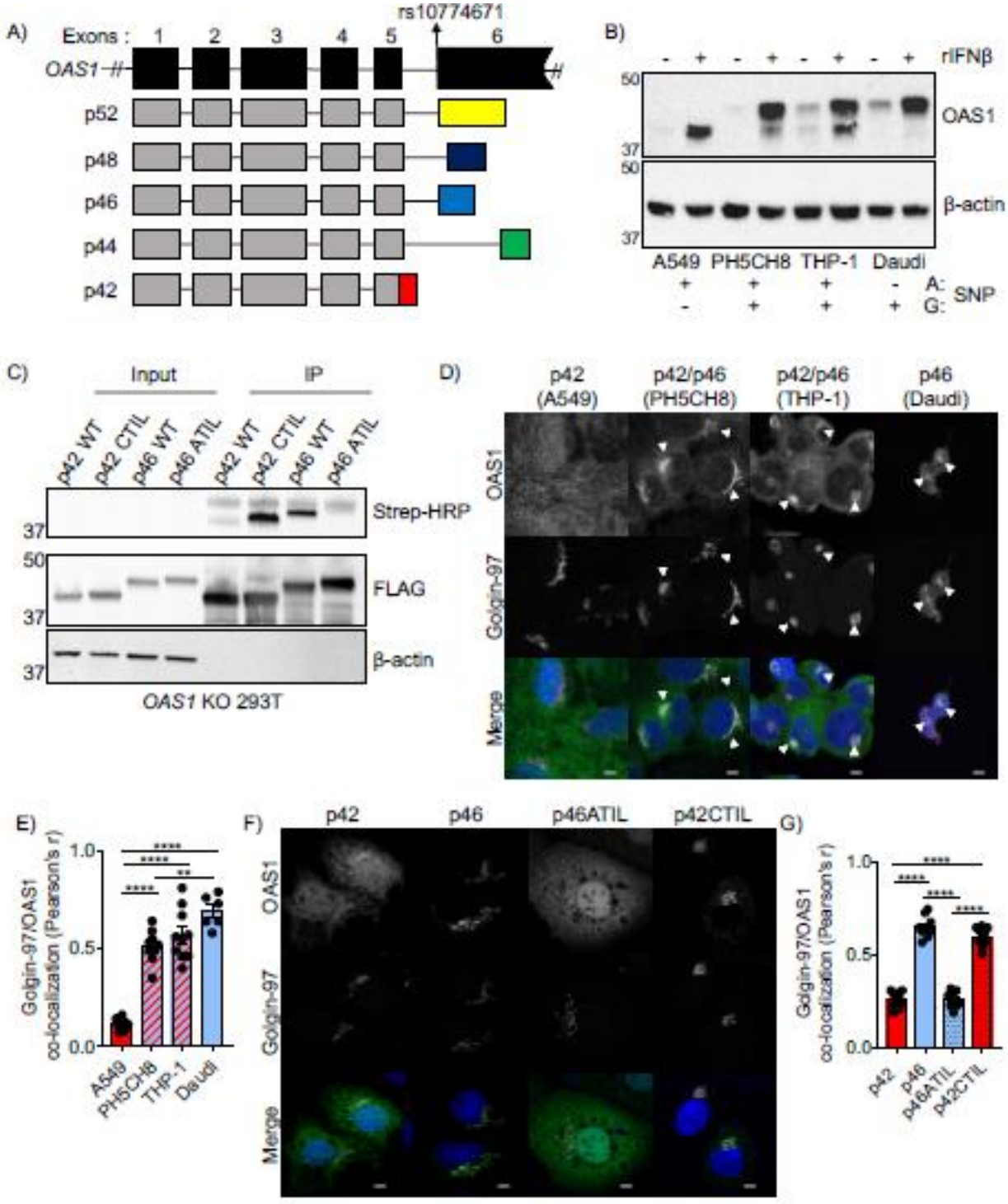
A)
Exons : 1 2 3 4 5 6
rs10774671
OAS1
p52
p48
p46
p44
p42
B)
rIFNβ
OAS1
β-actin
A549 PH5CH8 THP-1 Daudi
SNP
A:
G:
C)
Input
IP
p42 WT
p42 CTIL
p46 WT
p46 ATIL
Strep-HRP
FLAG
β-actin
OAS1 KO 293T
D)
p42 (A549)
p42/p46 (PH5CH8)
p42/p46 (THP-1)
p46 (Daudi)
OAS1
Golgin-97
Merge
E)
Golgin-97/OAS1 co-localization (Pearson's r)
A549
PH5CH8
THP-1
Daudi
F)
p42
p46
p46ATIL
p42CTIL
G)
p42
p46
p46ATIL
p42CTIL

Figure 3.1. The p46 isoform of OAS1 is targeted to the endomembrane system.

A) Differential C-terminal splicing of OAS1 creates isoform diversity. **B)** Immunoblot analysis of OAS1 isoform expression across cell lines treated with 1000U/mL IFNβ for 24h. **C)** Immunoblot of whole cell lysate (left) and immunoprecipitated (right) FLAG-tagged p42, p46, p42CTIL, or p46ATIL constructs subjected to Click-chemistry reaction with geranylgeranyl azide and alkyne biotin. **D)** Representative maximum intensity projections of the indicated cell lines treated with IFNβ for 24h followed by staining with anti-OAS1 antibody (green), anti-Golgin-97 (magenta), and DAPI (blue). **E)** Pearson's correlation of OAS1 and Golgin-97 in individual cells from the indicated cell lines. **F)** Representative confocal slices of OAS1 KO Huh7 transfected with constructs encoding p42, p46, p42CTIL, or p46ATIL stained with anti-OAS1 and Golgin-97 antibodies (green, magenta) and DAPI (blue). **G)** Pearson's correlation of OAS1 and Golgin-97 in *OAS1 KO* Huh7 cells expressing p42, p46, p42CTIL, or p46ATIL. Scale on micrographs in D) and F) = 5 μm. E), G) Data were analyzed using one-way ANOVA with Tukey's multiple comparisons test where **P<0.01, ****P<0001.

A)

```
p42  MMDLRNTPAKSLDKFIEDYLLPDTCFRMQINHAIDIICGFLKERCFRGSSYPVCVSKVVKGGSSGKGTTLRGRSDADLVVFLSPLTTFQDQLNRRGEFIQEIRRQLEACQ 110
p44  ..........................................................................................................  110
p46  ..........................................................................................................  110
p48  ..........................................................................................................  110
p52  ..........................................................................................................  110

p42  RERAFSVKFEVQAPRWGNPRALSFVLSSLQLGEGVEFDVLPAFDALGQLTGGYKPNPQIYVKLIEECTDLQKEGEFSTCFTELQRDFLKQRPTKLKSLIRLVKHWYQNCK 220
p44  ..........................................................................................................  220
p46  ..........................................................................................................  220
p48  ..........................................................................................................  220
p52  ..........................................................................................................  220

p42  KKLGKLPPQYALELLTVYAWERGSMKTHFNTAQGFRTVLELVINYQQLCIYWTKYYDFKNPIIEKYLRRQLTKPRPVILDPADPTGNLGGGDPKGWRQLAQEAEAWLNYP 330
p44  ..........................................................................................................  330
p46  ..........................................................................................................  330
p48  ..........................................................................................................  330
p52  ..........................................................................................................  330

p42  CFKNWDGSPVSSWILLVRPPASSLPFIPAPLHEA                                                                          364
p44  ..............NLTLVGRRNYTNN                                                                                  360
p46  ..............AESNSADDETDDPRRYQKYGYIGTHEYPHFSHRPSTLQAASTPQAEEDWTCTIL                                          400
p48  ..............TQHTPG.IHPTGRRGLDLHHPLNASASWGKGLQCYLDQFLHFQVGLLIQRGQSSSVSWCIIQDRTQVS                              414
p52  ..............LKATVQTMRPTIPGRIRNMVTLEHMSTLISLIDPAHSRQHPPHRQKRTGPAPSSECQCILGERAPVLSGPVPSFSGGTLDPEKTKLLSELVYNP 440

p52  GQNPGLLTPGLLCPLSYHR 457
```

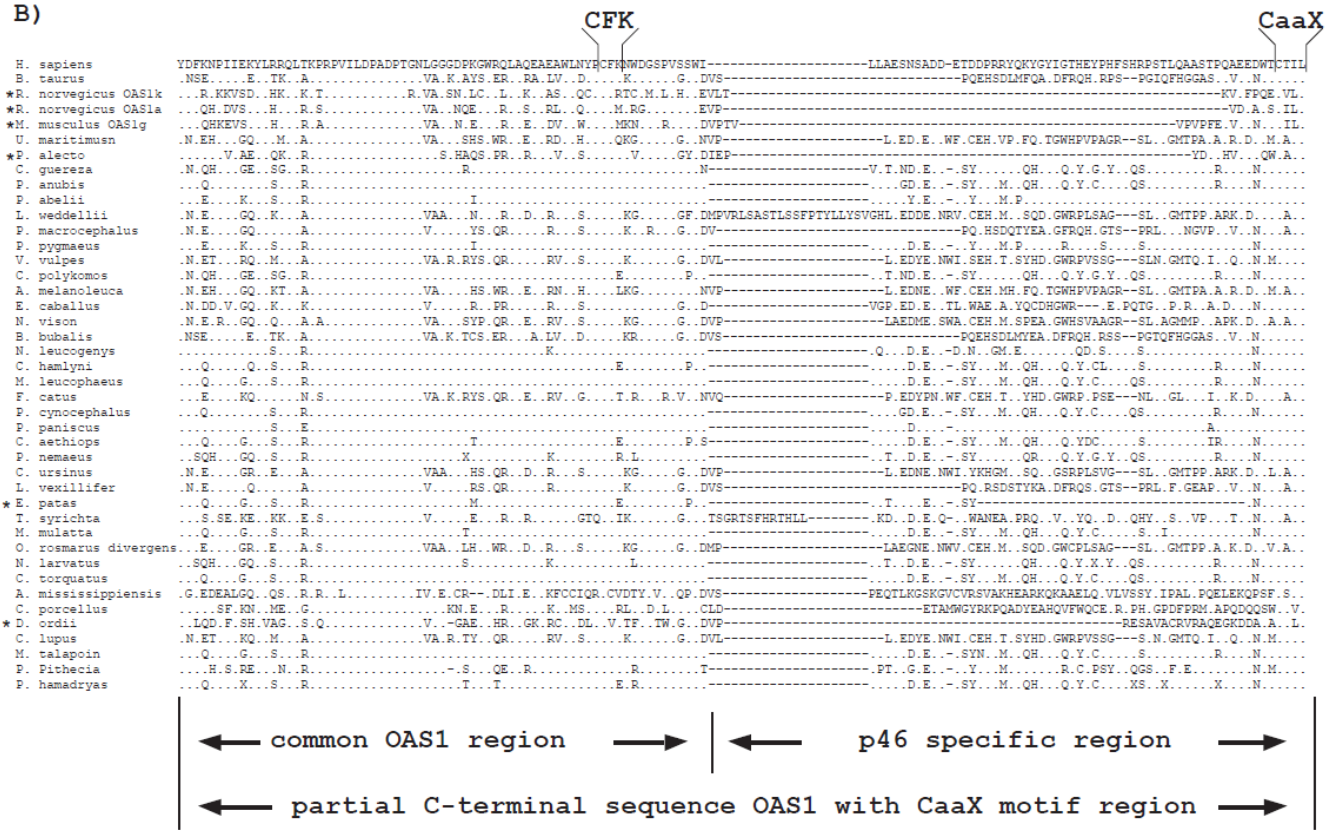
B)
CFK
CaaX
common OAS1 region
p46 specific region
partial C-terminal sequence OAS1 with CaaX motif region

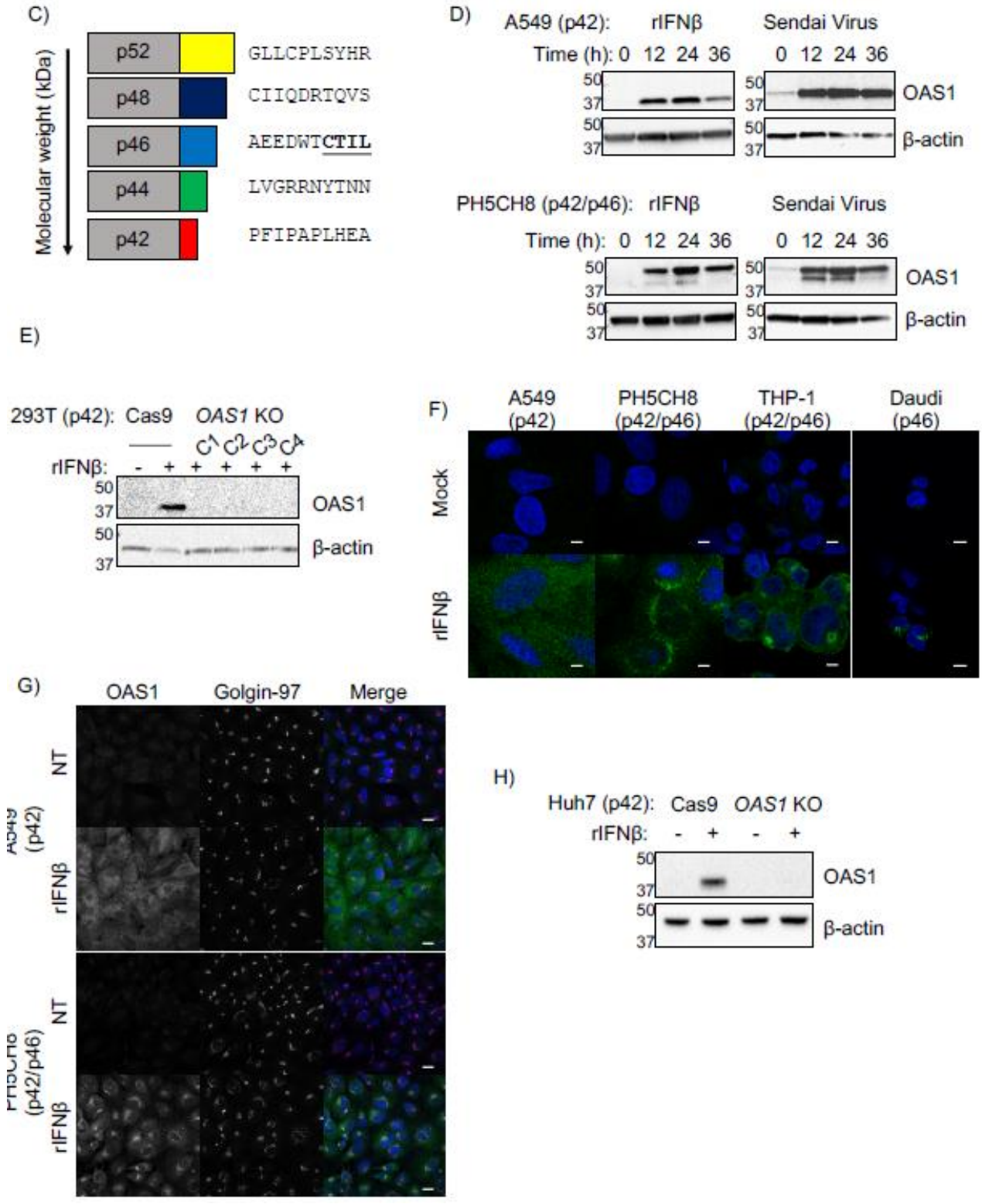
C)
Molecular weight (kDa)
p52
p48
p46
p44
p42
GLLCPLSYHR
CIIQDRTQVS
AEEDWTCTIL
LVGRRNYTNN
PFIPAPLHEA
D)
A549 (p42): rIFNβ Sendai Virus
Time (h): 0 12 24 36 0 12 24 36
50
37
OAS1
β-actin
PH5CH8 (p42/p46): rIFNβ Sendai Virus
Time (h): 0 12 24 36 0 12 24 36
E)
293T (p42): Cas9 OAS1 KO
C1 C2 C3 C4
rIFNβ: - + + + + +
F)
A549 (p42)
PH5CH8 (p42/p46)
THP-1 (p42/p46)
Daudi (p46)
Mock
rIFNβ
G)
OAS1
Golgin-97
Merge
NT
rIFNβ
A549 (p42)
PH5CH8 (p42/p46)
H)
Huh7 (p42): Cas9 OAS1 KO
rIFNβ: - + - +


I)
A549 (p42): Cas9
OAS1 KO
C1
C5
C10
C12
50
37
OAS1
50
37
β-actin

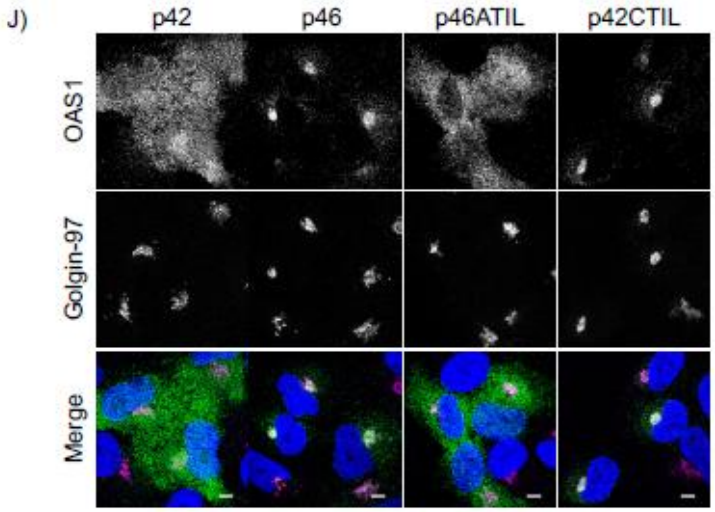
J)
p42
p46
p46ATIL
p42CTIL
OAS1
Golgin-97
Merge

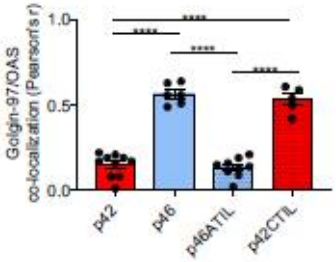
K)
Golgin-97/OAS co-localization (Pearson's r)
1.0
0.5
0.0
****
****
****
****
p42
p46
p46ATIL
p42CTIL

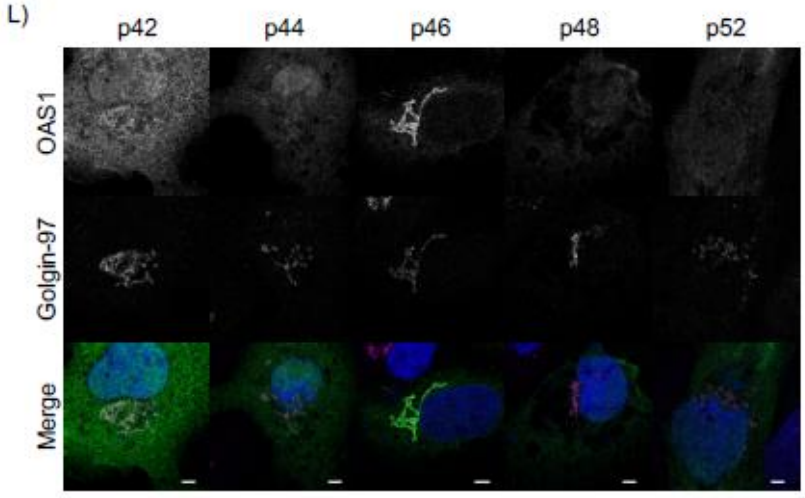
L)
p42
p44
p46
p48
p52
OAS1
Golgin-97
Merge

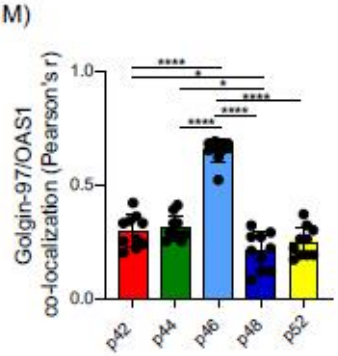
M)
Golgin-97/OAS1 co-localization (Pearson's r)
1.0
0.5
0.0
****
*
*
****
****
****
p42
p44
p46
p48
p52

Supplementary Figure 3.1 (related to figure 3.1).

A) Sequence alignment of human OAS1 isoforms. **B)** Sequence alignment of OAS1 p46 orthologous isoforms from different species. *Homo sapiens* P00973; *Bos taurus* F1MV66; *Rattus norvegicus* A0A0G2JU81; *Rattus norvegicus* Q05961; *Mus musculus* Q8K469; *Ursus maritimus* A0A384BY08*; Pteropus alecto* L5KWW0; *Colobus guereza* A0A3S7SJJ2; *Papio anubis* A0A3Q8HNT1*; Pongo abelii* B6RC73; *Leptonychotes weddellii* A0A2U3Y7T9; *Physeter macrocephalus* A0A2Y9EML2; *Pongo pygmaeus* A0A3Q8HG13; *Vulpes vulpes* A0A3Q7TBS2*; Colobus polykomos* A0A1B1M0U9; *Ailuropoda melanoleuca* G1LPZ0; *Equus caballus* A0A3Q2L9T1; *Neovison vison* U6CVG6; *Bubalus bubalis* A0A2S1PHI8; *Nomascus leucogenys* A0A2I3H3E5; *Cercopithecus hamlyni* A0A1B1M0T4; *Mandrillus leucophaeus* A0A1B1M0W1; *Felis catus* M3VUI8; *Papio cynocephalus* A0A1B1M0W8; *Pan paniscus* B6RC68*; Chlorocebus aethiops* A0A3Q8HG02; *Pygathrix nemaeus* A0A1B1M0V1; *Callorhinus ursinus* A0A3Q7QFP7; *Lipotes vexillifer* A0A340Y9X3; *Erythrocebus patas* A0A1B1M0V2; *Tarsius syrichta* A0A1U7TU37; *Macaca mulatta* A4LAA0; *Odobenus rosmarus divergens* A0A2U3WN15; *Nasalis larvatus* A0A1B1M0T6; *Cercocebus torquatus* A0A1B1M0U1; *Alligator mississippiensis* A0A151NE69*; Cavia porcellus* A0A286X8S4; *Dipodomys ordii* A0A1S3FQL6; *Canis lupus familiaris* F1PLW6; *Miopithecus talapoin* A0A3S7SJS6; *Pithecia pithecia* A0A3Q8HGF7; *Papio hamadryas* A0A1B1M0W2. **C)** OAS1 isoforms with last 10 amino acids. **D)** Immunoblot analysis of OAS1 expression in A549 and PH5CH8 cells following treatment with IFNβ (1000 U/mL) or Sendai virus (100 HAU/mL) for the indicated times. **E)** Immunoblot analysis of OAS1 expression in Cas9 and clonal *OAS1* KO 293T cells treated with IFNβ (1000 U/mL) for 24h. **F)** Representative confocal slices of the indicated cell lines treated with IFNβ (1000 U/mL) for 24h followed by staining with antibodies against OAS1 (green) and DAPI dye (blue). **G)** Representative maximum intensity projections

from the indicated cell lines treated with IFNβ for 24h followed by staining with anti-OAS1 antibody (green), anti-Golgin-97 (magenta), and DAPI (blue). **H)** Immunoblot analysis of OAS1 expression in Cas9 and polyclonal *OAS1* KO Huh7 cells treated with IFNβ (1000 U/mL) for 24h. **I)** Immunoblot analysis of OAS1 expression in Cas9 and clonal OAS1 KO A549 cells treated with IFNβ (1000 U/mL) for 24h. **J)** Representative confocal slices of OAS1 KO A549 cells expressing dox-inducible p42, p46, p42CTIL, or p46ATIL stained with anti-OAS1 and Golgin-97 antibodies (green, magenta) and DAPI (blue). **K)** Pearson's correlation of OAS1 and Golgin-97 in OAS1 KO A549 cells expressing p42, p46, p42CTIL, or p46ATIL. **L)** Representative confocal slices of OAS1 KO Huh7 cells expressing p42, p44 p46, p48 or p52 stained with anti-OAS1 and Golgin-97 antibodies (green, magenta) and DAPI (blue). **M)** Pearson's correlation of OAS1 and Golgin-97 in *OAS1* KO Huh7 cells expressing p42, p44 p46, p48 or p52. Scale = 5 μm. E) and G) Data were analyzed using one-way ANOVA with Tukey's multiple comparisons test where *P<0.05 and ****P<0.0001.

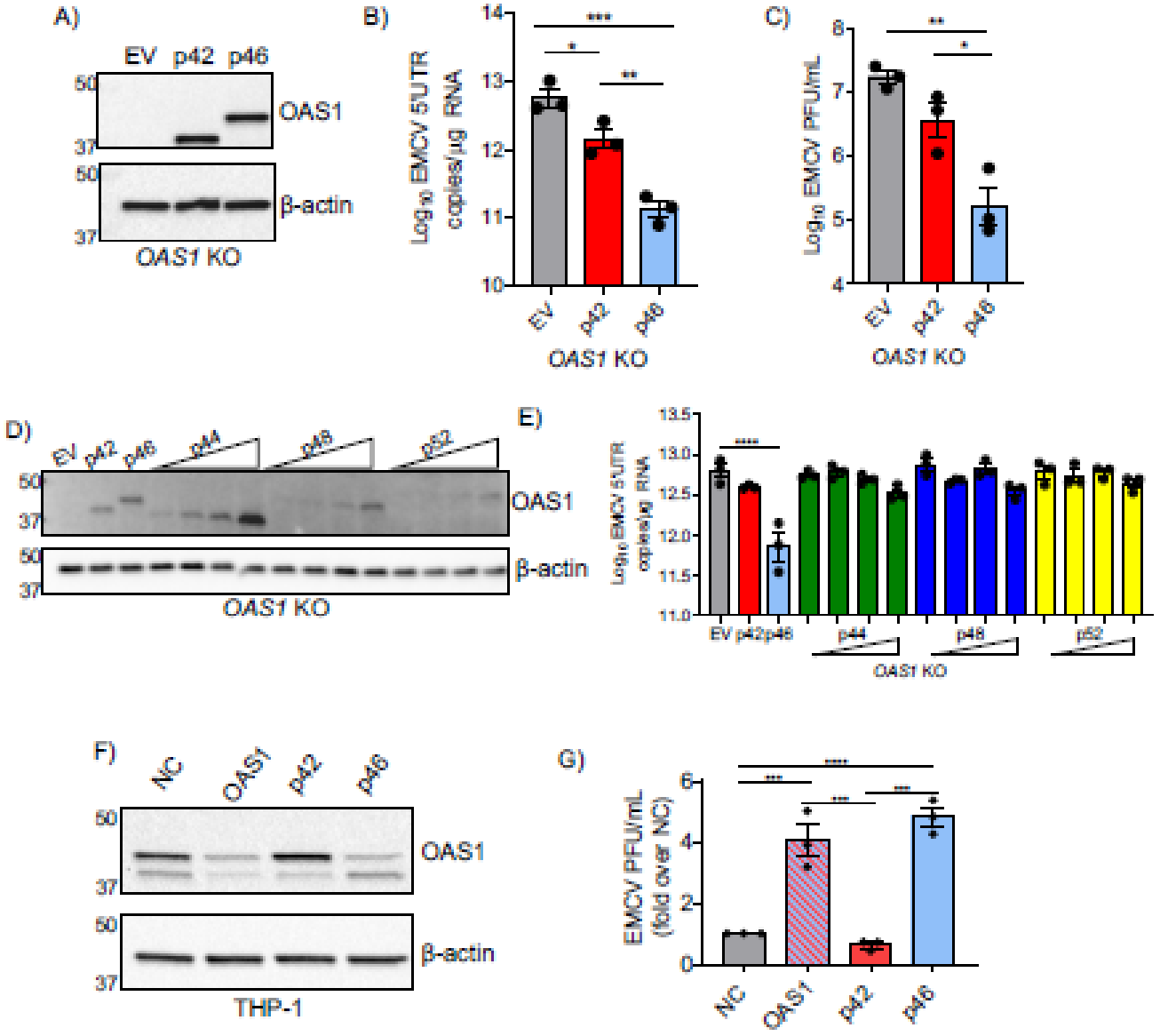

Figure 3.2. OAS1 isoforms are differentially antiviral.

A) Immunoblot analysis of p42 and p46 in OAS1 KO 293T cells at 24h post transfection. B) Quantification of EMCV 5′UTR by qPCR from OAS1 KO 293T cells transfected with a control EV, p42, or p46 at 24h post infection with EMCV at an MOI of 0.001. C) Viral titers at 24h post infection with EMCV at an MOI of 0.001 in OAS1 KO 293T cells transfected with a control EV, p42, and p46. D) Immunoblot analysis of OAS1 expression in OAS1 KO 293T at 24h post

transfection with EV (500 ng), p42 (100 ng), p46 (100 ng), or 200, 350, or 500 ng of the corresponding catalytic mutant (500 ng DNA total in each transfection). E) Quantification of EMCV 5′UTR in OAS1 KO 293T transfected as in A) for 24h followed by infection with EMCV for 24h (MOI 0.001). F) Immunoblot of OAS1 in PMA-differentiated THP-1 macrophages infected with EMCV at an MOI of 1 for 24h after 24h post transfection with a non-targeting control siRNA (siNC) or siRNAs against OAS1, p42, or p46. G) Viral titers at 24h post infection with EMCV at an MOI of 1 taken from PMA-differentiated THP-1 macrophages transfected with siNC, siOAS, sip42, or sip46. B), C), and G) Data were analyzed using one-way ANOVA with Tukey's multiple comparisons test where *P<0.05, **P<0.01, ***P<0.001, ****P<0.0001. For E) data were analyzed using a one-way ANOVA with Dunnett's multiple comparisons test (vs. EV) where ****p<0.0001.

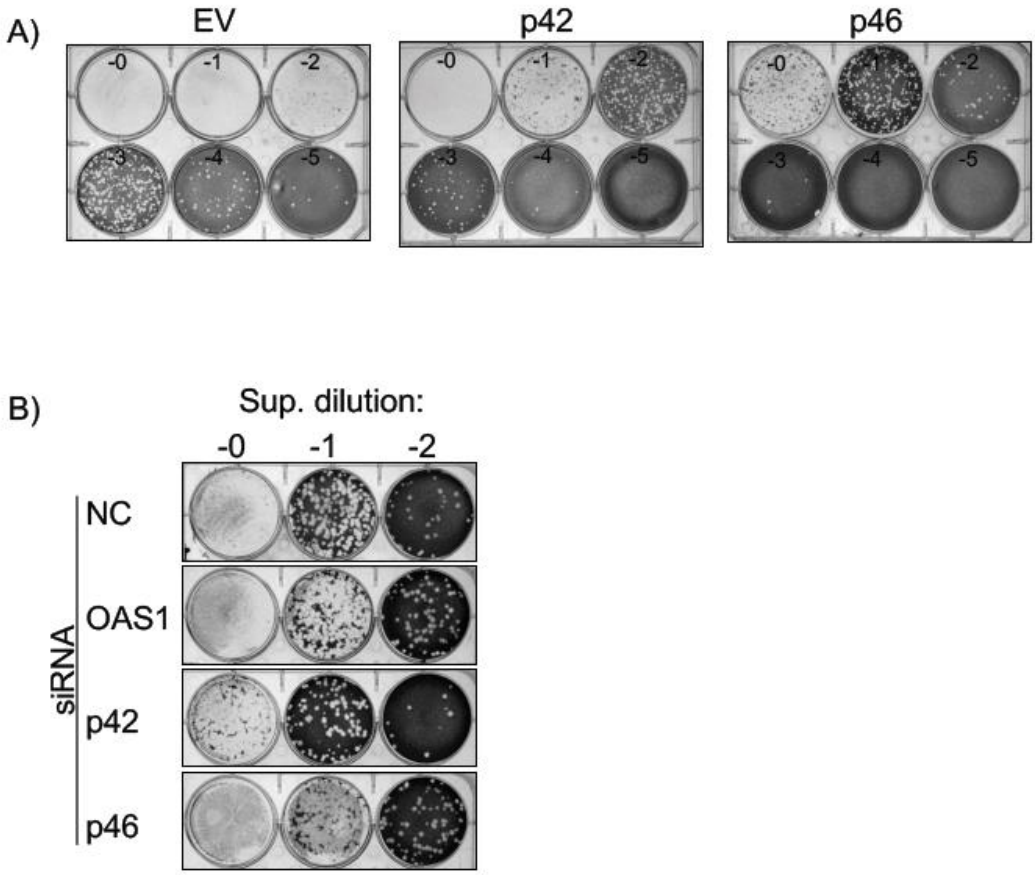

Supplementary Figure 3.2 (related to figure 3.2).

A) Representative plaque assay plates from the data in shown in Fig. 2C. **B)** Representative plaque assay plates from data shown in Fig. 2G.

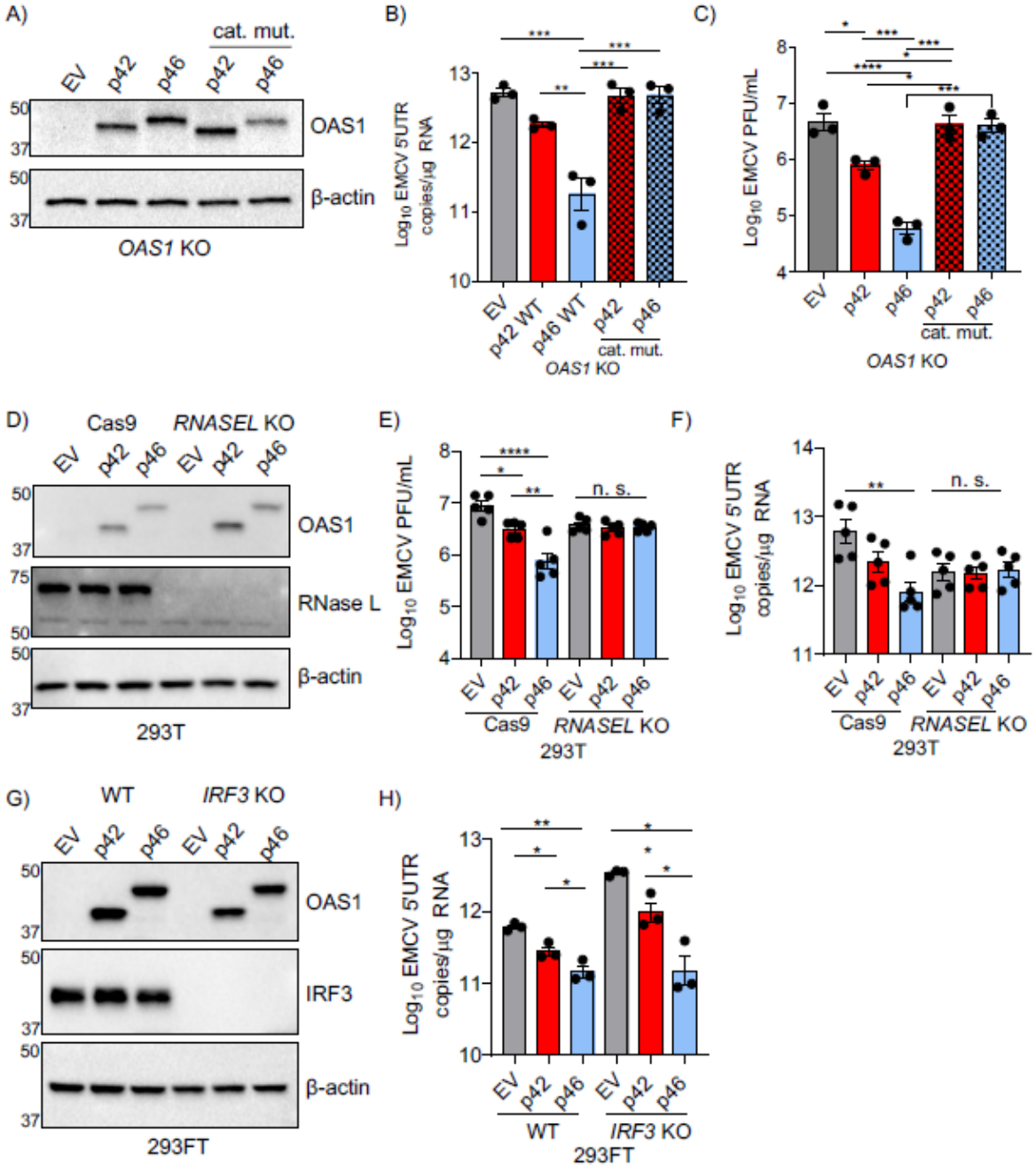

Figure 3.3. OAS1 isoforms require catalytic and RNase L activity.

A) Expression of OAS1 p42 and p46 along with their corresponding catalytic mutants (250ng) at 24h post transfection in OAS1 KO 293T cells. **B)** Quantification of EMCV 5′UTR by qPCR from OAS1 KO 293T cells transfected with a control EV, p42, p46, or their corresponding

catalytic mutants (250ng) at 24h post infection with EMCV at an MOI 0.001. **C)** Viral titers at 24h post infection with EMCV at an MOI of 0.001 taken from OAS1 KO 293T cells transfected with a control EV, p42, p46, or their corresponding catalytic (DADA) mutants. **D)** Immunoblot analysis of OAS1 and RNase L at 24h post transfection in Cas9 or RNase L KO 293T cells. **E)** Quantification of EMCV 5′UTR by qPCR from Cas9 and RNase L KO 293T cells transfected with control EV, p42, or p46 at 24h post infection with EMCV at an MOI of 0.001. **F)** Viral titers at 24h post infection with EMCV at an MOI of 0.001 taken from Cas9 or RNase L KO 293T cells transfected with control EV, p42, or p46. **G)** Immunoblot analysis of OAS1 and IRF3 in WT or IRF3 KO 293FT cells at 24h post transfection. **H)** Quantification of EMCV 5′UTR 24h post infection with EMCV at an MOI of 0.001 in WT or IRF3 KO 293FT cells transfected with a control EV, p42, or p46. EMCV plaque assays quantified on Vero cells. B), C), E), F), H) Data were analyzed using one-way ANOVA with Tukey's multiple comparisons test where *P<0.05, **P<0.01, ***P<0.001, ****P<0.0001.

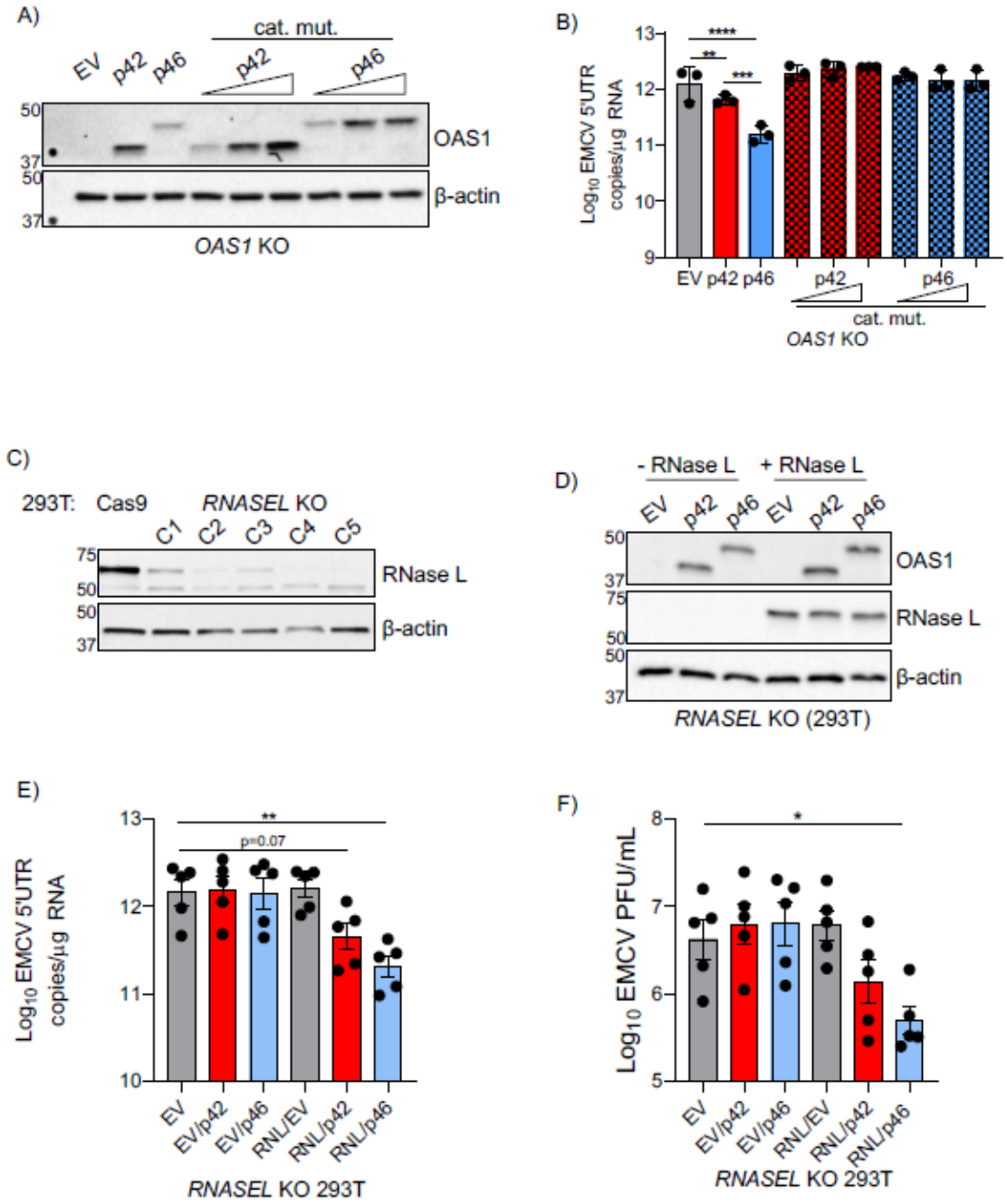

Supplementary Figure 3.3 (related to figure 3.3).

A) Expression of OAS1 p42 and p46 along with their corresponding catalytic mutants at 24h post transfection in OAS1 KO 293T cells. **B)** Quantification of EMCV 5′UTR by qPCR from OAS1 KO 293T cells transfected with a control EV, p42, p46, or their corresponding catalytic

mutants at 24h post infection with EMCV at an MOI 0.001. **C)** Immunoblot analysis of RNase L expression in Cas9 and clonal RNase L KO 293T cells. Clone 5 was used for subsequent experiments. **D)** Immunoblot analysis of OAS1 and RNase L expression in RNase L KO 293T cells at 24h post transfection with EV, p42, p46 with or without an RNase L expression plasmid. **E)** Quantification of EMCV 5′UTR or **F)** EMCV titers from RNase L KO 293T cells transfected as in D) followed by infection with EMCV for 24h (MOI 0.001). E) and F) Data were analyzed using a one-way ANOVA with Dunnett's multiple comparisons test where *$p<0.05$, **$p<0.01$, ***$p<0.001$, ****$p<0.0001$.

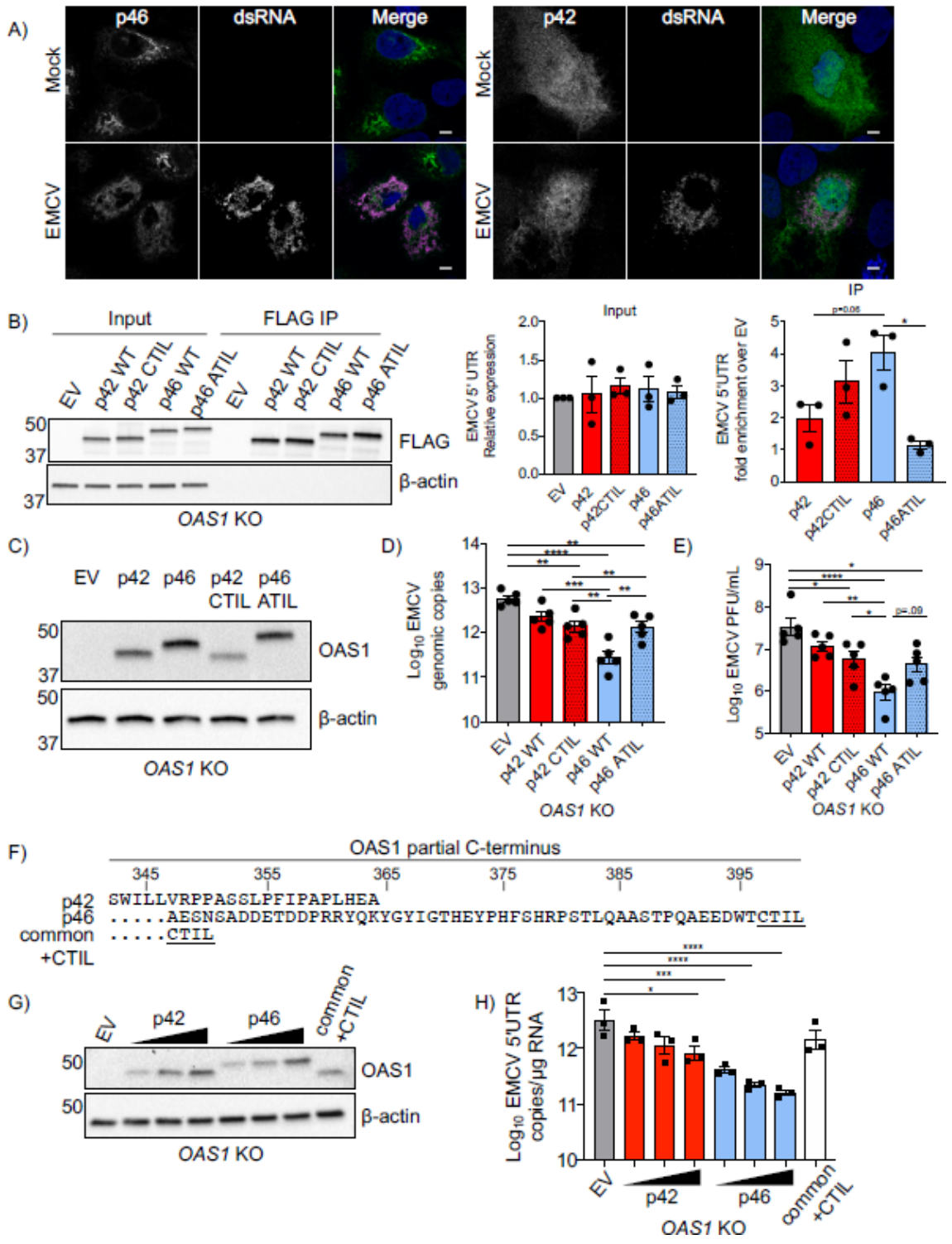

Figure 3.4. Endomembrane targeting of OAS1 p46 through the CaaX motif enhances access to viral RNA.

A) Representative confocal micrographs from mock or EMCV infected (MOI=0.001, 12h) OAS1 KO Huh7 cells expressing p42 or p46 and stained with anti-OAS1 and dsRNA (green, magenta) and DAPI (blue). B) Representative immunoblot of FLAG immunoprecipitation performed on OAS1 KO Huh7 cells expressing control EV, FLAG-p42, FLAG-p42CTIL, FLAG-p46, and FLAG-p46ATIL. Quantification of EMCV 5′UTR via qPCR in the input or after RNA immunoprecipitation performed on OAS1 KO Huh7 cells transfected with control EV, FLAG-p42, FLAG-p42CTIL, FLAG-p46, and FLAG-p46ATIL infected with EMCV at an MOI of 0.001 for 12h. C) Immunoblot analysis of p42, p46, p42CTIL, and p46ATIL in OAS1 KO 293T cells at 24h post transfection. D) Quantification of EMCV 5′UTR by qPCR from OAS1 KO 293T cells transfected with a control EV, p42, p46, p42CTIL or p46ATIL at 24h post infection with EMCV at an MOI 0.001. E) Viral titers quantified at 24h post infection with EMCV at an MOI of 0.001 in OAS1 KO 293T cells expressing transfected with control EV, p42, p46, p42CTIL or p46ATIL. F) Alignment of constructs used in G) and H). G) Immunoblot analysis of p42 (50 ng, 100 ng, 200 ng) p46 (50 ng, 100 ng, 200 ng) and common +CTIL (500 ng) in OAS1 KO 293T cells at 24h post transfection. H) Quantification of EMCV 5′UTR by qPCR from OAS1 KO 293T cells transfected as in G) at 24h post infection with EMCV at an MOI 0.001. EMCV plaque assays quantified on Vero cells. B), D), and E) Data were analyzed using one-way ANOVA with Tukey's multiple comparisons test where *P<0.05, **P<0.01, ***P<0.001, ****P<000.1. Scale = 5 μm. H) Data were analyzed using a one-way ANOVA with Dunnett's multiple comparisons test (vs. EV) where *P<0.05, ***P<0.001, and ****P<0.0001

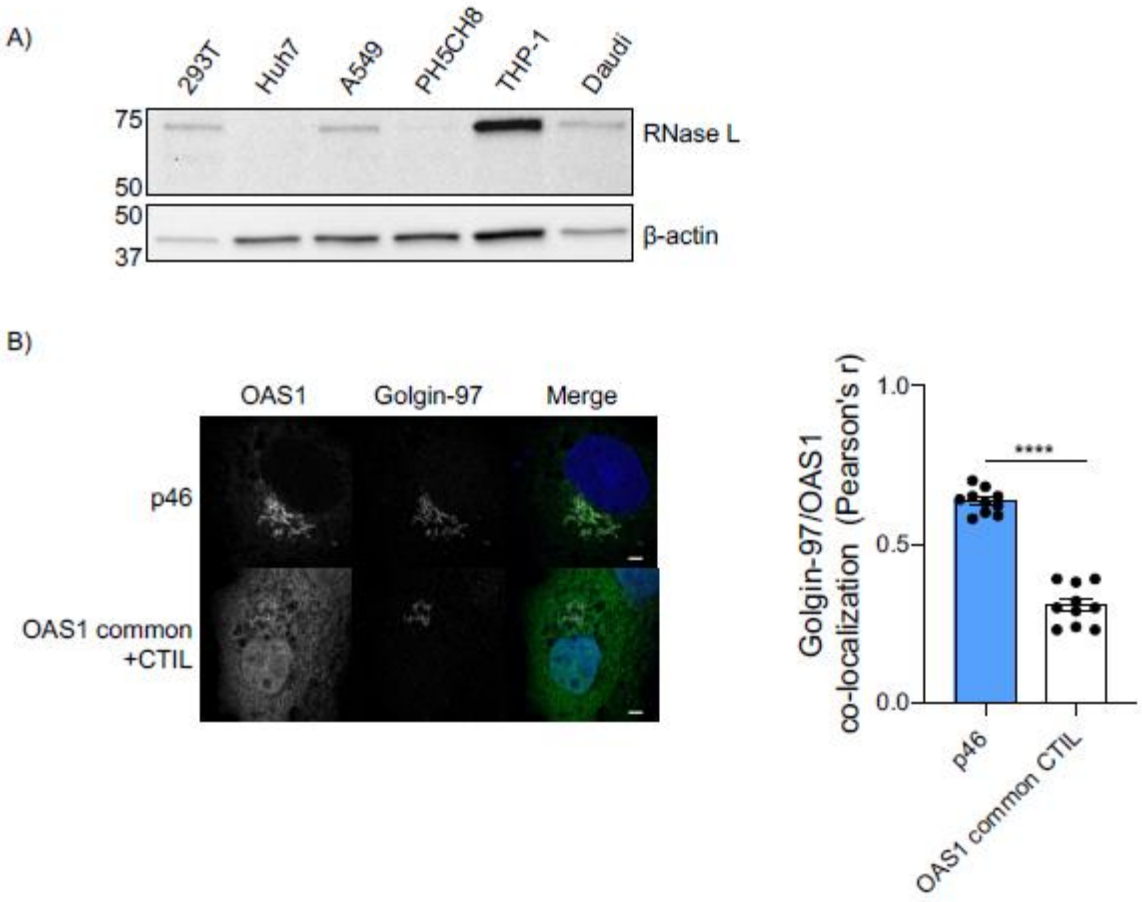

Supplementary Figure 3.4 (related to figure 3.4).

A) Immunoblot of RNase L expression in untreated cell lines. **B)** Representative confocal slices of OAS1 KO Huh7 cells expressing OAS1 p46 and OAS1 common +CTIL stained with anti-OAS1 (green) and Golgin-97 (magenta) antibodies and DAPI (blue). **C)** OAS1 and Golgin-97 colocalization is shown as Pearson's correlation. Scale = 5µm. Data were analyzed using an unpaired t test where ****P<0.0001.

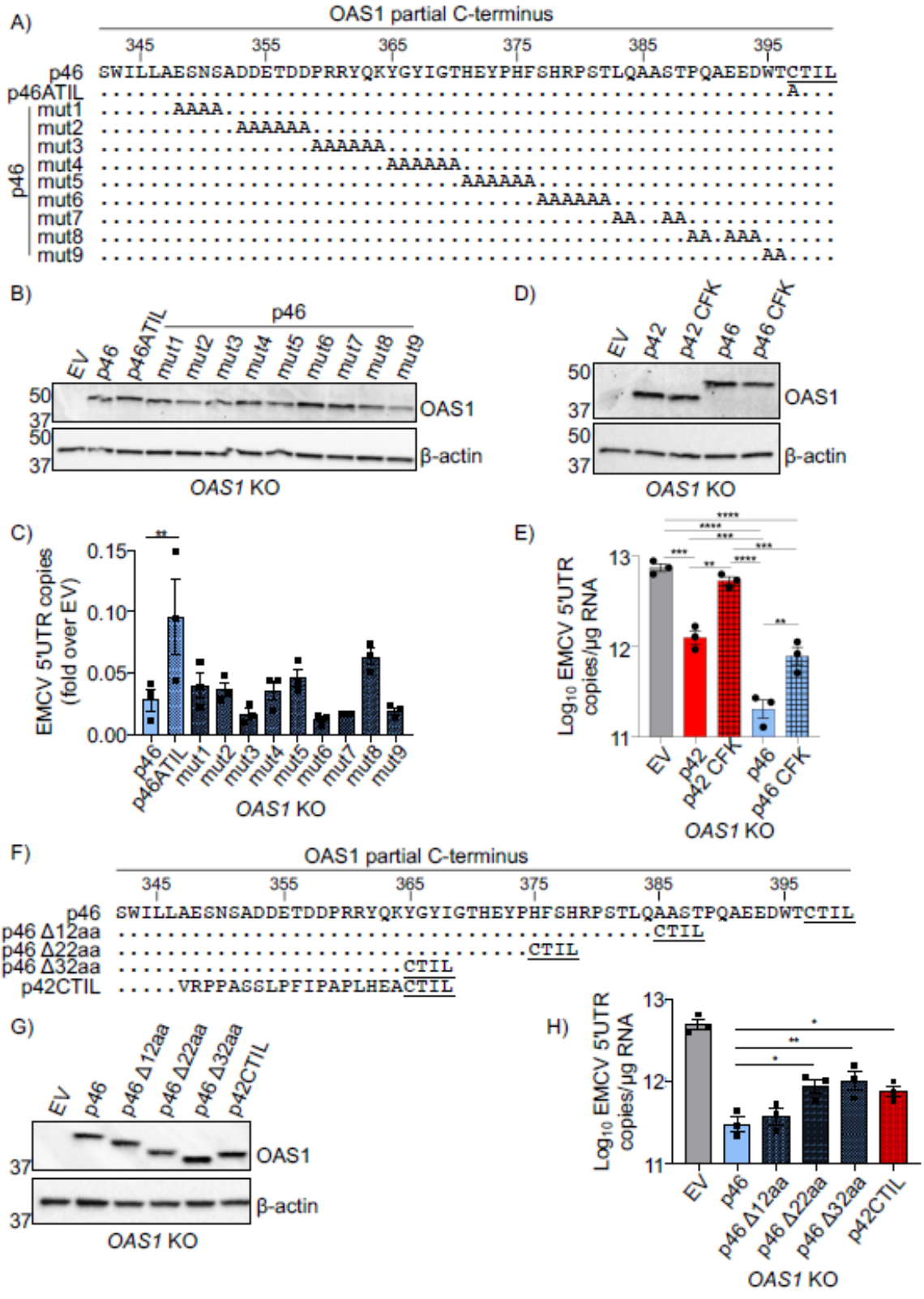
A)
OAS1 partial C-terminus
345
355
365
375
385
395
p46 SWILLAESNSADDETDDPRRYQKYGYIGTHEYPHFSHRPSTLQAASTPQAEEDWTCTIL
p46ATIL .....A...
mut1 ......AAAA.....
mut2 ....AAAAAA.....
mut3 ....AAAAAA.....
mut4 ....AAAAAA.....
mut5 ....AAAAAA.....
mut6 ....AAAAAA.....
mut7 ..........AA..AA.....
mut8 ..........AA.AAA.....
mut9 ....AA....
p46
B)
EV
p46
p46ATIL
p46
mut1
mut2
mut3
mut4
mut5
mut6
mut7
mut8
mut9
50
37
OAS1
50
37
β-actin
OAS1 KO
D)
EV
p42
p42 CFK
p46
p46 CFK
50
37
OAS1
50
37
β-actin
OAS1 KO
C)
EMCV 5'UTR copies (fold over EV)
0.15
0.10
0.05
0.00
**
p46
p46ATIL
mut1
mut2
mut3
mut4
mut5
mut6
mut7
mut8
mut9
OAS1 KO
E)
Log10 EMCV 5'UTR copies/µg RNA
13
12
11
****
****
***
***
***
**
****
**
EV
p42
p42 CFK
p46
p46 CFK
OAS1 KO
F)
OAS1 partial C-terminus
345
355
365
375
385
395
p46 SWILLAESNSADDETDDPRRYQKYGYIGTHEYPHFSHRPSTLQAASTPQAEEDWTCTIL
p46 Δ12aa .....CTIL
p46 Δ22aa .....CTIL
p46 Δ32aa .....CTIL
p42CTIL .....VRPPASSLPFIPAPLHEACTIL
G)
EV
p46
p46 Δ12aa
p46 Δ22aa
p46 Δ32aa
p42CTIL
37
OAS1
37
β-actin
OAS1 KO
H)
Log10 EMCV 5'UTR copies/µg RNA
13
12
11
*
**
*
EV
p46
p46 Δ12aa
p46 Δ22aa
p46 Δ32aa
p42CTIL
OAS1 KO

Figure 3.5. Combined effects of CaaX motif, C-terminus length, and oligomerization domain confer differential antiviral activity of OAS1 isoforms.

A) C-termini of OAS1 p46, p46ATIL, and p46 alanine substitution mutants 1-9. **B)** Immunoblot of control EV, p46, p46ATIL, and p46 alanine substitution mutants 1-9 in OAS1 KO 293T cells at 24h post transfection. **C)** Quantification of EMCV 5´UTR copies by qPCR from OAS1 KO 293T cells transfected with control EV, p46, p46ATIL, and p46 alanine substitution mutants 1-9 EV at 24h post infection with EMCV at an MOI of 0.001; data is expressed as fold of EV control **D)** Immunoblot of control EV, p42, p42 CFK mutant, p46, and p46 CFK mutant in OAS1 KO 293T cells at 24h post transfection. **E)** Quantification of EMCV 5´UTR copies by qPCR from OAS1 KO 293T cells transfected with control EV, p42, p42 CFK mutant, p46, and p46 CFK mutant at 24h post infection with EMCV at an MOI of 0.001. **F)** C-termini of OAS1 p46, p46 truncation mutants Δ12aa, Δ22aa, and Δ32aa, and p42CTIL. **G)** Immunoblot of control EV, p46, p46 truncation mutants Δ12aa, Δ22aa, and Δ32aa, and p42CTIL in *OAS1* KO 293T cells at 24h post transfection. **H)** Quantification of EMCV 5´UTR copies by qPCR from *OAS1* KO 293T cells transfected with control EV, p46, p46 truncation mutants Δ12aa, Δ22aa, and Δ32aa, and p42CTIL at 24h post infection with EMCV at an MOI of 0.001. For C) and H) data were analyzed by one-way ANOVA with Dunnett's multiple comparisons test (vs. p46) where *P<0.05, and **P<0.01. D). For E) data were analyzed using one-way ANOVA with Tukey's multiple comparisons test where **P<0.01, and ***P<0.001 and ****P<0.001

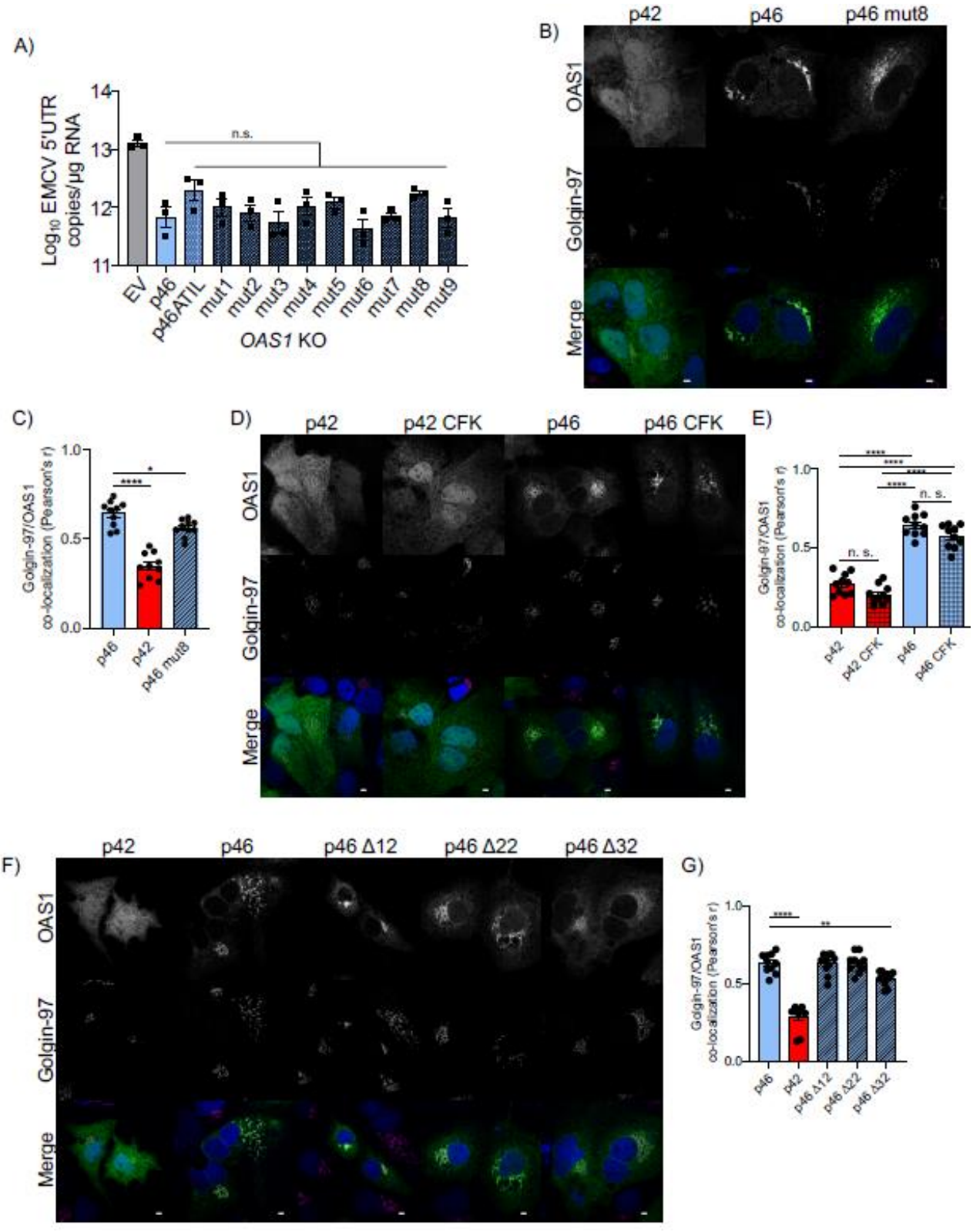
A)
Log10 EMCV 5'UTR copies/µg RNA
14
13
12
11
n.s.
EV
p46
p46ATIL
mut1
mut2
mut3
mut4
mut5
mut6
mut7
mut8
mut9
OAS1 KO
B)
p42
p46
p46 mut8
OAS1
Golgin-97
Merge
C)
Golgin-97/OAS1 co-localization (Pearson's r)
1.0
0.5
0.0
*
****
p46
p42
p46 mut8
D)
p42
p42 CFK
p46
p46 CFK
OAS1
Golgin-97
Merge
E)
Golgin-97/OAS1 co-localization (Pearson's r)
1.0
0.5
0.0
****
****
****
****
n. s.
n. s.
p42
p42 CFK
p46
p46 CFK
F)
p42
p46
p46 Δ12
p46 Δ22
p46 Δ32
OAS1
Golgin-97
Merge
G)
Golgin-97/OAS1 co-localization (Pearson's r)
1.0
0.5
0.0
****
**
p46
p42
p46 Δ12
p46 Δ22
p46 Δ32

Supplementary Figure 3.5 (related to figure 3.5).

A) Quantification of EMCV 5´UTR copies by qPCR from OAS1 KO 293T cells transfected with control EV, p46, p46ATIL, and p46 alanine substitution mutants 1-9 EV at 24h post infection with EMCV at an MOI of 0.001. **B)** Representative confocal slices of *OAS1* KO Huh7 cells expressing p42, p46, or p46 mut8 stained with anti-OAS1 and Golgin-97 antibodies (green, magenta) and DAPI (blue). **C)** OAS1 and Golgin-97 colocalization from B) is shown as Pearson's correlation. **D)** Representative confocal slices of OAS1 KO Huh7 cells expressing p42, p42 CFK, p46, or p46 CFK stained with anti-OAS1 and Golgin-97 antibodies (green, magenta) and DAPI (blue). **E)** OAS1 and Golgin-97 colocalization from D) is shown as Pearson's correlation. **F)** Representative confocal slices of OAS1 KO Huh7 cells expressing OAS1 p42, p46, p46 Δ12, p46 Δ22, or p46 Δ32 stained with anti-OAS1 and Golgin-97 antibodies (green, magenta) and DAPI (blue). **G)** OAS1 and Golgin-97 colocalization from F) is shown as Pearson's correlation. A), C), and G) Data were analyzed by one-way ANOVA with Dunnett's multiple comparisons test (vs. p46). E) Data were analyzed by one-way ANOVA with Tukey's multiple comparisons test. *P<0.05, **P<0.01 and ****P<0.0001. n.s. = not significant. Scale = 5 μm.

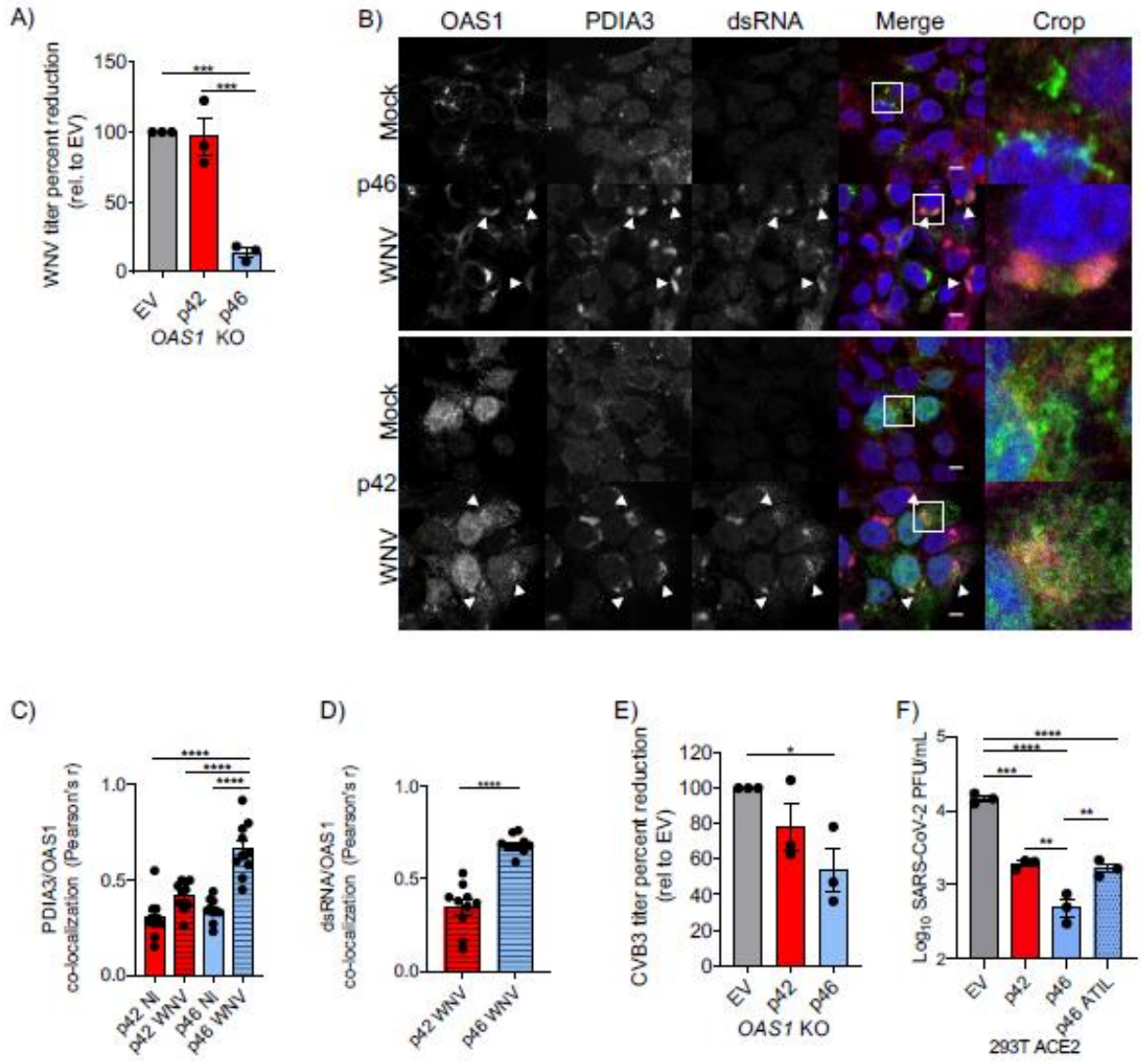

Figure 3.6. OAS1 p46 has broad antiviral activity against viruses that use the endomembrane system for replication.

A) WNV Texas titers (percent titer normalized to EV) 48h post infection with WNV at an MOI of 0.001 taken from OAS1 KO 293T cells transfected with control EV, p42, and p46. B) Representative confocal micrographs from mock or WNV Texas (MOI=1, 24h) infected OAS1 KO 293T cells expressing p42 or p46 and stained with DAPI (blue) and anti-OAS1 (green), PDIA3 (red), and dsRNA (magenta) antibodies. C) Pearson's correlation of OAS1 and PDIA3.

D) Pearson's correlation of OAS1 and dsRNA. E) CVB titers (percent titer normalized to EV) 48h post infection with CVB3 at an MOI of 0.001 in OAS1 KO 293T cells transfected with a control EV, p42, or p46. F) SARS-CoV-2 titers taken at 48h post infection from OAS1 KO 293T expressing EV, p42, p46, or p46ATIL for 24h. Scale = 5 μm. For A) C) E) and F) Data were analyzed using one-way ANOVA with Tukey's multiple comparisons test where *P<0.05, ***P<0.001, ****P<000.1 D) Data were analyzed using an unpaired t test where ****P<0.0001.

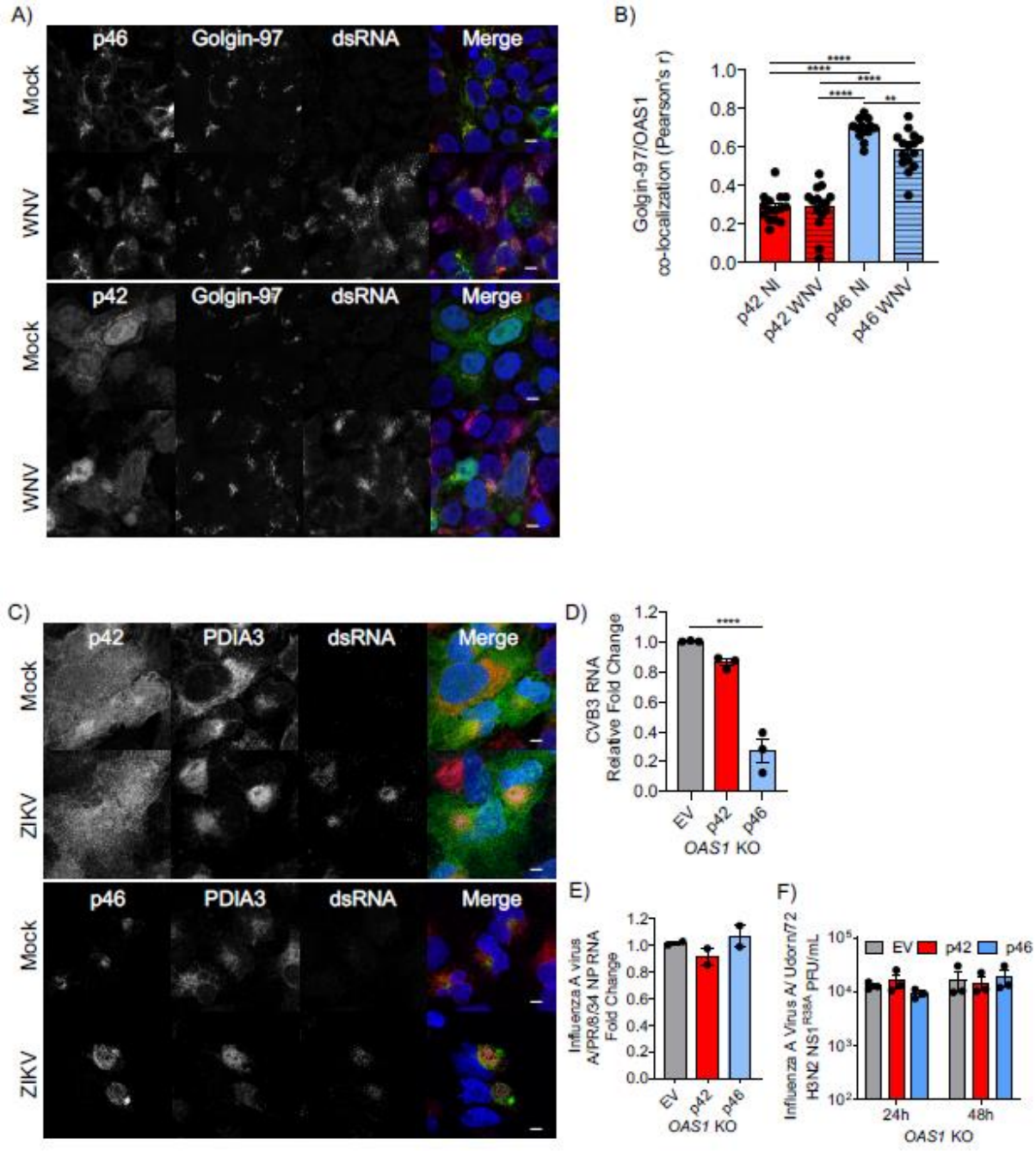

Supplementary Figure 3.6 (related to figure 3.6).

A) Representative confocal micrographs from mock or WNV Texas (MOI=1, 24h) infected OAS1 KO 293T cells expressing p42 or p46 and stained with DAPI (blue) and anti-OAS1

(green), Golgin-97 (red), and dsRNA (magenta) antibodies. **B)** Pearson's correlation of OAS1 and Golgin-97. **C)** Representative confocal micrographs from mock or Zika virus MR766 (MOI=5, 24h) infected OAS1 KO A549 cells expressing p42 or p46 and stained with DAPI (blue) and anti OAS1 (green), PDIA3 (red), and dsRNA (magenta) antibodies. **D)** Relative quantification of CVB3 RNA relative to EV in EV, p42, or p46 expressing cells infected with CVB3 at an MOI of 0.001 for 24h. **E)** Relative quantification of influenza A virus A/PR/8/34 NP RNA relative to EV. EV, p42, or p46 expressing cells were infected with A/PR/8/34 at an MOI of 0.01 for 24h. **F)** Viral titers quantified by plaque assay at 24h and 48h post infection with influenza virus A/Udorn/72 H3n2 R38A at an MOI of 0.01 in *OAS1* KO 293T cells expressing p42, p46, or an EV. Scale = 5 μm. B), D), E) and F) Data were analyzed using one-way ANOVA with Tukey's multiple comparisons test where **P<0.01 and ****P<0.0001

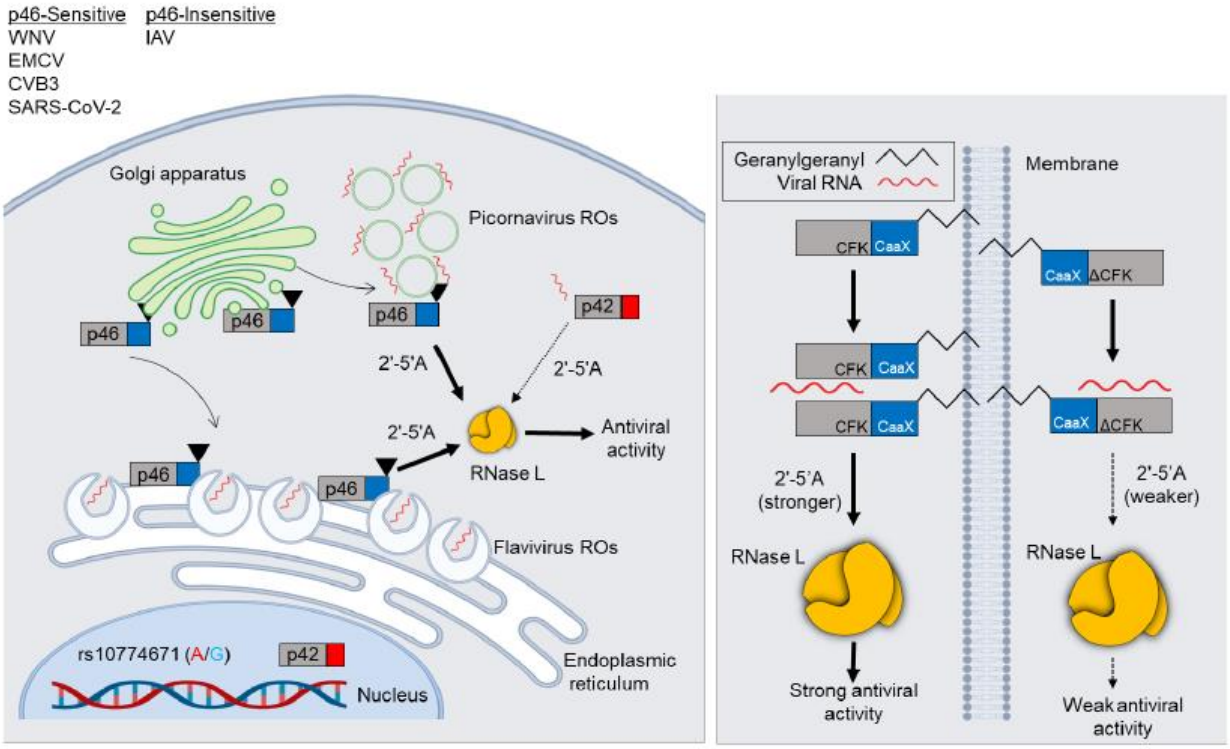

Figure 3.7. A schematic depicting how endomembrane targeting of OAS1 p46 primes antiviral activity against positive-strand RNA viruses.

Left**,** a splice-acceptor SNP (rs10774671) controls production of the p42/p46 OAS1 isoforms. Isoform-specific prenylation localizes p46 to the Golgi apparatus, while OAS1 p42 is cytosolic and, during positive-stand RNA virus infection, OAS1 p46 is recruited to virus replication organelles (VROs) of flaviviruses and picornaviruses. Through this targeting p46 gains enhanced access to viral RNA. OAS1 p42 remains cytosolic and nuclear during infection and has limited access to viral RNA. Both OAS1 isoforms require catalytic activity and RNase L to be antiviral. Cytosolic targeting of p42 may allow this protein to bind to cytosolic vRNA or host mRNA. Right, a CFK oligomerization domain is required for the enhanced antiviral activity of p46.

Table S3.1. Nucleic acids used in this study.

Primers	Sequence 5'-3'
OAS1 common For	GCTTGGTACCGAGCTCGGATCC
OAS1 common Rev	CAGCAGAATCCAGGAGCTCACTGG
OAS1 p42 For	AGTGAGCTCCTGGATTCTGCTGGTGAGACCTCCTGCTTCCTCCC
OAS1 p42 wt Rev	CTATAGAATAGGGCCCTCTAGATCAAGCTTCATGGAGAGGGGC AG
OAS1 p42 CaaX Rev	TATAGAATAGGGCCCTCTAGATCAGAGGATGGTGCAAGCTTCAT
OAS1 p46 For	CCCAGTGAGCTCCTGGATTCTGCTGGCTGAAAGCAACAGTGCAG ACG
OAS1 p46 wt CaaX Rev	ACTATAGAATAGGGCCCTCTAGATCAGAGGATGGTGCAGGTCC A
OAS1 p46 mut CaaX Rev	ACTATAGAATAGGGCCCTCTAGATCAGAGGATGGTGGCGGTC
OAS1 p48 For	AGTGAGCTCCTGGATTCTGCTGACCCAGCACACTCCAGGCAG
OAS1 p48 Rev	CTATAGAATAGGGCCCTCTAGATCAGGAGACCTGGGTTCTGTCC
OAS1DADA_F	GAAGACAACCAGGGCAGCGGCAGATCGGCCTCT
OAS1DADA_R	AGAGGCCGATCTGCCGCTGCCCTGGTT
OAS1FLAG_F	CGACTCACTATAGGGAGACCCAAGCTTGGTACCGAGCTCGATG GACTACAAAGAC
OAS1FLAG_R	GTCCAGAGATTTGGCTGGGGTATTTCTGAGATCCATCATGCTTG TCATCGTCATCCTTGTAATCGATG
EMCV_F	AGATCCGGATTGCCAGTCT
EMCV_R	CACTATCGTAGCCTTCACGTTG
EMCV_probe	/56-FAM/AT ATC GCA G/ZEN/G CTG GGT CCG T/3IABkFQ/
IAV NP Fwd	CGTTCTCCATCAGTCTCCATC
IAV NP Rev	GAGTGACATCAAAATCATGGCG
OAS1 CFK mut SDM fwd	CTGAGGCCTGGCTGAATTACCCAGCCGCTGCGAATTGGGATGGG TCCCCAGTGA
OAS1 CFK mut SDM rev	TCACTGGGGACCCATCCCAATTCGCAGCGGCTGGGTAATTCAGC CAGGCCTCAG
OAS1 p46Δ32 SDM fwd	ACGATCCCAGGAGGTATCAGAAATGCACCATCCTC
OAS1 p46Δ32 SDM rev	GAGGATGGTGCATTTCTGATACCTCCTGGGATCGT
OAS1 p46Δ22 SDM fwd	ACATTGGAACACATGAGTACCCTTGCACCATCCTCT

OAS1 p46Δ22 SDM rev	AGAGGATGGTGCAAGGGTACTCATGTGTTCCAATGT
OAS1 p46Δ12 SDM fwd	CCCAGCACACTCCAGTGCACCATCCTCTGA
OAS1 p46Δ12 SDM rev	TCAGAGGATGGTGCACTGGAGTGTGCTGGG
OAS1 SDM common+CTIL fwd	AGAGGGGCAGGGATGAATGGCAGGGAGGACTAAAGAATCGTG CACAGCAGAATCCAGGAGCTCACTGGGGACC
OAS1 SDM common+CTIL rev	GGTCCCCAGTGAGCTCCTGGATTCTGCTGTGCACGATTCTTTAGT CCTCCCTGCCATTCATCCCTGCCCCTCT
OAS1 p46 Ala mut9 SDM fwd	CAGAGGATGGTGCAGGCCGCGTCCTCTTCTGCCTGT
OAS1 p46 Ala mut9 SDM rev	ACAGGCAGAAGAGGACGCGGCCTGCACCATCCTCTG
p52_F	CCCAGTGAGCTCCTGGATTCTGCTGCTGAAAGCAACAGTACAGA CGATG
p52_R	ACTATAGAATAGGGCCCTCTAGATTATCTATGATAGGATAGAGG GCATAGAA
S/AS oligos	**Sequence 5'-3'**
OAS1 p42 WT S	GTGAGACCTCCTGCTTCCTCCCTGCCATTCATCCCTGCCCCTCTC CATGAAGCTTGA
OAS1 p42 WT AS	TCAAGCTTCATGGAGAGGGGCAGGGATGAATGGCAGGGAGGAA GCAGGAGGTCTCAC
OAS1 p42 CaaX S	GTGAGACCTCCTGCTTCCTCCCTGCCATTCATCCCTGCCCCTCTC CATGAAGCTTGCACCATCCTCTGA
OAS1 p42 CaaX AS	TCAGAGGATGGTGCAAGCTTCATGGAGAGGGGCAGGGATGAAT GGCAGGGAGGAAGCAGGAGGTCTCAC
OAS1 p44 WT S	CCCAGTGAGCTCCTGGATTCTGCTGGTAAACCTCACACTGGTTG GCAGAAGGAACTATACCAATAATTAGTCTAGAGGGCCCTATTCT ATAGTGT
OAS1 p44 WT AS	ACACTATAGAATAGGGCCCTCTAGACTAATTATTGGTATAGTTC CTTCTGCCAACCAGTGTGAGGTTTACCAGCAGAATCCAGGAGCT CACTGGG
gBlocks (partial)	**Sequence 5'-3'**
OAS1 p46 WT	GCTGAAAGCAACAGTGCAGACGATGAGACCGACGATCCCAGGA GGTATCAGAAATATGGTTACATTGGAACACATGAGTACCCTCAT TTCTCTCATAGACCCAGCACACTCCAGGCAGCATCCACCCCACA GGCAGAAGAGGACTGGACCTGCACCATCCTCTGA
OAS1 p46 mutCaaX	GCTGAAAGCAACAGTGCAGACGATGAGACCGACGATCCCAGGA GGTATCAGAAATATGGTTACATTGGAACACATGAGTACCCTCAT TTCTCTCATAGACCCAGCACACTCCAGGCAGCATCCACCCCACA GGCAGAAGAGGACTGGACCGCCACCATCCTCTGA

OAS1 p48 WT	ACCCAGCACACTCCAGGCAGCATCCACCCCACAGGCAGAAGAG GACTGGACCTGCACCATCCTCTGAATGCCAGTGCATCTTGGGGG AAAGGGCTCCAGTGTTATCTGGACCAGTTCCTTCATTTTCAGGT GGGACTCTTGATCCAGAGAGGACAAAGCTCCTCAGTGAGCTGG TGTATAATCCAGGACAGAACCCAGGTCTCCTGA
OAS1 p52 WT	CTGAAAGCAACAGTACAGACGATGAGACCGACGATCCCAGGAC GTATCAGAAATATGGTTACATTGGAACACATGAGTACCCTCATT TCTCTCATAGACCCAGCACACTCCAGGCAGCATCCACCCCACAG GCAGAAGAGGACTGGACCTGCACCATCCTCTGAATGCCAGTGC ATCTTGGGGGAAAGGGCTCCAGTGTTATCTGGACCAGTTCCTTC ATTTTCAGGTGGGACTCTTGATCCAGAGAAGACAAAGCTCCTCA GTGAGCTGGTGTATAATCCAGGACAGAACCCAGGTCTCCTGACT CCTGGCCTTCTATGCCCTCTATCCTATCATAGATAA
OAS1 p46 Ala mut1	TGCTTTAAGAATTGGGATGGGTCCCCAGTGAGCTCCTGGATTCT GCTGGCTGCCGCGGCAGCTGCAGACGATGAGACCGACGATCCC AGGAGGTATCAGAAATATGGTTACATTGGAACACATGAGTACC CTCATTTCTCTCATAGACCCAGCACACTCCAGGCAGCATCCACC CCACAGGCAGAAGAGGACTGGACCTGCACCATCCTCTGATCTA GAGGGCCCTATTCTATAGTGTCACCTA
OAS1 p46 Ala mut2	TGCTTTAAGAATTGGGATGGGTCCCCAGTGAGCTCCTGGATTCT GCTGGCTGAAAGCAACAGTGCAGCGGCAGCTGCCGCAGCGCCC AGGAGGTATCAGAAATATGGTTACATTGGAACACATGAGTACC CTCATTTCTCTCATAGACCCAGCACACTCCAGGCAGCATCCACC CCACAGGCAGAAGAGGACTGGACCTGCACCATCCTCTGATCTA GAGGGCCCTATTCTATAGTGTCACCTA
OAS1 p46 Ala mut3	TGCTTTAAGAATTGGGATGGGTCCCCAGTGAGCTCCTGGATTCT GCTGGCTGAAAGCAACAGTGCAGACGATGAGACCGACGATGCT GCCGCGGCAGCTGCATATGGTTACATTGGAACACATGAGTACCC TCATTTCTCTCATAGACCCAGCACACTCCAGGCAGCATCCACCC CACAGGCAGAAGAGGACTGGACCTGCACCATCCTCTGATCTAG AGGGCCCTATTCTATAGTGTCACCTA
OAS1 p46 Ala mut4	TGCTTTAAGAATTGGGATGGGTCCCCAGTGAGCTCCTGGATTCT GCTGGCTGAAAGCAACAGTGCAGACGATGAGACCGACGATCCC AGGAGGTATCAGAAAGCTGCCGCGGCAGCTGCACATGAGTACC CTCATTTCTCTCATAGACCCAGCACACTCCAGGCAGCATCCACC CCACAGGCAGAAGAGGACTGGACCTGCACCATCCTCTGATCTA GAGGGCCCTATTCTATAGTGTCACCTA
OAS1 p46 Ala mut5	TGCTTTAAGAATTGGGATGGGTCCCCAGTGAGCTCCTGGATTCT GCTGGCTGAAAGCAACAGTGCAGACGATGAGACCGACGATCCC AGGAGGTATCAGAAATATGGTTACATTGGAACAGCTGCCGCGG CAGCTGCATCTCATAGACCCAGCACACTCCAGGCAGCATCCACC CCACAGGCAGAAGAGGACTGGACCTGCACCATCCTCTGATCTA GAGGGCCCTATTCTATAGTGTCACCTA

OAS1 p46 Ala mut6	TGCTTTAAGAATTGGGATGGGTCCCCAGTGAGCTCCTGGATTCT GCTGGCTGAAAGCAACAGTGCAGACGATGAGACCGACGATCCC AGGAGGTATCAGAAATATGGTTACATTGGAACACATGAGTACC CTCATTTCGCTGCCGCGGCAGCTGCACTCCAGGCAGCATCCACC CCACAGGCAGAAGAGGACTGGACCTGCACCATCCTCTGATCTA GAGGGCCCTATTCTATAGTGTCACCTA
OAS1 p46 Ala mut7	TGCTTTAAGAATTGGGATGGGTCCCCAGTGAGCTCCTGGATTCT GCTGGCTGAAAGCAACAGTGCAGACGATGAGACCGACGATCCC AGGAGGTATCAGAAATATGGTTACATTGGAACACATGAGTACC CTCATTTCTCTCATAGACCCAGCACAGCTGCCGCGGCAGCTGCA CCACAGGCAGAAGAGGACTGGACCTGCACCATCCTCTGATCTA GAGGGCCCTATTCTATAGTGTCACCTA
OAS1 p46 Ala mut8	TGCTTTAAGAATTGGGATGGGTCCCCAGTGAGCTCCTGGATTCT GCTGGCTGAAAGCAACAGTGCAGACGATGAGACCGACGATCCC AGGAGGTATCAGAAATATGGTTACATTGGAACACATGAGTACC CTCATTTCTCTCATAGACCCAGCACACTCCAGGCAGCATCCACC GCTGCCGCGGCAGCTGCATGGACCTGCACCATCCTCTGATCTAG AGGGCCCTATTCTATAGTGTCACCTA
siRNA	**Sequence 5'-3'**
OAS1	AGUCAAGCACUGGUACCAACAAUUUUGGUACCAGUG
p42	GGUCACAAUCGAGGGUUAUUCCAGAAACCCUCGAU
p46	AGAGAGAUUUAGAUAAGAUUCAUUCUCUUAUCUAAA

Table S3.2. Antibodies used in this study.

Name	Vendor/Source	Catalog
OAS1 (D1W3A) Rabbit mAb	Cell Signaling Technology	14498
RNase L (D4B4J) Rabbit mAb	Cell Signaling Technology	27281
Golgin-97 (CDF4) Mouse mAb	Cell Signaling Technology	97537
Monoclonal Anti-PDIA3 antibody raised in mouse	Sigma-Aldrich	AMAB90988
Golgin-97 (CDF4), Unconjugated, Species Reactivity: Human, Host: Mouse / IgG1	Thermo Scientific	A-21270
Monoclonal ANTI-FLAG® M2 antibody raised in mouse	Sigma-Aldrich	F3165
J2 monoclonal antibody (mAb) anti dsRNA, mouse, IgG2a	Scicons	10010200
Mouse monoclonal antibody 9D5 anti dsRNA	Adam Geballe lab	N/A
β-Actin (13E5) Rabbit mAb	Cell Signaling Technology	4970
Goat anti Mouse IgG2a Alexa Fluor 647	Thermo Fisher Scientific	A21241
Goat anti Mouse IgG1 Alexa Fluor 594	Thermo Fisher Scientific	A21125
Goat anti Rabbit Alexa Fluor 488	Thermo Fisher Scientific	A11008

Table S3.3. Clinical and demographic information for COVID-19 and matched healthy control cohort.

Cohort	Number	M:F	Ancestry	Disease severity
Severe COVID-19	35	15:20	23% Caucasian 29% Latino 11% African American 9% Asian 14% American Indian 14% Other race/declined	Critical care unit, mechanical ventilation
Ancestry matched healthy controls	99	47:52	34% Caucasian 22% Latino 19% African American 12% Asian 8% American Indian 3% Pacific Islander	Not applicable

Chapter 4. Conclusions and future directions.

In this dissertation, we defined isoform-specific prenylation as an important determinant of the antiviral activity of ZAP and OAS1 by directing these proteins to sites of viral RNA accumulation. For ZAP, prenylation of the long isoform localized this protein to sites of alphavirus replication at the plasma membrane and endolysosomes. The short isoform of ZAP, which is generated by alternative splicing, is not prenylated and localizes to the cytosol. Although ZAP-S has inferior antiviral activity against alphaviruses when compared to ZAP-L, ZAP-S binds to and regulates type I and III interferon mRNA. Mutating the CaaX motif on ZAP-L and adding a CaaX motif to ZAP-S swapped the antiviral activities and interferon mRNA binding capacity of these isoforms. Since ZAP has antiviral activity against many other viruses, including retroviruses and filoviruses, the role of ZAP isoforms and the CaaX motif in the antiviral activity of ZAP needs to be investigated further. We hypothesize, for example, that ZAP-S may have higher antiviral activity against RNA viruses that predominately replicate in the cytosol such as Reoviruses and Rhabdoviruses.

For OAS1, we demonstrated the p46 isoform contains a C-terminal CaaX motif that targets this isoform primarily to Golgi membranes. Other isoforms of OAS1, such as p42, do not contain a CaaX motif and instead localize to the cytosol and the nucleus. Compared to p42, the p46 isoform had enhanced antiviral activity against positive-strand RNA viruses that utilized the endomembrane system for replication (EMCV, CVB3, WNV, and SARS-CoV-2). Compared to p42, the p46 isoform localized to sites of viral RNA replication and had enhanced access to viral RNA. This was dependent on the CaaX motif, suggesting membrane-targeting is important for this isoform to access viral RNA. Once hypothesis is that, by being targeted to membranes, OAS1 p46 may miss viral RNA that accumulates in the cytosol. Therefore, the production of

cytosolic OAS1 isoforms, such as p42, might represent a more generalist strategy for sensing viral RNA.

Collectively, the results of this thesis emphasize the importance of subcellular localization to antiviral activity. Interestingly, differential subcellular localization can be generated by alternative splicing through the production of isoforms with or without a membrane-targeting CaaX motif. Although the focus of this thesis, prenylation is only one of many lipidation modifications that can target proteins to organelle surfaces and thereby potentially modify antiviral activity. Future studies should aim at deciphering the role of other lipidation modifications in directing antiviral proteins to sites utilized by viruses for replication.

In a broader sense, the work herein suggests a model in which the host may guard the surface of organelle membranes with antiviral effectors (Fig 4.1). Organelle-localized antiviral effectors may have enhanced access to the replication compartments of positive-strand RNA viruses over cytosolic localized effectors. This model posits the specificity of an organelle targeted innate immune antiviral protein can be predicted by the particular organelle(s) to which the antiviral protein localizes. For example, a plasma membrane targeted antiviral effector may be able to access alphavirus ROs, but have limited access to flavivirus and coronavirus ROs (Fig 1.4). Future work should address the subcellular localization of antiviral effectors at organelle membranes in the steady state, after innate immune activation, and during infection with various positive-strand RNA viruses. Such information will help us understand the extent to which the host guards organelle membranes from usurpation by positive-strand RNA viruses. On the other hand, there is still much to learn about the precise organelle rearrangements that occur when a cell is infected with different positive-strand RNA viruses. Overall, this work adds to our

understanding of how the innate antiviral state is broadly antiviral through the collective action of antiviral effectors that, individually, are specific for different viral threats.

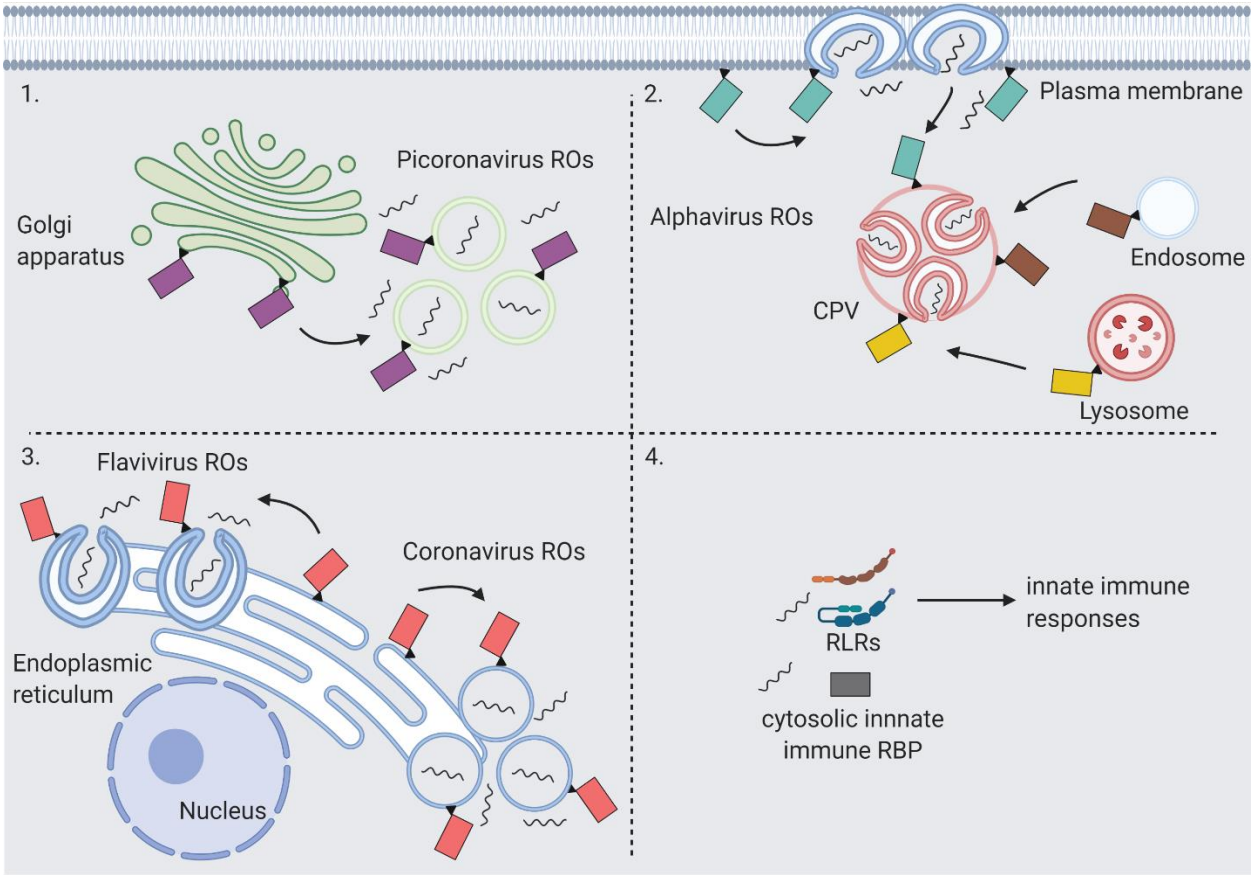

Figure 4.1. Organelle-specific targeting of antiviral effectors defines their antiviral specificity against positive-strand RNA viruses.

This model posits that distinct organelle localization of innate immune RNA binding proteins can determine their specificity against positive-strand RNA viruses as these viruses use unique combinations of organelle membranes for replication. 1) A Golgi-targeted antiviral RNA binding protein is recruited to the replication organelle of picronaviruses, which primarily use Golgi membranes for replication organelle formation. 2) Alphavirus RNA replication begins at the plasma membrane in spherules. Later, spherules are internalized and merge with endosomal and lysosomal membrane to form the cytopathic vacuole (CPV). Thus plasma membrane, lysosomal, and endosomal localized proteins may all have access to the replication organelles of alphaviruses. 3) An endoplasmic reticulum localized innate immune RNA binding protein gains

access to flaviviruses and coronaviruses replication organelles. 4) Viral RNA ultimately escapes to the cytosol, where it interacts with host innate immune effectors localized to this compartment such as the RIG-I like receptors (RLRs). Cytosolic RNA sensed in this manner induces an innate immune response through RLR signaling.

BIBLIOGRAPHY

1. S. Froshauer, J. Kartenbeck, A. Helenius, Alphavirus RNA replicase is located on the cytoplasmic surface of endosomes and lysosomes. *The Journal of Cell Biology* **107**, (1988).

2. P. M. Grimley, I. K. Berezesky, R. M. Friedman, Cytoplasmic structures associated with an arbovirus infection: loci of viral ribonucleic acid synthesis *Journal of Virology* **2**, (1968).

3. R. M. Friedman, J. G. Levin, P. M. Grimley, I. K. Berezesky, Membrane-associated replication complex in arbovirus infection *Journal of Virology* **10**, (1972).

4. N. H. Acheson, I. Tamm, Replication of semliki forest virus an electron microscopic study. *Virology* **32**, (1967).

5. R. Gorchakov *et al.*, A new role for ns polyprotein cleavage in Sindbis virus replication. *J Virol* **82**, 6218-6231 (2008).

6. P. Kujala *et al.*, Biogenesis of the Semliki Forest virus RNA replication complex. *J Virol* **75**, 3873-3884 (2001).

7. E. I. Frolova, R. Gorchakov, L. Pereboeva, S. Atasheva, I. Frolov, Functional Sindbis virus replicative complexes are formed at the plasma membrane. *J Virol* **84**, 11679-11695 (2010).

8. M. K. Pietilü, M. J. v. Hemert, T. Ahola, Purification of highly active alphavirus replication complexes demonstrates altered fractionation of multiple cellular membranes *Journal of Virology* **92**, (2018).

9. K. Knoops *et al.*, SARS-coronavirus replication is supported by a reticulovesicular network of modified endoplasmic reticulum. *PLoS Biol* **6**, e226 (2008).

10. S. Stertz *et al.*, The intracellular sites of early replication and budding of SARS-coronavirus. *Virology* **361**, 304-315 (2007).

11. E. J. Snijder *et al.*, A unifying structural and functional model of the coronavirus replication organelle: Tracking down RNA synthesis. *PLoS Biol* **18**, e3000715 (2020).

12. M. Cortese *et al.*, Integrative imaging reveals SARS-CoV-2 induced reshaping of subcellular morphologies. *Cell Host & Microbe*, (2020).

13. M. M. Angelini, M. Akhlaghpour, B. W. Neuman, M. J. Buchmeier, Severe acute respiratory syndrome coronavirus nonstructural proteins 3, 4, and 6 induce double-membrane vesicles. *mBio* **4**, (2013).

14. G. Wolff *et al.*, A molecular pore spans the double membrane of the coronavirus replication organelle *Science* **369**, (2020).

15. G. A. Belov *et al.*, Complex dynamic development of poliovirus membranous replication complexes. *J Virol* **86**, 302-312 (2012).

16. R. W. Limpens *et al.*, The transformation of enterovirus replication structures: a three-dimensional study of single- and double-membrane compartments. *mBio* **2**, (2011).

17. K. Bienz, D. Egger, L. Pasamontes, Association of polioviral proteins of the P2 genomic region with the viral replication complex and virus-induced membrane synthesis as visualized by electron microscopic immunocytochemistry and autoradiography *Virology* **160**, (1987).

18. N. Takeda, R. J. Kuhn, C.-F. Yang, T. Takegami, E. Wimmer, Initiation of poliovirus plus-strand RNA synthesis in a membrane complex of infected HeLa cells *Journal of Virology* **60**, (1986).

19. M. P. Taylor, T. B. Burgon, K. Kirkegaard, W. T. Jackson, Role of microtubules in extracellular release of poliovirus. *J Virol* **83**, 6599-6609 (2009).

20. N. Y. Hsu *et al.*, Viral reorganization of the secretory pathway generates distinct organelles for RNA replication. *Cell* **141**, 799-811 (2010).

21. H. M. van der Schaar *et al.*, Illuminating the Sites of Enterovirus Replication in Living Cells by Using a Split-GFP-Tagged Viral Protein. *mSphere* **1**, (2016).

22. R. C. Rust *et al.*, Cellular COPII proteins are involved in production of the vesicles that form the poliovirus replication complex. *J Virol* **75**, 9808-9818 (2001).

23. A. Schlegel, T. H. Giddings, M. S. Ladinsky, K. Kirkegaard, Cellular origin and ultrastructure of membranes induced during poliovirus infection *Journal of Virology* **70**, (1996).

24. C. E. Melia *et al.*, Origins of Enterovirus Replication Organelles Established by Whole-Cell Electron Microscopy. *mBio* **10**, (2019).

25. O. Laufman, J. Perrino, R. Andino, Viral Generated Inter-Organelle Contacts Redirect Lipid Flux for Genome Replication. *Cell* **178**, 275-289 e216 (2019).

26. M. Cortese *et al.*, Ultrastructural Characterization of Zika Virus Replication Factories. *Cell Rep* **18**, 2113-2123 (2017).

27. L. K. Gillespie, A. Hoenen, G. Morgan, J. M. Mackenzie, The endoplasmic reticulum provides the membrane platform for biogenesis of the flavivirus replication complex. *J Virol* **84**, 10438-10447 (2010).

28. L. Miorin *et al.*, Three-dimensional architecture of tick-borne encephalitis virus replication sites and trafficking of the replicated RNA. *J Virol* **87**, 6469-6481 (2013).

29. S. Welsch *et al.*, Composition and three-dimensional architecture of the dengue virus replication and assembly sites. *Cell Host Microbe* **5**, 365-375 (2009).

30. J. M. Mackenzie, M. T. Kenney, E. G. Westaway, West Nile virus strain Kunjin NS5 polymerase is a phosphoprotein localized at the cytoplasmic site of viral RNA synthesis. *J Gen Virol* **88**, 1163-1168 (2007).

31. J. M. Mackenzie, A. A. Khromykh, M. K. Jones, E. G. Westaway, Subcellular localization and some biochemical properties of the flavivirus kunjin nonstructural proteins NS2A and NS4A. *Virology* **245**, (1998).

32. P. H. Kaufusi, J. F. Kelley, R. Yanagihara, V. R. Nerurkar, Induction of endoplasmic reticulum-derived replication-competent membrane structures by West Nile virus non-structural protein 4B. *PLoS One* **9**, e84040 (2014).

33. S. Miller, S. Kastner, J. Krijnse-Locker, S. Buhler, R. Bartenschlager, The non-structural protein 4A of dengue virus is an integral membrane protein inducing membrane alterations in a 2K-regulated manner. *J Biol Chem* **282**, 8873-8882 (2007).

34. S. Miller, S. Sparacio, R. Bartenschlager, Subcellular localization and membrane topology of the Dengue virus type 2 Non-structural protein 4B. *J Biol Chem* **281**, 8854-8863 (2006).

35. D. L. Akey *et al.*, Flavivirus NS1 structures reveal surfaces for associations with membranes and the immune system *Science* **343**, (2014).

36. C. J. Neufeldt *et al.*, ER-shaping atlastin proteins act as central hubs to promote flavivirus replication and virion assembly. *Nat Microbiol* **4**, 2416-2429 (2019).

37. I. Romero-Brey *et al.*, Three-dimensional architecture and biogenesis of membrane structures associated with hepatitis C virus replication. *PLoS Pathog* **8**, e1003056 (2012).

38. B. Wolk, B. Buchele, D. Moradpour, C. M. Rice, A dynamic view of hepatitis C virus replication complexes. *J Virol* **82**, 10519-10531 (2008).

39. D. Egger *et al.*, Expression of hepatitis C virus proteins induces distinct membrane alterations including a candidate viral replication complex. *J Virol* **76**, 5974-5984 (2002).

40. R. Gosert *et al.*, Identification of the hepatitis C virus RNA replication complex in Huh-7 cells harboring subgenomic replicons. *J Virol* **77**, 5487-5492 (2003).

41. D. Paul, S. Hoppe, G. Saher, J. Krijnse-Locker, R. Bartenschlager, Morphological and biochemical characterization of the membranous hepatitis C virus replication compartment. *J Virol* **87**, 10612-10627 (2013).

42. Y. Miyanari *et al.*, Hepatitis C virus non-structural proteins in the probable membranous compartment function in viral genome replication. *J Biol Chem* **278**, 50301-50308 (2003).

43. D. Quinkert, R. Bartenschlager, V. Lohmann, Quantitative analysis of the hepatitis C virus replication complex. *J Virol* **79**, 13594-13605 (2005).

44. C. J. Neufeldt *et al.*, Hepatitis C virus-induced cytoplasmic organelles use the nuclear transport machinery to establish an environment conducive to virus replication. *PLoS Pathog* **9**, e1003744 (2013).

45. S. N. Lester, K. Li, Toll-like receptors in antiviral innate immunity. *J Mol Biol* **426**, 1246-1264 (2014).

46. L. Alexopoulou, A. C. Holt, R. Medzhitov, R. A. Flavell, Recognition of double-strande RNA and activation of NF-kB by Toll-like receptor 3 *Nature* **413**, (2001).

47. H. S. Hardarson *et al.*, Toll-like receptor 3 is an essential component of the innate stress response in virus-induced cardiac injury. *American Journal of Physiology-Heart and Circulatory Physiology* **292**, H251-H258 (2007).

48. H. Negishi *et al.*, A critical link between Toll-like receptor 3 and type II interferon signaling pathways in antiviral innate immunity *PNAS* **105**, (2008).

49. N. Wang *et al.*, Toll-Like Receptor 3 Mediates Establishment of an Antiviral State against Hepatitis C Virus in Hepatoma Cells. *Journal of Virology* **83**, 9824-9834 (2009).

50. Y.-T. Tsai, S.-Y. Chang, C.-N. Lee, C.-L. Kao, Human TLR3 recognizes dengue virus and modulates viral replicationin vitro. *Cellular Microbiology* **11**, 604-615 (2009).

51. F. Heil *et al.*, Species-specific recognition of single-stranded RNA via toll-like receptor 7 and 8. *Science* **303**, (2004).

52. S. S. Diebold, T. Kaisho, H. Hemmi, S. Akira, C. R. e. Sousa, Innate antiviral responses by means of TLR7-mediated recognition of single-stranded RNA. *Science* **303**, (2004).

53. V. Hornung *et al.*, Quantitative Expression of Toll-Like Receptor 1‑10 mRNA in Cellular Subsets of Human Peripheral Blood Mononuclear Cells and Sensitivity to CpG Oligodeoxynucleotides. *The Journal of Immunology* **168**, 4531-4537 (2002).

54. T. Town *et al.*, Toll-like receptor 7 mitigates lethal West Nile encephalitis via interleukin 23-dependent immune cell infiltration and homing. *Immunity* **30**, 242-253 (2009).

55. L. Cervantes-Barragan *et al.*, Control of coronavirus infection through plasmacytoid dendritic-cell-derived type I interferon. *Blood* **109**, 1131-1137 (2007).

56. K. Takahashi *et al.*, Plasmacytoid dendritic cells sense hepatitis C virus-infected cells, produce interferon, and inhibit infection. *Proc Natl Acad Sci U S A* **107**, 7431-7436 (2010).

57. K. Triantafilou *et al.*, Human cardiac inflammatory responses triggered by Coxsackie B viruses are mainly Toll-like receptor (TLR) 8-dependent. *Cell Microbiol* **7**, 1117-1126 (2005).

58. D.-c. Kang *et al.*, *mda-5*: an inferon-inducible putative RNA helicase with double-stranded RNA-dependent ATPase activity and melanoma growth-suppressive properties *PNAS* **99**, (2002).

59. M. Yoneyama *et al.*, The RNA helicase RIG-I has an essential function in double-stranded RNA-induced innate antiviral responses. *Nat Immunol* **5**, 730-737 (2004).

60. T. Saito *et al.*, Regulation of innate antiviral defenses through a shared repressor domain in RIG-I and LGP2. *PNAS* **104**, (2007).

61. T. Venkataraman *et al.*, Loss of DExD/H box RNA helicase LGP2 manifests disparate antiviral responses. *J Immunol* **178**, 6444-6455 (2007).

62. D. Goubau, S. Deddouche, C. Reis e Sousa, Cytosolic sensing of viruses. *Immunity* **38**, 855-869 (2013).

63. H. Kato *et al.*, Cell type-specific involvement of RIG-I in antiviral response. *Immunity* **23**, 19-28 (2005).

64. Y. M. Loo *et al.*, Distinct RIG-I and MDA5 signaling by RNA viruses in innate immunity. *J Virol* **82**, 335-345 (2008).

65. K. Esser-Nobis *et al.*, Comparative Analysis of African and Asian Lineage-Derived Zika Virus Strains Reveals Differences in Activation of and Sensitivity to Antiviral Innate Immunity. *J Virol* **93**, (2019).

66. L. Gitlin *et al.*, Essential role of mda-5 in type I IFN responses to polyriboinosinic:polyribocytidylic acid and encephalomyocarditis picornavirus *PNAS* **103**, (2006).

67. Q. Feng *et al.*, MDA5 detects the double-stranded RNA replicative form in picornavirus-infected cells. *Cell Rep* **2**, 1187-1196 (2012).

68. S. A. McCartney *et al.*, MDA-5 recognition of a murine norovirus. *PLoS Pathog* **4**, e1000108 (2008).

69. J. K. Roth-Cross, S. J. Bender, S. R. Weiss, Murine coronavirus mouse hepatitis virus is recognized by MDA5 and induces type I interferon in brain macrophages/microglia. *J Virol* **82**, 9829-9838 (2008).

70. B. L. Fredericksen, B. C. Keller, J. Fornek, M. G. Katze, M. Gale, Jr., Establishment and maintenance of the innate antiviral response to West Nile Virus involves both RIG-I and MDA5 signaling through IPS-1. *J Virol* **82**, 609-616 (2008).

71. J. W. Schoggins *et al.*, A diverse range of gene products are effectors of the type I interferon antiviral response. *Nature* **472**, 481-485 (2011).

72. V. Hornung *et al.*, 5'-triphosphate RNA is the ligand for RIG-I. *Science* **314**, (2006).

73. T. Kawai *et al.*, IPS-1, an adaptor triggering RIG-I- and Mda5-mediated type I interferon induction. *Nat Immunol* **6**, 981-988 (2005).

74. E. Meylan *et al.*, Cardif is an adaptor protein in the RIG-I antiviral pathway and is targeted by hepatitis C virus. *Nature* **437**, 1167-1172 (2005).

75. R. B. Seth, L. Sun, C. K. Ea, Z. J. Chen, Identification and characterization of MAVS, a mitochondrial antiviral signaling protein that activates NF-kappaB and IRF 3. *Cell* **122**, 669-682 (2005).

76. L. G. Xu *et al.*, VISA is an adapter protein required for virus-triggered IFN-beta signaling. *Mol Cell* **19**, 727-740 (2005).

77. A. K. Overby, V. L. Popov, M. Niedrig, F. Weber, Tick-borne encephalitis virus delays interferon induction and hides its double-stranded RNA in intracellular membrane vesicles. *J Virol* **84**, 8470-8483 (2010).

78. L. Uchida *et al.*, The dengue virus conceals double-stranded RNA in the intracellular membrane to escape from an interferon response. *Sci Rep* **4**, 7395 (2014).

79. C. J. Neufeldt *et al.*, The Hepatitis C Virus-Induced Membranous Web and Associated Nuclear Transport Machinery Limit Access of Pattern Recognition Receptors to Viral Replication Sites. *PLoS Pathog* **12**, e1005428 (2016).

80. J. W. Schoggins, Interferon-Stimulated Genes: What Do They All Do? *Annu Rev Virol* **6**, 567-584 (2019).

81. G. R. Stark, J. E. Darnell, Jr., The JAK-STAT pathway at twenty. *Immunity* **36**, 503-514 (2012).

82. S. Kang, H. M. Brown, S. Hwang, Direct Antiviral Mechanisms of Interferon-Gamma. *Immune Netw* **18**, e33 (2018).

83. S. B. Biering *et al.*, Viral Replication Complexes Are Targeted by LC3-Guided Interferon-Inducible GTPases. *Cell Host Microbe* **22**, 74-85 e77 (2017).

84. S. Hwang *et al.*, Nondegradative role of Atg5-Atg12/ Atg16L1 autophagy protein complex in antiviral activity of interferon gamma. *Cell Host Microbe* **11**, 397-409 (2012).

85. M. Hong *et al.*, Interferon lambda 4 expression is suppressed by the host during viral infection. *J Exp Med* **213**, 2539-2552 (2016).

86. A. I. Wells, C. B. Coyne, Type III Interferons in Antiviral Defenses at Barrier Surfaces. *Trends Immunol* **39**, 848-858 (2018).

87. A. Forero *et al.*, Differential Activation of the Transcription Factor IRF1 Underlies the Distinct Immune Responses Elicited by Type I and Type III Interferons. *Immunity* **51**, 451-464 e456 (2019).

88. W. M. Schneider, M. D. Chevillotte, C. M. Rice, Interferon-stimulated genes: a complex web of host defenses. *Annu Rev Immunol* **32**, 513-545 (2014).

89. J. L. Hyde *et al.*, Mouse norovirus replication is associated with virus-induced vesicle clusters originating from membranes derived from the secretory pathway. *J Virol* **83**, 9709-9719 (2009).

90. E. R. Hinson, P. Cresswell, The antiviral protein, viperin, localizes to lipid droplets via its N-terminal amphipathic α-helix

PNAS **106**, (2009).

91. E. R. Hinson, P. Cresswell, The N-terminal Amphipathic α-Helix of Viperin Mediates Localization to the Cytosolic Face of the Endoplasmic Reticulum and Inhibits Protein Secretion. *Journal of Biological Chemistry* **284**, 4705-4712 (2009).

92. H. T. McMahon, E. Boucrot, Membrane curvature at a glance. *Journal of Cell Science* **128**, 1065-1070 (2015).

93. A. I. Chiramel *et al.*, TRIM5α Restricts Flavivirus Replication by Targeting the Viral Protease for Proteasomal Degradation. *Cell Reports* **27**, 3269-3283.e3266 (2019).

94. A. Dukhovny *et al.*, A CRISPR Activation Screen Identifies Genes That Protect against Zika Virus Infection. *J Virol* **93**, (2019).

95. R. B. Richardson *et al.*, A CRISPR screen identifies IFI6 as an ER-resident interferon effector that blocks flavivirus replication. *Nature Microbiology* **3**, 1214-1223 (2018).

96. I. N. Boys *et al.*, RTP4 Is a Potent IFN-Inducible Anti-flavivirus Effector Engaged in a Host-Virus Arms Race in Bats and Other Mammals. *Cell Host & Microbe* **28**, 712-723.e719 (2020).

97. B. Chen, Y. Sun, J. Niu, G. K. Jarugumilli, X. Wu, Protein Lipidation in Cell Signaling and Diseases: Function, Regulation, and Therapeutic Opportunities. *Cell Chem Biol* **25**, 817-831 (2018).

98. S. Kuchay *et al.*, GGTase3 is a newly identified geranylgeranyltransferase targeting a ubiquitin ligase. *Nat Struct Mol Biol* **26**, 628-636 (2019).

99. F. L. Zhang, P. J. Casey, Protein prenylation: molecular mechanisms and functional consequences *Annual Reviews Biochemistry* **65**, (1996).

100. J. R. Silvius, F. l'Heureux, Fluorimetric evaluation of the affinities of isoprenylated peptides for lipid bilayers *Biochemistry* **33**, (1994).

101. H. L. Hartman, K. A. Hicks, C. A. Fierke, Peptide specificity of protein prenyltransferases is determined mainly by reactvitiy rather than binding affinity. *Biochemistry* **44**, (2005).

102. M. Wang, P. J. Casey, Protein prenylation: unique fats make their mark on biology. *Nat Rev Mol Cell Biol* **17**, 110-122 (2016).

103. D. K. Simanshu, D. V. Nissley, F. McCormick, RAS Proteins and Their Regulators in Human Disease. *Cell* **170**, 17-33 (2017).

104. I. M. Ahearn, K. Haigis, D. Bar-Sagi, M. R. Philips, Regulating the regulator: post-translational modification of RAS. *Nat Rev Mol Cell Biol* **13**, 39-51 (2011).

105. G. Charron, M. M. Li, M. R. MacDonald, H. C. Hang, Prenylome profiling reveals S-farnesylation is crucial for membrane targeting and antiviral activity of ZAP long-isoform. *Proc Natl Acad Sci U S A* **110**, 11085-11090 (2013).

106. E. Braun *et al.*, Guanylate-Binding Proteins 2 and 5 Exert Broad Antiviral Activity by Inhibiting Furin-Mediated Processing of Viral Envelope Proteins. *Cell Rep* **27**, 2092-2104 e2010 (2019).

107. N. Britzen-Laurent *et al.*, Intracellular trafficking of guanylate-binding proteins is regulated by heterodimerization in a hierarchical manner. *PLoS One* **5**, e14246 (2010).

108. S. A. Holstein, R. J. Hohl, Isoprenoids: remarkable diversity of form and function *Lipids* **39**, (2004).

109. J. Greenwood, L. Steinman, S. S. Zamvil, Statin therapy and autoimmune disease: from protein prenylation to immunomodulation. *Nat Rev Immunol* **6**, 358-370 (2006).

110. S. P. Parihar, R. Guler, F. Brombacher, Statins: a viable candidate for host-directed therapy against infectious diseases. *Nat Rev Immunol* **19**, 104-117 (2019).

111. Z. Zhang *et al.*, Host Lipids in Positive-Strand RNA Virus Genome Replication. *Front Microbiol* **10**, 286 (2019).

112. X. J. Zhang *et al.*, In-Hospital Use of Statins Is Associated with a Reduced Risk of Mortality among Individuals with COVID-19. *Cell Metab* **32**, 176-187 e174 (2020).

113. R. Wang *et al.*, Genetic screens identify host factors for SARS-CoV-2 and common cold coronaviruses *Cell* **184**, (2021).

114. R. S. Harris, J. P. Dudley, APOBECs and virus restriction. *Virology* **479-480**, 131-145 (2015).

115. O. Haller, P. Staeheli, M. Schwemmle, G. Kochs, Mx GTPases: dynamin-like antiviral machines of innate immunity. *Trends Microbiol* **23**, 154-163 (2015).

116. M. S. Diamond, M. Farzan, The broad-spectrum antiviral functions of IFIT and IFITM proteins. *Nat Rev Immunol* **13**, 46-57 (2013).

117. A. Jarret *et al.*, Hepatitis-C-virus-induced microRNAs dampen interferon-mediated antiviral signaling. *Nat Med* **22**, 1475-1481 (2016).

118. A. P. McFarland *et al.*, The favorable IFNL3 genotype escapes mRNA decay mediated by AU-rich elements and hepatitis C virus-induced microRNAs. *Nat Immunol* **15**, 72-79 (2014).

119. R. Savan, Post-transcriptional regulation of interferons and their signaling pathways. *J Interferon Cytokine Res* **34**, 318-329 (2014).

120. J. Schwerk, R. Savan, Translating the Untranslated Region. *J Immunol* **195**, 2963-2971 (2015).

121. M. J. Bick *et al.*, Expression of the zinc-finger antiviral protein inhibits alphavirus replication. *J Virol* **77**, 11555-11562 (2003).

122. G. Gao, X. Guo, S. P. Goff, Inhibition of retroviral RNA production by ZAP, a CCCH-type zing finger protein *Science* **297**, (2002).

123. S. Muller *et al.*, Inhibition of filovirus replication by the zinc finger antiviral protein. *J Virol* **81**, 2391-2400 (2007).

124. Y. Zhu *et al.*, Zinc-finger antiviral protein inhibits HIV-1 infection by selectively targeting multiply spliced viral mRNAs for degradation. *Proc Natl Acad Sci U S A* **108**, 15834-15839 (2011).

125. X. Guo, J. W. Carroll, M. R. Macdonald, S. P. Goff, G. Gao, The zinc finger antiviral protein directly binds to specific viral mRNAs through the CCCH zinc finger motifs. *J Virol* **78**, 12781-12787 (2004).

126. X. Guo, J. Ma, J. Sun, G. Gao, The zinc-finger antiviral protein recruits the RNA processing exosome to degrade the target mRNA *Proc Natl Acad Sci U S A* **104**, (2007).

127. J. A. Kerns, M. Emerman, H. S. Malik, Positive selection and increased antiviral activity associated with the PARP-containing isoform of human zinc-finger antiviral protein. *PLoS Genet* **4**, e21 (2008).

128. S. Vyas, M. Chesarone-Cataldo, T. Todorova, Y. H. Huang, P. Chang, A systematic analysis of the PARP protein family identifies new functions critical for cell physiology. *Nat Commun* **4**, 2240 (2013).

129. S. Hayakawa *et al.*, ZAPS is a potent stimulator of signaling mediated by the RNA helicase RIG-I during antiviral responses. *Nat Immunol* **12**, 37-44 (2011).

130. K. D. Ryman *et al.*, Sindbis virus translation is inhibited by a PKR/RNase L-independent effector induced by alpha/beta interferon priming of dendritic cells. *J Virol* **79**, 1487-1499 (2005).

131. N. Wang *et al.*, Viral induction of the zinc finger antiviral protein is IRF3-dependent but NF-kappaB-independent. *J Biol Chem* **285**, 6080-6090 (2010).

132. Y. Takagaki, R. L. Seipelt, M. L. Peterson, J. L. Manley, The polyadenylation factor CstF-64 regulates alternative processing of IgM heavy chain pre-mRNA during B cell differentiation *Cell* **87**, (1996).

133. S. Chuvpilo *et al.*, Alternative polyadenylation events contribute to the induction of NF-ATc in effector T cells

Immunity **10**, (1999).

134. S. A. Shell, C. Hesse, S. M. Morris, Jr., C. Milcarek, Elevated levels of the 64-kDa cleavage stimulatory factor (CstF-64) in lipopolysaccharide-stimulated macrophages influence gene expression and induce alternative poly(A) site selection. *J Biol Chem* **280**, 39950-39961 (2005).

135. H. Lee *et al.*, Zinc-finger antiviral protein mediates retinoic acid inducible gene I-like receptor-independent antiviral response to murine leukemia virus. *Proc Natl Acad Sci U S A* **110**, 12379-12384 (2013).

136. M. G. L. Gustafsson, Surpassing the lateral resolution limit by a factor of two using structured illumination microscopy *Journal of Microscopy* **198** (2000).

137. Y. Zhang, C. W. Burke, K. D. Ryman, W. B. Klimstra, Identification and Characterization of Interferon-Induced Proteins That Inhibit Alphavirus Replication. *Journal of Virology* **81**, 11246-11255 (2007).

138. D. P. DiCiommo, R. Bremner, Rapid, high level protein production using DNA-based Semliki Forest virus vectors. *The Journal of Biological Chemistry* **273**, (1998).

139. H. P. Chiu *et al.*, Inhibition of Japanese encephalitis virus infection by the host zinc-finger antiviral protein. *PLoS Pathog* **14**, e1007166 (2018).

140. Y. Zhu, X. Wang, S. P. Goff, G. Gao, Translational repression precedes and is required for ZAP-mediated mRNA decay. *EMBO J* **31**, 4236-4246 (2012).

141. A. T. Rosengren, T. A. Nyman, S. Syyrakki, S. Matikainen, R. Lahesmaa, Proteomic and transcriptomic characterization of interferon-alpha-induced human primary T helper cells. *Proteomics* **5**, 371-379 (2005).

142. Z. Huang, X. Wang, G. Gao, Analyses of SELEX-derived ZAP-binding RNA aptamers suggest that the binding specificity is determined by both structure and sequence of the RNA. *Protein Cell* **1**, 752-759 (2010).

143. M. A. Takata *et al.*, CG dinucleotide suppression enables antiviral defence targeting non-self RNA. *Nature* **550**, 124-127 (2017).

144. S. Chen *et al.*, Structure of N-terminal domain of ZAP indicates how a zinc-finger protein recognizes complex RNA. *Nat Struct Mol Biol* **19**, 430-435 (2012).

145. S. Glasker, M. Toller, B. M. Kummerer, The alternate triad motif of the poly(ADP-ribose) polymerase-like domain of the human zinc finger antiviral protein is essential for its antiviral activity. *J Gen Virol* **95**, 816-822 (2014).

146. C. H. Liu, L. Zhou, G. Chen, R. M. Krug, Battle between influenza A virus and a newly identified antiviral activity of the PARP-containing ZAPL protein. *Proc Natl Acad Sci U S A* **112**, 14048-14053 (2015).

147. X. Wang *et al.*, Sindbis Virus Can Exploit a Host Antiviral Protein To Evade Immune Surveillance. *J Virol* **90**, 10247-10258 (2016).

148. T. Saito, D. M. Owen, F. Jiang, J. Marcotrigiano, M. Gale, Jr., Innate immunity induced by composition-dependent RIG-I recognition of hepatitis C virus RNA. *Nature* **454**, 523-527 (2008).

149. T. J. Urban *et al.*, IL28B genotype is associated with differential expression of intrahepatic interferon-stimulated genes in patients with chronic hepatitis C. *Hepatology* **52**, 1888-1896 (2010).

150. J. R. Friedman, B. M. Webster, D. N. Mastronarde, K. J. Verhey, G. K. Voeltz, ER sliding dynamics and ER-mitochondrial contacts occur on acetylated microtubules. *J Cell Biol* **190**, 363-375 (2010).

151. A. A. Rowland, P. J. Chitwood, M. J. Phillips, G. K. Voeltz, ER contact sites define the position and timing of endosome fission. *Cell* **159**, 1027-1041 (2014).

152. S. G. Olenych, N. S. Claxton, G. K. Ottenberg, M. Davidson, The fluorescent protein color palette *Current Protocols Cell Biology* **33**, (2006).

153. D. A. Vogt, M. Ott, Membrane flotation assay. *Bio Protocols* **5**, (2015).

154. E. Boritz, J. Gerlach, J. E. Johnson, J. K. Rose, Replication-competent rhabdoviruses with human immunodeficiency virus type 1 coat and green fluorescent protein: entry by a pH-independent pathway *Journal of Virology* **73**, (1999).

155. V. Hornung, R. Hartmann, A. Ablasser, K. P. Hopfner, OAS proteins and cGAS: unifying concepts in sensing and responding to cytosolic nucleic acids. *Nat Rev Immunol* **14**, 521-528 (2014).

156. J. Lohofener *et al.*, The Activation Mechanism of 2'-5'-Oligoadenylate Synthetase Gives New Insights Into OAS/cGAS Triggers of Innate Immunity. *Structure* **23**, 851-862 (2015).

157. Y. Han *et al.*, Structure of human RNase L reveals the basis for regulated RNA decay in the IFN response. *Science* **343**, 1244-1248 (2014).

158. R. H. Silverman, Viral encounters with 2',5'-oligoadenylate synthetase and RNase L during the interferon antiviral response. *J Virol* **81**, 12720-12729 (2007).

159. V. Bonnevie-Nielsen *et al.*, Variation in antiviral 2',5'-oligoadenylate synthetase (2'5'AS) enzyme activity is controlled by a single-nucleotide polymorphism at a splice-acceptor site in the OAS1 gene. *Am J Hum Genet* **76**, 623-633 (2005).

160. J. K. Lim *et al.*, Genetic variation in OAS1 is a risk factor for initial infection with West Nile virus in man. *PLoS Pathog* **5**, e1000321 (2009).

161. A. Ablasser, S. Hur, Regulation of cGAS- and RLR-mediated immunity to nucleic acids. *Nat Immunol* **21**, 17-29 (2020).

162. Y. K. Chan, M. U. Gack, Viral evasion of intracellular DNA and RNA sensing. *Nat Rev Microbiol* **14**, 360-373 (2016).

163. I. Romero-Brey, R. Bartenschlager, Membranous replication factories induced by plus-strand RNA viruses. *Viruses* **6**, 2826-2857 (2014).

164. H. Li *et al.*, Identification of a Sjogren's syndrome susceptibility locus at OAS1 that influences isoform switching, protein expression, and responsiveness to type I interferons. *PLoS Genet* **13**, e1006820 (2017).

165. C. M. Carey *et al.*, Recurrent Loss-of-Function Mutations Reveal Costs to OAS1 Antiviral Activity in Primates. *Cell Host Microbe* **25**, 336-343 e334 (2019).

166. A. J. DeGraw *et al.*, Evaluation of alkyne-modified isoprenoids as chemical reporters of protein prenylation. *Chem Biol Drug Des* **76**, 460-471 (2010).

167. C. E. Melia *et al.*, The Origin, Dynamic Morphology, and PI4P-Independent Formation of Encephalomyocarditis Virus Replication Organelles. *mBio* **9**, (2018).

168. J. Chebath, P. Benech, M. Revel, M. Vigneron, Constitutive expression of (2'-5') oligo A synthetase confers resistance to picornavirus infection.

. *Nature* **330**, (1987).

169. S. N. Sarkar, A. Ghosh, H.-W. Wang, S.-S. Sung, G. C. Sen, The nature of the catalytic domain of 2'-5'-oligoadenylate synthetases *The Journal of Biological Chemistry* **36**, (1999).

170. K. Malathi, B. Dong, M. Gale, Jr., R. H. Silverman, Small self-RNA generated by RNase L amplifies antiviral innate immunity. *Nature* **448**, 816-819 (2007).

171. A. Ghosh, S. N. Sarkar, W. Guo, S. Bandyopadhyay, G. C. Sen, Enzymatic activity of 2'-5'-oligoadenylate synthetase is impaired by specific mutations that affect oligomerization of the protein *The Journal of Biological Chemistry* **272**, (1997).

172. E. G. Westaway, J. M. Mackenzie, M. T. Kenney, M. K. Jones, A. A. Khromykh, Ultrastructure of Kunjin virus infected cells: colocalization of NS1 and NS3 with double-stranded RNA, and of NS2B with NS3, in virus-induced membrane structures

173. A. M. Ward *et al.*, The Golgi associated ERI3 is a Flavivirus host factor. *Sci Rep* **6**, 34379 (2016).

174. Y. Li *et al.*, Activation of RNase L is dependent on OAS3 expression during infection with diverse human viruses. *Proc Natl Acad Sci U S A* **113**, 12573 (2016).

175. J.-Y. Min, R. M. Krug, The primary function of RNA binding by the influenza A virus NS1 protein in infected cells: inhibiting the 2'-5' oligo (A) synthetase/RNase L pathway *PNAS* **103**, (2006).

176. J. M. Mackenzie, A. A. Khromykh, R. G. Parton, Cholesterol manipulation by West Nile virus perturbs the cellular immune response. *Cell Host Microbe* **2**, 229-239 (2007).

177. A. J. Sams *et al.*, Adaptively introgressed Neandertal haplotype at the OAS locus functionally impacts innate immune responses in humans. *Genome Biol* **17**, 246 (2016).

178. X. Liu *et al.*, A functional variant in the OAS1 gene is associated with Sjogren's syndrome complicated with HBV infection. *Sci Rep* **7**, 17571 (2017).

179. M. O'Brien *et al.*, A multiple sclerosis susceptibility gene that influences disease severity *Neurology* **75**, (2010).

180. M. S. Ibsen *et al.*, The 2'-5'-oligoadenylate synthetase 3 enzyme potently synthesizes the 2'-5'-oligoadenylates required for RNase L activation. *J Virol* **88**, 14222-14231 (2014).

181. L. Lau, E. E. Gray, R. L. Brunette, D. B. Stetson, DNA tumor virus oncogenes antagonize the cGAS-STING DNA-sensing pathway *Science* **350**, (2015).

182. J. Schwerk *et al.*, RNA-binding protein isoforms ZAP-S and ZAP-L have distinct antiviral and immune resolution functions. *Nat Immunol* **20**, 1610-1620 (2019).

183. L. D. Aarreberg *et al.*, Interleukin-1beta Induces mtDNA Release to Activate Innate Immune Signaling via cGAS-STING. *Mol Cell* **74**, 801-815 e806 (2019).

VITA

Frank was born in Cicero, Illinois where he attended grade school (1st-6th) at Abe Lincoln elementary school and Unity Jr. High (7^{th}-8^{th}), and high school at John Sterling Morton East High School. In 2009 he pursued a bachelors of science in zoology with a minor in chemistry at Southern Illinois University Carbondale (SIUC). Simultaneously, he worked in the laboratory of Dr. Agustin Jimenez where he studied host parasite interactions between woodwasps and their nematode parasites and phylogenetics of treamatode parasites of New World marsupials. In the summer of 2012, he was a Research Experience for Undergraduates (REU) intern in the laboratory of Dr. Aaron Turkewitz in the Department of Molecular Genetics and Cell Biology at the University of Chicago where he worked on protein regulators of phagosome maturation in the ciliate *Tetrahymena thermophila*. After graduating *magna cum laude* at SIUC in 2013, he worked in the laboratory of Dr. Joan Cook-Mills in the Division of Allergy and Immunology at Northwestern University Feinberg School of Medicine. There, he studied endothelial regulators of leukocyte migration during allergic airway inflammation. In 2015, he joined the immunology graduate program at the University of Washington where he rotated in the laboratories of Drs. Jessica Hamerman, Daniel Stetson, and Ram Savan. He joined the Ram lab in the spring of 2016.